The University of Osaka
Institutional Knowledge Archive

Title	Study on the Mechanism of Gain Drop in a Microchannel Plate
Author(s)	小林, 浩之
Citation	大阪大学, 2023, 博士論文
Version Type	VoR
URL	https://doi.org/10.18910/93019
rights	
Note	

The University of Osaka Institutional Knowledge Archive : OUKA

https://ir.library.osaka-u.ac.jp/

The University of Osaka

Study on the Mechanism of Gain Drop in a Microchannel Plate

Hiroshi Kobayashi

Department of Physics, Graduate School of Science,

Osaka University

Contents

1. Introduction

Microchannel plates (MCPs) play a key role in the detection of charged and uncharged particles, including electrons, ions, and photons, in various fields owing to their high gain [1-1] and excellent temporal characteristics[1-1–3]. An MCP is an array of 10^4–10^8 parallel electron multiplier channels. The channels are tilted from 2°–20° with respect to the normal of the front surface. Each channel has a diameter of 2–25 μm and a length of 0.1–1.0 mm from the input to output surfaces. The inner surface of the channel is a semiconductor with a high resistivity of 10^{12}–10^{16} Ω from the input to the output surfaces and a high secondary electron emission yield. The channels are electrically connected in parallel using evaporated metal electrodes on the surface. Generally, a voltage of 500–1,000 V is applied between the surfaces, and each channel functions as a continuous dynode. When a particle hits the channel wall, a few secondary electrons are emitted from the channel wall. The electrons are accelerated along the channel by the electric field between the input and output electrodes and collide with the channel wall again to emit further secondary electrons. This process is repeated, and the number of electrons is multiplied by approximately 10^4 during their output from the channel. With a strong electric field of ~10^6 V/m along the channel, the transit time of electrons from multiplication to output is less than 500 ps, [1-4,5] producing a short pulse of less than 1 ns for a single particle [1-1]. Two or three stacked MCPs were used to obtain a gain of 10^6 to detect a single particle. A chevron configuration is widely used for two-stack MCPs, where one MCP rotates 180° relative to the other [1-1,6]. Because MCP detectors can output a very short pulse of less than 1 ns, they are suitable for time-of-flight (TOF) mass spectrometry (MS), in which individual ions arrive at the detector in short time intervals of a few microseconds to nanoseconds. Although the MCP detector has sufficient gain to detect a single particle and excellent temporal characteristics, the 'gain-drop' phenomenon of MCP has been reported in TOF-MS [1-7,8] and photon counting [1-9,10], where the MCP gain drops temporally after electron multiplication processes. Multiplication

depletes the charge from the channel wall, and the gain drop lasts until the charge is replenished from the voltage supply [1-1,8]. This phenomenon alters the gain in a short interval; therefore, not considering this phenomenon leads to misinterpretation of the signal intensities in the TOF spectrum and count rate.

The gain-drop phenomenon in MCP has been studied since the 1970s. Gatti et al. [1-11] reported that the electric field along the channel of an MCP changes owing to the depleted charges (wall charges) on the walls. Moreover, they showed that the changed electric field affects the gain of the multiplication process, which persisted until the charges were replenished. The recharge time corresponding to the gain recovery time was expected to be comparable to the product of the resistance R and capacitance C of the channel plate (RC constant) [1-1,8]. However, the recovery time constants evaluated in previous studies [1-12–15] were inconsistent with the constant RC and differed from each other. Fraser et al. [1-12,13] experimentally evaluated the time constant from the ratio of the MCP output current to the nominal conduction (strip) current for continuous X-ray or ultraviolet (UV) illumination (continuous irradiation method). The gain recovery time constant was 2.5 to 27,500 times the RC constant. Instead of the continuous irradiation method, the recovery time of an MCP has been obtained by irradiating double pulses in some studies [1-14,15] (double-pulse method). Giudicotti et al. [1-14] evaluated the recovery time of an MCP photomultiplier tube (manufactured by ITT Electro Optical Products Division), which contained an S-20 photocathode and a 3-stage MCP, using light-emitting diodes (LEDs) ($\lambda = 670$ nm). The recovery time constant was a few times longer than the RC constant. Coeck et al. [1-15] evaluated the gain recovery time constant of a chevron MCP detector using double-ion pulses; the constant was twice the RC constant.

Another issue with MCP detectors is that a gain drop occurs not only in the activated channels where the electrons are multiplied, but also in the surrounding channels. The spatial extension of the gain drop was a significant issue in the 1990s, as it caused image distortion. Gatti et al. suggested that the

electric field produced by the wall charges in the activated channels leaked into the surrounding channels, affecting their gain [1-11]. Anacker et al. calculated the electric field produced by wall charges and estimated that the gain depression (gain drop) obtained by detecting a single particle extends up to 190 μm at a gain of 5×10^6 (corresponding to 0.8 pC for a single particle) [1-16]. In contrast, Edgar et al. [1-17] and Fraser et al. [1-13] evaluated the spatial extent of the gain drop in chevron MCP detectors under continuous UV photon illumination at a high count rate. Fraser et al. reported that the spatial extent of gain drop was reported to be 1.5–2.0 mm when UV was irradiated to a radius of ~0.5 mm. The spatial extent was approximately one order of magnitude greater than that estimated by Anacker et al. One possible cause of this inconsistency is the difference between the detector gains of 5×10^6 and 4×10^7. Furthermore, Fraser et al. reported that the count rate was ~ 0.7% of the maximum value at a radius of 1.0 mm from the center of the point despite the illumination radius of ~0.5 mm, suggesting the possibility of slight light leakage to the surrounding channels. To determine the spatial extent of the gain drop more accurately, evaluation of the spatial extent of the gain drop without light leakage is necessary. Thus, the spatial extent of a single pulse should be investigated.

The purpose of this study is to understand the gain-drop mechanism, particularly gain recovery and spatial extension. The gain recovery and spatial extent were investigated using a TOF mass spectrometer and an experimental system consisting of UV light sources. This study provides new insights into the development of novel detectors. The remainder of this thesis is organized as follows.

Chapter 2:

This chapter explains the fundamentals of MCPs in light of previous studies. Furthermore, it describes the structure, manufacturing method, operational theory, general characteristics, and applications.

Chapter 3:

The gain recovery time courses of the two chevron MCP detectors were evaluated using a multi-turn TOF mass spectrometer [1-18]. By irradiating two isotope clusters of xenon ions, the gain recovery time constants of two chevron MCP detectors were evaluated as 0.38 and 0.48 times the *RC* constant. The values obtained by ion irradiation were significantly different from those (2.5 to 27,500) obtained by UV or X-ray irradiation using the continuous irradiation method [1-12,13].

Chapter 4:

The gain recovery time constant was evaluated by two evaluation methods (the double-pulse method [1-14,15] and the continuous irradiation method [1-12,13]) using the same chevron MCP detector [1-19]. The time constants obtained using the continuous irradiation method differed significantly from those obtained using the double-pulse method, and the reason behind this difference is discussed in the chapter.

Chapter 5:

One possible mechanism for the spatial extension of the gain drop is that the electric field produced by the wall charges in the activated channels leaks to the surrounding channels, affecting their gains. By assuming that the field leakage causes a spatial extension of the gain drop, the electric field produced by the wall charges is calculated, and the spatial extent is estimated [1-20].

Chapter 6:

The spatial extent of the gain drop by single-pulse irradiation has been experimentally evaluated [1-21]. The relationship between the spatial extent of the gain drop and output charge corresponding to the wall charge was investigated and compared with those estimated in Chapter 5.

Chapter 7：

A new ion detector 'MIGHTION' is developed that combines an MCP with an avalanche diode (AD) [1-22]. According to the findings in the previous chapters, the gain-drop strongly depends on the amount of the output charge. Therefore, the MCP operation at low gain allows to prevent the gain drop. In MIGHTION, the MCP gain can be reduced to 10^2, while keeping the total gain of 10^6 due to the AD gain of 10^4. The performance of MIGHTION is verified using a TOF mass spectrometer.

Finally, in Chapter 8, the achievements of this study are summarized.

References

[1-1]   J.L. Wiza, Nuclear Instruments and Methods 162 (1979) 587–601.

[1-2]   S. Matsuura, S. Umebayashi, Y. Kusyama, Y. Natsume, K. Oba, Nuclear Instruments and Methods in Physics Research Section A: Accelerators, Spectrometers, Detectors and Associated Equipment 363 (1995) 481–484.

[1-3]   K. Matsuoka, Nuclear Instruments and Methods in Physics Research Section A: Accelerators, Spectrometers, Detectors and Associated Equipment 766 (2014) 148–151.

[1-4]   M. Wu, C.A. Kruschwitz, D.V. Morgan, J. Morgan, Review of Scientific Instruments 79 (2008) 073104.

[1-5]   Q. Wang, Z. Yuan, Z. Cao, B. Deng, T. Chen, K. Deng, Review of Scientific Instruments 87 (2016) 073303.

[1-6]   W. Parkes, R. Gott, Nuclear Instruments and Methods 95 (1971) 487–491.

[1-7]   R.C. Beavis, B.T. Chait, Rapid Communications in Mass Spectrometry Vol. 3 (1989) 233–237.

[1-8]   A. Westman, G. Brinkmalm, D.F. Barofsky, International Journal of Mass Spectrometry and Ion Processes 169–170 (1997) 79–87.

[1-9]   J.E. Bateman, R.J. Apsimon, Nuclear Instruments and Methods 137 (1976) 61–70.

[1-10]   J.F. Pearson, J.E. Lees, G.W. Fraser, IEEE Transactions on Nuclear Science Vol. 35 (1988) 520–523.

[1-11]   E. Gatti, K. Oba, P. Rehak, IEEE Transactions on Nuclear Science NS-30 (1983) 461–468.

[1-12]   G.W. Fraser, M.T. Pain, J.E. Lees, J.F. Pearson, Nuclear Instruments and Methods in Physics Research Section A: Accelerators, Spectrometers, Detectors and Associated Equipment 306

(1991) 247–260.

[1-13] G.W. Fraser, M.T. Pain, J.E. Lees, Nuclear Instruments and Methods in Physics Research Section A: Accelerators, Spectrometers, Detectors and Associated Equipment 327 (1993) 328–336.

[1-14] L. Giudicotti, M. Bassan, R. Pasqualotto, A. Sardella, Review of Scientific Instruments 65 (1994) 247–258.

[1-15] S. Coeck, M. Beck, B. Delauré, V.V. Golovko, M. Herbane, A. Lindroth, S. Kopecky, V.Yu. Kozlov, I.S. Kraev, T. Phalet, N. Severijns, Nuclear Instruments and Methods in Physics Research Section A: Accelerators, Spectrometers, Detectors and Associated Equipment 557 (2006) 516–522.

[1-16] D.C. Anacker, J.L. Erskine, Review of Scientific Instruments 62 (1991) 1246–1255.

[1-17] M.L. Edgar, J.S. Lapington, A. Smith, Review of Scientific Instruments 63 (1992) 816–819.

[1-18] H. Kobayashi, T. Hondo, M. Toyoda, Journal of Mass Spectrometry 56 (2021).

[1-19] H. Kobayashi, T. Hondo, Y. Kanematsu, M. Suyama, M. Toyoda, Nuclear Instruments and Methods in Physics Research Section A: Accelerators, Spectrometers, Detectors and Associated Equipment 1053 (2023) 168355.

[1-20] Submitted to Mass Spectrometry (2023).

[1-21] Submitted to Nuclear Instruments and Methods in Physics Research Section A: Accelerators, Spectrometers, Detectors and Associated Equipment (2023).

[1-22] H. Kobayashi, T. Hondo, N. Imaoka, M. Suyama, M. Toyoda, Nuclear Instruments and Methods in Physics Research Section A: Accelerators, Spectrometers, Detectors and Associated Equipment 971 (2020) 164110.

2. Microchannel plates

2.1 Introduction

In various fields, such as mass spectrometry (MS) and high-energy physics (HEP), detectors for particles (ions, electrons, and photons) play a key role. The Faraday cup is a basic detector for charged particles in vacuum and was named after Michael Faraday, who first theorized about ions in approximately 1830. A metal cup is placed in the path of the electron or ion beam and attached to an electrometer to measure the beam current (Fig. 2-1 (a)). A Faraday cup was used in mass spectrometers in the 1910s [2-1,2]. Koeigsberger and Kutchewski first reported the sensitivity of photographic plates to positive ions [2-3]. Beginning in 1911, Thomson began using photographic plates exclusively in his parabola-positive ray apparatus [2-4]. The main advantage of photographic plates is their ability to record hundreds of ion beams simultaneously. However, neither the Faraday cup nor the photographic plate were sufficiently sensitive to detect a single particle.

Electron multipliers have been developed to detect single particles. The principle of operation of the electron multipliers is based on secondary electron emission, in which secondary electrons are emitted when a primary particle with sufficient energy collides with atoms. Two basic forms of electron multipliers exist: the discrete-dynode electron multiplier (Fig. 2-1 (b)) and the continuous-dynode electron multiplier (Fig. 2-1 (c)). A typical discrete-dynode electron multiplier has 10–30 dynodes coated with a secondary emission material, and the voltage applied between the dynodes is generally 100–200 V. A particle emits secondary electrons when it hits the first dynode. The secondary electrons accelerate and collide with the next dynode. Electron multiplication was repeated at each dynode, generating 10^4–10^8 electrons, which were finally collected by the anode. Amplification of 10^6 times or more allows the detection of a single particle. In 1930, Kubetsky et al. proposed a discrete-

dynode electron multiplier as part of the photomultiplier tube (PMT) [2-5]. In 1936, Zworykin et al. developed a discreet electron multiplier in which each flight between dynodes was controlled by electric and magnetic fields [2-6]. In 1939, Zworykin and Rajchman developed a discrete electron multiplier in which the electron trajectory in each dynode was controlled by an electrostatic field (this is the basic structure currently used) [2-7]. Farnsworth first proposed the concept of a continuous-dynode electron multiplier in 1930 [2-8]. Approximately 30 years later, Goodrich and Wiley at Bendix Research Laboratories reported for the first time the continuous-dynode electron multiplier fabricated using a high-temperature hydrogen reduction technique of lead glass [2-9]. This technique produces conductivity and secondary emissive characteristics on the channel surface, allowing the operation of a continuous-dynode electron multiplier, as shown in Fig. 2-1 (c). The continuous-dynode electron multiplier also amplifies the signal by 10^2 to 10^8, owing to the electron avalanche, similar to the discrete-dynode electron multiplier [2-9]. Goodrich and Wiley experimentally found the relationship between gain, applied voltage, and the ratio of the length L to diameter D. The ratio is expressed as follows:

$$\alpha = \frac{L}{D} \tag{2-1}$$

This relationship was theoretically derived by previous studies [2-10–12]. Assuming that the continuous-dynode electron multiplier is a discrete-dynode electron multiplier with n dynodes, gain G can be described as follows:

$$G = \delta^n \tag{2-2}$$

where δ is the gain per collision. Assuming that the channel is straight, the flight distance of the secondary electrons between collisions l can be derived as follows:

$$l = \frac{D^2}{4V_0}\left(\frac{V}{L}\right) \tag{2-3}$$

where V_0 and V are the initial energy of the secondary electrons and the voltage applied to the channel, respectively. According to Eq. (2-3), the number of collisions n can be described as follows:

$$n = \frac{L}{l} = \frac{4V_0}{V}\alpha^2 \tag{2-4}$$

Adams and Manly [2-10] derived an expression that shows the dependence of gain G on the applied voltage V and the ratio α, assuming that $\delta = A\frac{V}{n}$, where A is a constant.

$$G = \left(\frac{AV^2}{4V_0\alpha^2}\right)^{\frac{4V_0}{V}\alpha^2} \tag{2-5}$$

This suggests that the gain of the continuous-dynode electron multiplier depends on the length-to-diameter ratio α and not on the absolute physical dimensions.
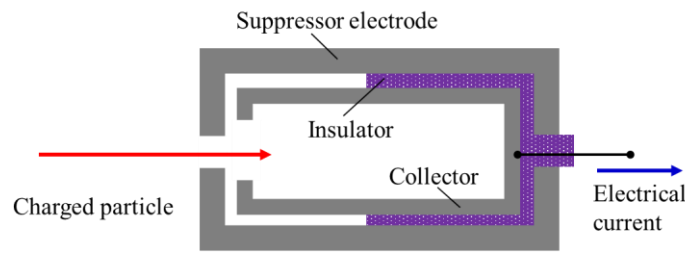
(a) Faraday cup
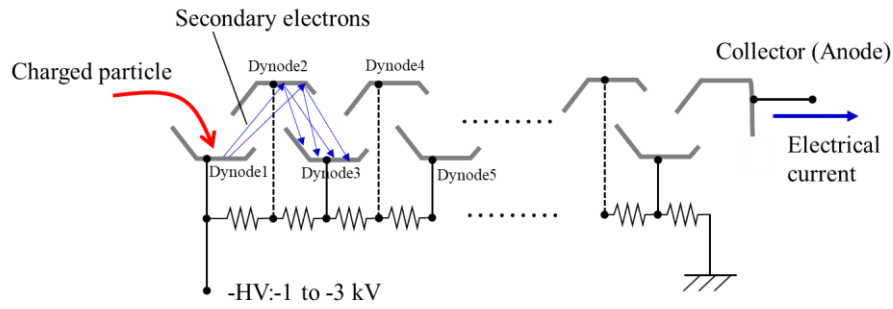
(b) Discrete-dynode electron multiplier

(c) Continuous-dynode electron multiplier

Fig. 2-1. Schematics of the detectors for charged particles.

On the other hand, minimization of the image intensifier is required, which is a vacuum-tube device used to intensify light images in the 1950s and the 1960s. Because the image intensifier for this period did not have an electron multiplier, the gain was only 50. Thus, multiple image intensifiers were used in the cascade to achieve sufficient gain, as shown in Fig. 2-2 (a). However, the image intensifiers were significantly large for military use. In addition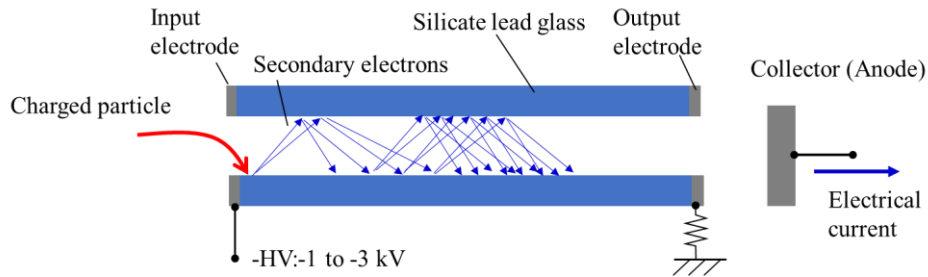, a high voltage (> 40 kV) was necessary to operate the cascade image intensifier. Therefore, the application of a continuous-dynode electron multiplier as an image intensifier was considered. A large number of independent electron multipliers are necessary to intensify the image. In this case, the spatial resolution was determined by the channel size of the electron multiplier. As described in Eq. (2-5), the continuous-dynode electron multiplier allows sufficient gain by maintaining α even when the channel diameter is reduced. Thus, the channel diameter is limited by available glass technology. The first multiple electron multipliers for the image intensifier were reported in 1962 by Willey and Hendee at Bendix Research Laboratories. They were assembled by bonding together approximately 5,000 continuous-dynode electron multipliers of diameter 100 μm [2-13]. This is an early microchannel plate (MCP). By introducing the MCP to the image intensifier, the size of the image intensifier was drastically reduced, as shown in Fig. 2-2 (b). In addition, the operating voltage can be reduced to less than 10 kV.

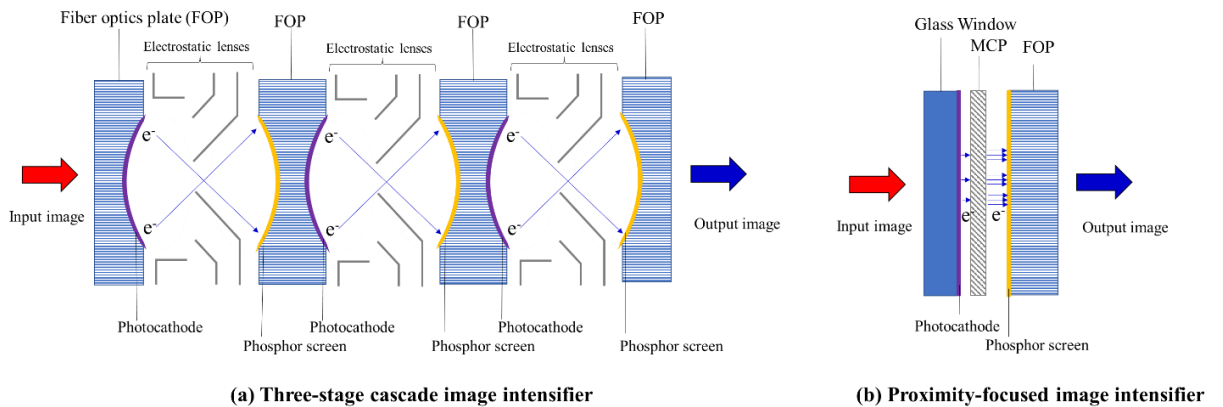(a) Three-stage cascade image intensifier   (b) Proximity-focused image intensifier

Fig. 2-2. Schematics of the image intensifiers.

Later, MCPs were manufactured using the fiber drawing technique used in the manufacturing of fiber optic plates (FOPs) [2-14]. Currently, a two-step glass-fiber drawing method is generally used in the MCP manufacturing process. Figure 2-3 shows a schematic of the MCP production by the two-step glass fiber drawing method. (1) A two-part billet consisting of an etchable glass core surrounded by lead glass cladding was drawn down to a single fiber. (2) Single fibers were aligned hexagonally and fused to form a hexagonal multi-fiber billet. (3) multi-fiber billets were drawn to form a multi-fiber. (4) The multi-fibers were aligned and fused to form an MCP billet. (5) The MCP wafers were produced by slicing a billet. (6) After polishing, the MCP wafer was chemically etched, and the core glass was etched away, forming the channels. (7) Subsequently, in the hydrogen reduction process, the surface was converted from an insulator to a semiconductor with high resistance and given to a secondary electron emission property. (8) Finally, metals, such as nichrome or Inconel, were evaporated to form electrodes on the input and output surfaces to electrically connect the individual channels. Recently, MCPs have been fabricated using atomic layer deposition (ALD) [2-15,16]. This technique allows the formation of resistive and emissive layers on the inner surface instead of hydrogen reduction. Figure 2-4 (a) illustrates the schematic of an MCP, which is an array of 10^4–10^8 parallel electron multiplier channels. The channels are tilted from 2° to 20° with respect to the normal of the front surface. Each channel has a diameter of 2–25 μm and a length of 0.1–1.0 mm from the input to output surfaces. By applying a voltage between the electrodes, each channel acts as an independent continuous-dynode electron multiplier, as shown in Fig. 2-4 (b). In this chapter, the fundamental characteristics and applications of MCP are described.

Core glass

Clad glass
(Lead glass)

Single fiber

Multi-fiber billet

Multi-fiber

MCP Billet

(1) Draw single fiber (2) Align single fibers   (3) Draw Multi-fiber   (4) MCP Billet

H_2

MCP wafer

metal

(8) Evaporate electrode   (7) Hydrogen reduction   (6) Chemical-etch   (5) Polish and Slice
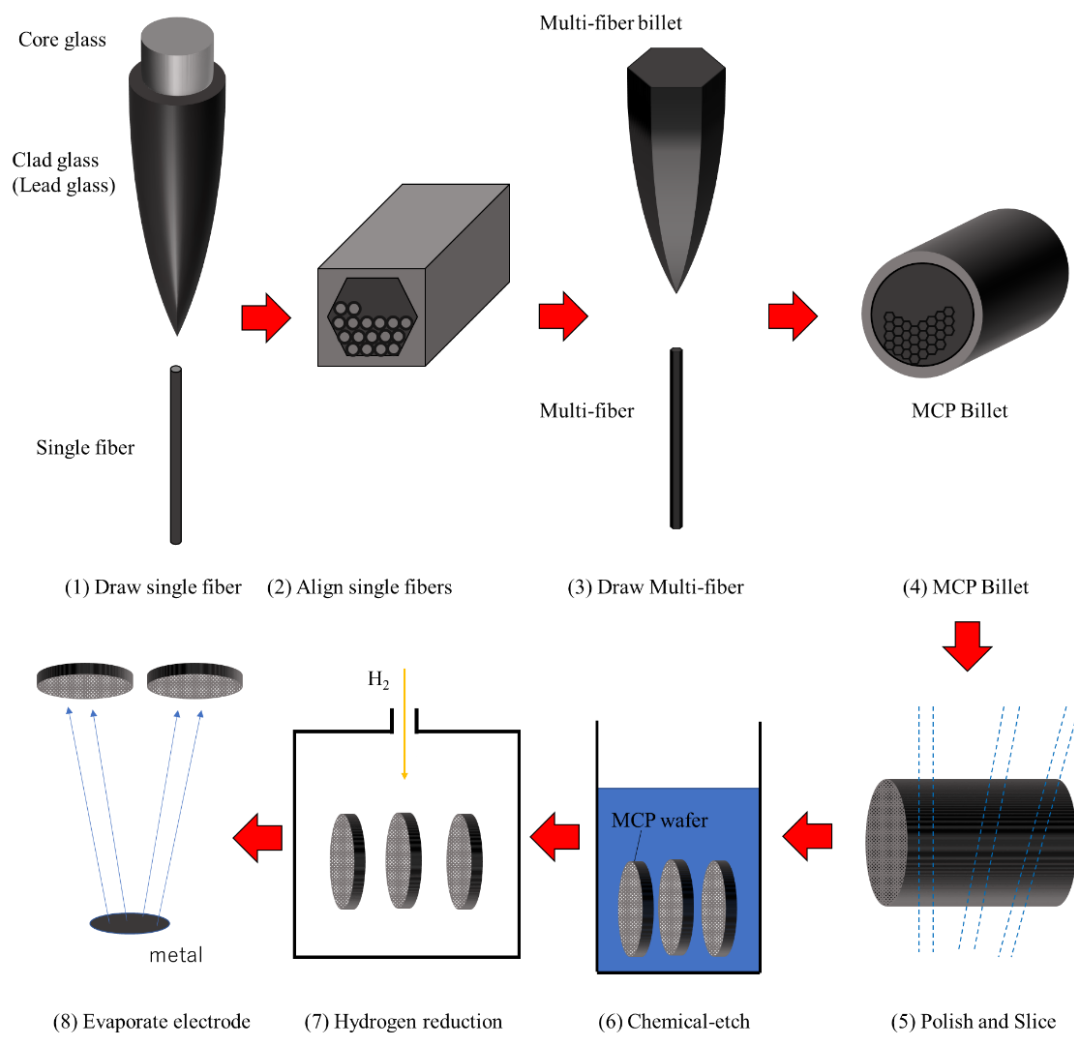
Fig. 2-3. Schematic of MCP production using a two-step glass fiber drawing method.

CHANNEL

CHANNEL WALL

INPUT
ELECTRON

OUTPUT
ELECTRODE

INPUT ELECTRODE

OUTPUT
ELECTRONS

STRIP CURRENT

V_D

THBV3_1001EA

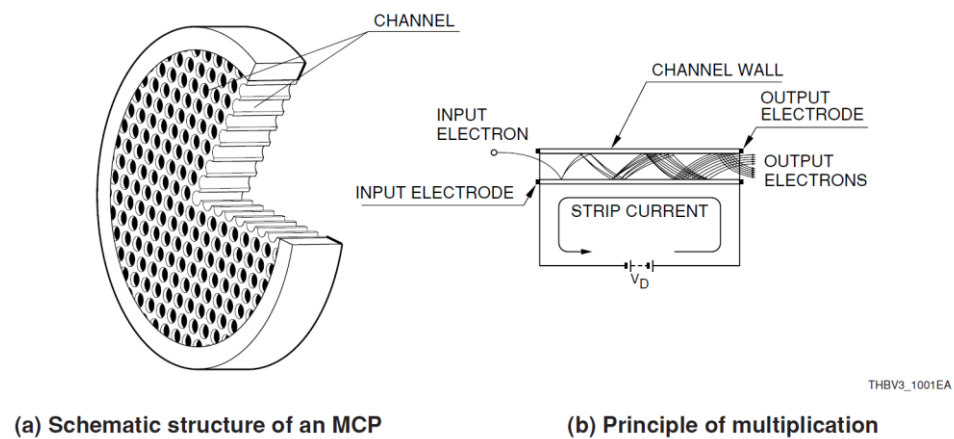(a) Schematic structure of an MCP

(b) Principle of multiplication

Fig. 2-4. Schematic of an MCP and its principle of multiplication.

(Reproduced with permission from Hamamatsu Photonics K.K. [2-17])

2.2 Fundamental characteristics

This section describes the fundamental characteristics of MCPs, such as the gain, time response, and output linearity [2-17]. Figure 2-5 shows the gain characteristics of MCPs depending on α. When α increases, multiplication starts at a higher voltage, and the maximum gain is higher. However, when the gain exceeds 10^4, the noise is increased through 'ion feedback.' The ion feedback phenomenon occurs when multiple electrons ionize residual gas molecules in the channels. The generated ions return toward the MCP input surface because of the electric field along the channel and produce a false signal when they collide with the channel wall. Therefore, the value of α is generally 40–60, so that the gain becomes 10^4 at an applied voltage of 1,000 V. To detect a single particle, two or three MCPs are stacked to obtain a sufficient gain of 10^6. In this case, MCPs were stacked by 180° rotation to each other, as shown in Fig. 2-6. This configuration allows MCPs to operate at high gain because they can absorb the generated ions at the boundary of the MCPs. The two- and three-stacked configurations in Fig. 2-6 are called the chevron and Z-stack, respectively. Figure 2-7 shows the relationship between gain and applied voltage for a single, chevron, and Z-stack MCPs.
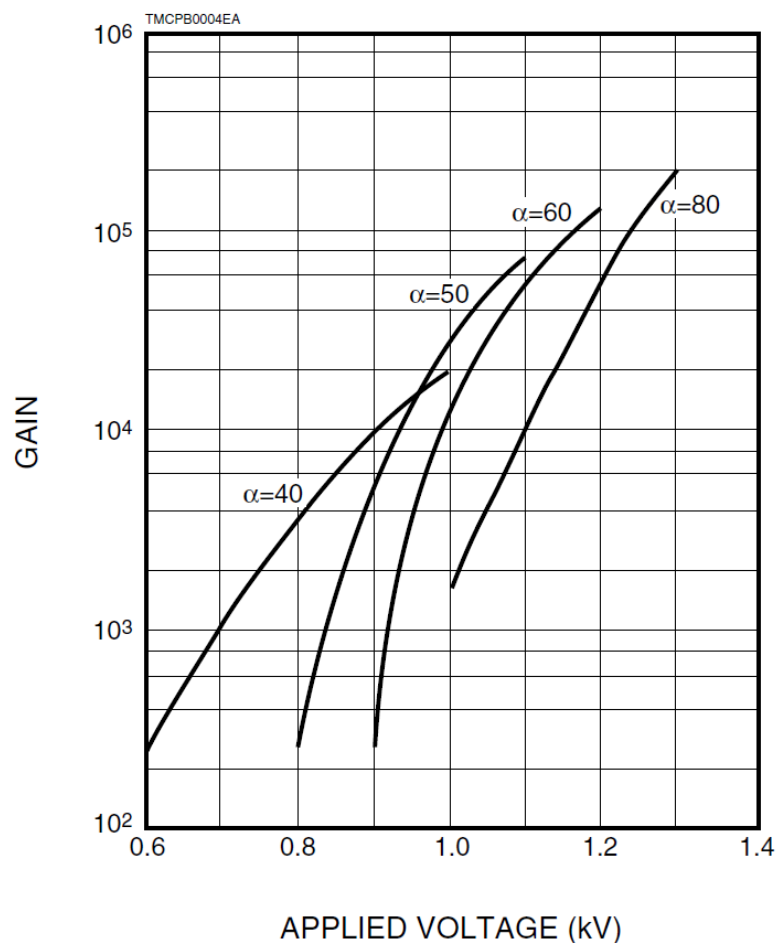
Fig. 2-5. Relationship between the gain and applied voltage for a single MCP.

(Reproduced with permission from Hamamatsu Photonics K.K. [2-17])

Fig. 2-6. Configuration of two-stage (chevron) and three-stage (Z-stack) MCPs.

(Reproduced with permission from Hamamatsu Photonics K.K. [2-17])
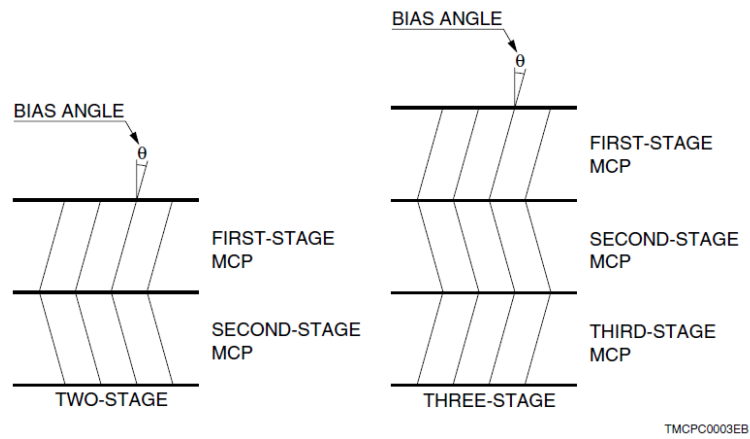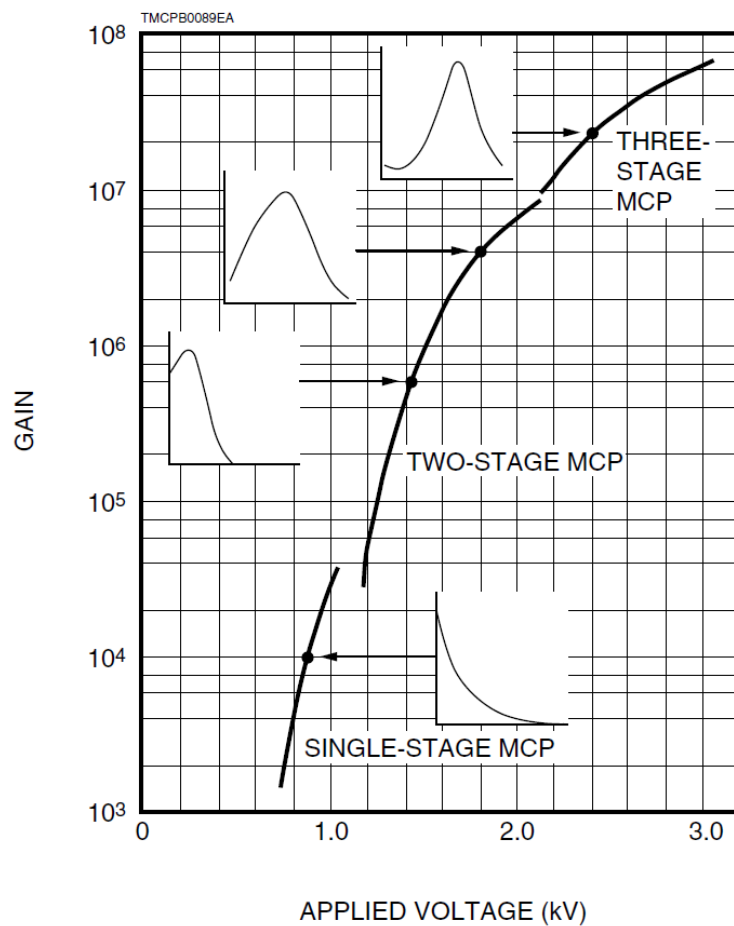

Fig. 2-7. Relationship between gain and applied voltage for single, chevron, and Z-stack MCPs.

(Reproduced with permission from Hamamatsu Photonics K.K. [2-17])

17

Attaching MCPs to the leads (electrodes) and anode is necessary when using them as charged-particle detectors. Figure 2-8 shows the schematic of a typical detector with a chevron MCP (F4655-13, Hamamatsu, Photonics K.K., Hamamatsu, Japan). Because the electron avalanche in the MCP occurs in a strong electric field (greater than 1 kV/mm) with a short transit path, the transit time and jitter of the secondary electrons are significantly shorter than those of the other electron multipliers. Figure 2-9 shows the output waveform of the MCP detector for a single electron. The MCP detector can produce a short pulse of less than 500 ps.
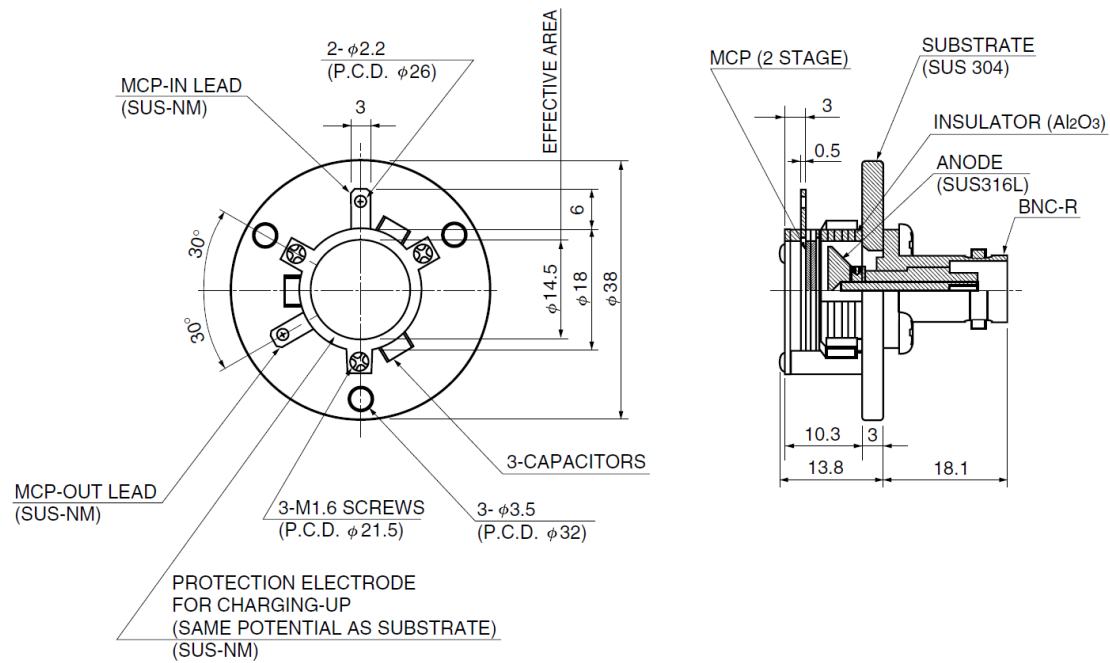
Fig. 2-8. Dimensional outlines of F4655-13 (unit: mm).

(Reproduced with permission from Hamamatsu Photonics K.K. [2-18])

TIME RESPONSE (500 ps/div)

Fig. 2-9. Time response of the MCP detector (F4655-13) for a single electron.

(Reproduced with permission from Hamamatsu Photonics K.K. [2-18])
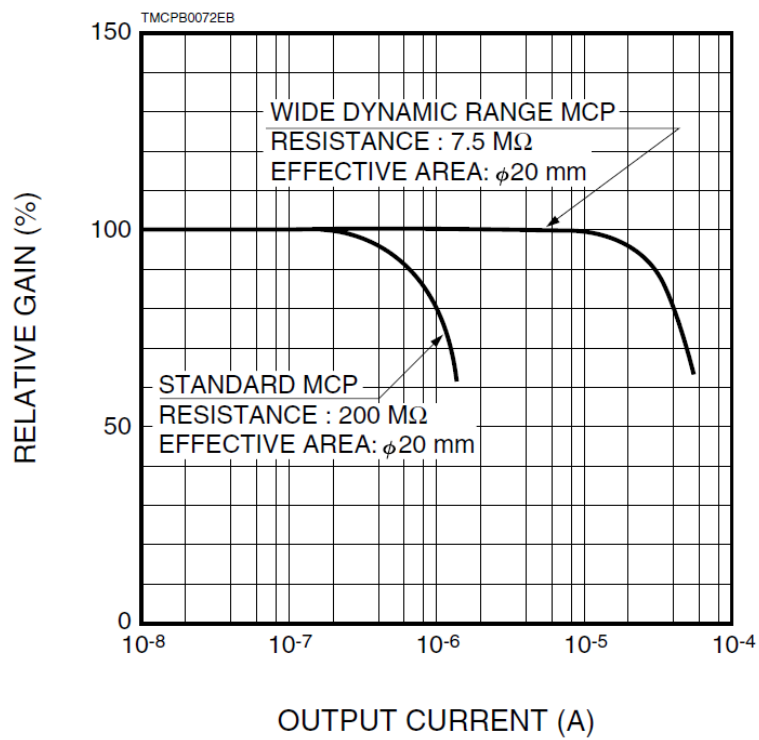
OUTPUT CURRENT (A)

Fig.2-10. Linearity of DC output.

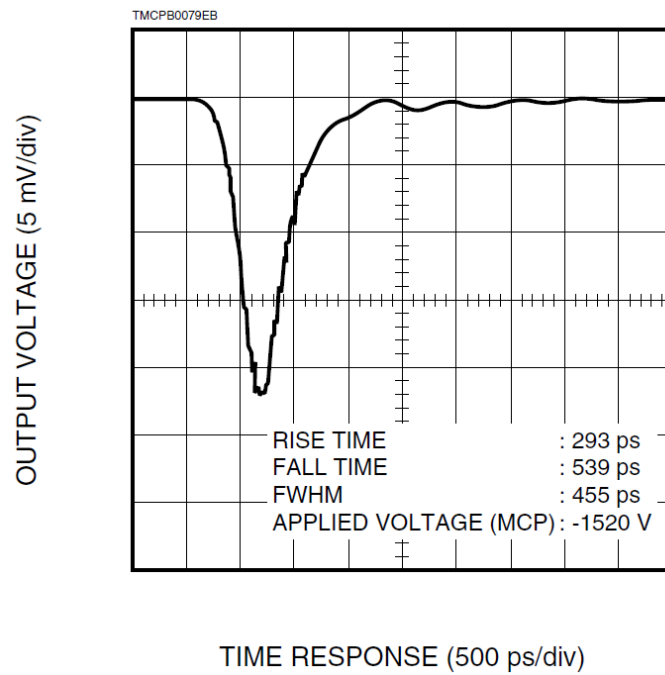(Reproduced with permission from Hamamatsu Photonics K.K. [2-17])

19

Empirically, it is known that the direct current (DC) output of the MCP saturates when it reaches 5%–6% of the strip current (flowing current to the MCP). Upon the output of a large current from an MCP, the walls in the channels near the output surface are charged because of the large amount of secondary electron emission. This surface charge disturbs the potential distribution and changes the electric field, thereby affecting the subsequent amplification. The charges are neutralized by the strip current flowing through the channel surface with high resistance. Figure 2-10 shows the DC output linearities of a normal-resistance MCP (200 MΩ) and a low-resistance MCP (7.5 MΩ). The output current, at which the relative gain starts to decrease, of the low-resistance MCP increased by approximately 30 times that of the high-resistance MCP. Thus, the linearity of the DC output can be improved by reducing electrical resistance. However, there is a limit to reduce the resistance. Because MCP has a negative resistivity temperature coefficient, the electrical resistance decreases with increasing temperature. If the electrical resistance is significantly low such that the Joule heat in the MCP cannot be counteracted, the temperature continues to increase, resulting in the melting of the MCP.

2.3 Applications of MCPs

Because MCPs have a high gain and high-speed response, they have been used in many applications, such as TOF-MS and time-correlated single-photon counting (TCSPC). In TOF-MS, molecules are ionized through some means such as electrospray ionization [2-19] and matrix-assisted laser desorption/ionization (MALDI) [2-20], and the ions are accelerated by the electrical potential, travel through a field-free region, and reach the ion detector. Because the velocities of ions in the field-free region depend on the ratio m/z, m/z can be obtained by measuring the flight time of each ion. The ratio m/z was calculated using the following formula:

$$m/z = 2V\left(\frac{T}{L}\right)^2 \tag{2-6}$$

where V, T, and L are the acceleration voltage, flight time, and flight-path length, respectively. The mass-resolving power R is defined as a specific m/z value (m) divided by the difference in m/z values of ions that can be separated from one another (Δm).

$$R = \frac{m}{\Delta m} \tag{2-7}$$

In a TOF mass spectrometer, the mass-resolving power R can be expressed using T.

$$R = \frac{T}{2\Delta T} \tag{2-8}$$

where ΔT is the minimum difference between the arrival times of the two ions that can be separated. If the detector does not have a sufficiently high-speed response time, it broadens the ion peaks, leading to a deterioration in R. Therefore, MCPs have been used in modern TOF mass spectrometers.

In addition, MCPs have been used in TCSPC, which is an essential technique for measuring the fluorescence decay time [2-21]. The sample was excited using a short laser pulse of a few picoseconds. When a single fluorescent photon was detected, the detection time correlated with the laser irradiation was measured. By repeating this process, a histogram of the detection time for single photons reflecting the fluorescence decay time was obtained. In this technique, the time resolution was determined by the jitter rather than the pulse width of the output signal from the

detector. Therefore, this method can achieve excellent time resolution because the jitter of the output signal from the detector is generally ten times shorter than the pulse width. In addition, the dynamic range of this method is excellent because it is limited only by the photon statistics. Therefore, the TCSPC can simultaneously measure the decay times of both fluorescence and weak phosphorescence.

Although the time jitter of the output signal from the MCP is considerably shorter than that from other electron multipliers, the MCP itself cannot detect fluorescence under visible light. Therefore, MCPs are combined with a photocathode in a vacuum tube and used in a photodetector called an MCP-PMT [2-22]. Figure 2-11 shows a cross-sectional view of the MCP-PMT, containing an input window, a photocathode, two MCPs, and an anode in a vacuum tube. A few hundred volts are generally applied between the photocathode and the MCP input surface to allow photoelectrons from the photocathode to enter the MCP. When a photon enters the photocathode, a photoelectron is generated and then accelerates toward and into the MCP. The photoelectrons are amplified by the MCPs, and the electrons are collected by the anode. The jitter of the MCP-PMTs is also significantly smaller than that of the other PMTs. The jitter of the MCP-PMT (R3809-50U, Hamamatsu, Photonics K.K., Hamamatsu, Japan) was evaluated as 25 ps at full-width at half maximum using the measurement system shown in Fig. 2-12 [2-22].
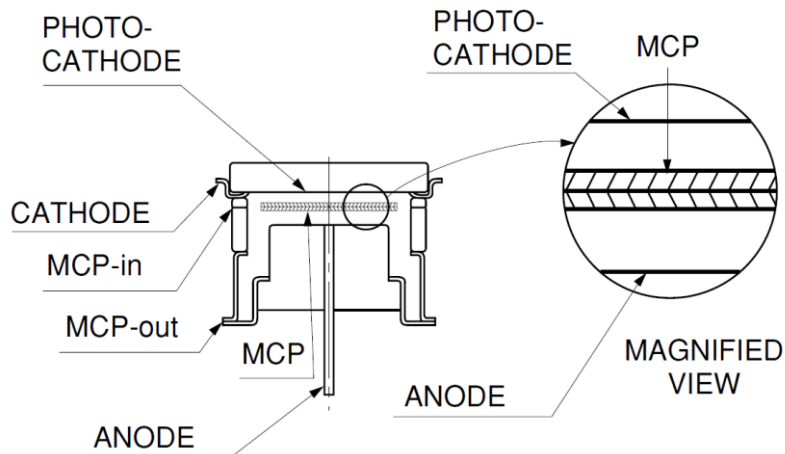
Fig. 2-11. Schematic of the cross-sectional view of typical MCP-PMT.

(Reproduced with permission from Hamamatsu Photonics K.K. [2-22])
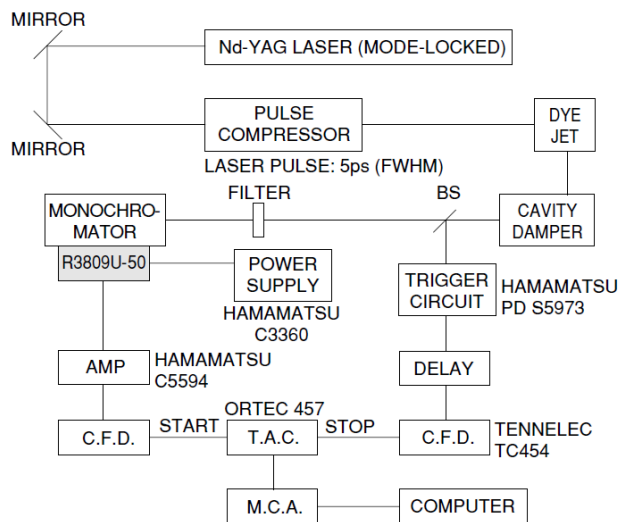
Fig.2-12. Experimental setup to evaluate the jitter of MCP-PMT(R3809U-50).

(Reproduced with permission from Hamamatsu Photonics K.K. [2-22])

References

[2-1]   J.J. Thomson, The Philosophical Magazine 6 (1912) 209–253.

[2-2]   A.J. Dempster, Physical Review 2 (1918) 316–325.

[2-3]   J. Koeigsberger, J. Kutchewski, Physikalische Zeitschrift 11 (1910) 666.
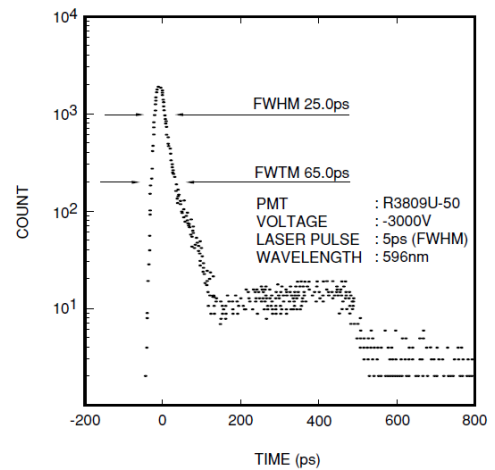
[2-4]   J.J. Thomson, The Philosophical Maga 21 (1911) 225–249.

[2-5]   B.K. Lubsandorzhiev, Nuclear Instruments and Methods in Physics Research Section A: Accelerators, Spectrometers, Detectors and Associated Equipment 567 (2006) 236–238.

[2-6]   V.K. Zworykin, G.A. Morton, L. Malter, In Proceedings of the Institute of Radio Engineers 24 (1936) 351–375.

[2-7]   V.V. Zworykin, J.A. Rajchman, In Proceedings of the IRE 27 (1939) 558–566.

[2-8]   P.T. Farnsworth, Electron Multiplier, US1969399, 1930.

[2-9]   G.W. Goodrich, W.C. Wiley, Review of Scientific Instruments 33 (1962) 761–762.

[2-10]   J. Adams, B.W. Manley, IEEE Transactions on Nuclear Science 13 (1966) 88–99.

[2-11]   J.L. Wiza, Nuclear Instruments and Methods 162 (1979) 587–601.

[2-12]   E.H. Eberhardt, Applied Optics 18 (1979) 1418.

[2-13]   W.C. Wiley, C.F. Hendee, IRE Transactions on Nuclear Science 9 (1962) 103–106.

[2-14]   D. Washigton, V. Duchenois, R. Polaert, R.M. Beasley, Acta Electronica 14 (1971) 201–224.

[2-15]   A. O'Mahony, C.A. Craven, M.J. Minot, M.A. Popecki, J.M. Renaud, D.C. Bennis, J.L. Bond, M.E. Stochaj, M.R. Foley, B.W. Adams, A.U. Mane, J.W. Elam, C. Ertley, O.H.W. Siegmund, Journal of Vacuum Science and Technology A 34 (2016) 01A128.

[2-16]   Yu. Melikyan, T. Sýkora, T. Komárek, L. Nožka, D. Serebryakov, V. Urbášek, Nuclear Instruments and Methods in Physics Research Section A: Accelerators, Spectrometers, Detectors and Associated Equipment 949 (2020) 162854.

[2-17]   Technical Information MCP Assembly, Hamamatsu photonics K.K., 2016.

[2-18]   Hamamatsu Photonics K.K., Catalog of MCP ASSEMBLY FOR HIGH RESOLUTION TOF-MS F4655-13, 1998.

[2-19]   J.B. Fenn, M. Mann, C.K. Meng, S.F. Wong, C.M. Whitehouse, Science 246 (1989) 64–71.

[2-20]   M. Karas, D. Bachmann, U. Bahr, F. Hillenkamp, International Journal of Mass Spectrometry and Ion Processes 78 (1987) 53–68.

[2-21]   I. Yamazaki, N. Tamai, H. Kume, H. Tsuchiya, K. Oba, Review of Scientific Instruments 56 (1985) 1187–1194.

[2-22]   Hamamatsu Photonics K.K., PHOTOMULUTIPLIER TUBES -Basics and Applications- Third Edition (Edition 3a), 2007.

3. Evaluation of gain-recovery time by ion irradiation

3.1 Introduction

As described in the previous chapter, the detectors with the microchannel plates (MCPs) are suitable for time-of-flight (TOF) mass spectrometers because of the high-gain and fast time response. However, it is also well known that the gain temporarily drops when other high ion-flux signals are detected. Beavis et al.[3-1] reported that the detection of proteins was inhibited by gain drops caused by large amounts of matrix-derived low-mass ions in matrix-assisted laser desorption/ionization (MALDI) mass spectrometry. They noted that the drop in detector gain with high low-mass ion fluxes is of substantial practical importance. In addition, Westman et al.[3-2] quantitatively presented saturation effects in chevron MCP detectors by switching the detector voltage at various time points during the course of a single TOF spectrum acquisition. They reported that when the front plate voltage of an MCP detector was set to the target value (800 V) from the beginning, no peak corresponding to cytochrome c was observed. However, it can be detected with a high sensitivity when the front plate voltage was set low and then switched to 800 V at the timing of TOF for cytochrome c. Such gain drops on TOF mass spectrometers have been reported; however, the fundamental principles responsible for this phenomenon have not been investigated yet. The mechanism for MCP gains in imaging detectors for photons have been studied by comparing mathematical models and experimental results under various count rates to understand the artifacts on the obtained images. Sams [3-3] reported that PAPA (precision analog photon address) cameras of photon-counting imagers employing MCPs used for astronomical speckle imaging could produce artifacts when light incident on its MCP image intensifier was highly concentrated. The artifacts depend on the local photon concentration at the input face of the camera, and result from the

25

dynamical photon "gain depression" of the MCP. In addition, in the TOF photoelectron spectrometer, Anacker et al. [3-4] exhibited "gain saturation," in which the MCP gain deteriorates. This phenomenon was assumed to be related to the active channels in which output electron fluxes deactivate the quiescent neighboring channels, the mechanism of which has been modeled as "pore bleaching." Fraser et al. [3-5,6] had investigated the fundamentals of the MCP gain drop using photons in detail, as described below.

A computer model of the channel plate performance was developed by Guest [3-7], and the mathematical model of gain has been discussed by Eberhardt [3-8]. Moreover, Giudicotti et al. [3-9] established a mathematical model that focused on "gain saturation," a phenomenon in which the MCP gain drops if the input LED illumination pulse interval is smaller than the recharging time constant RC. An area of the channel wall needs to be recharged before the next event or drops gain. The normalized voltage across the capacitor (V_c) during the charging period on a simple recharging circuit can be represented as follows:

$$V_c = 1 - \exp\left(-t/RC\right) \tag{3-1}$$

where t is the time and R and C are the resistance and capacitance of the entire MCP, respectively. Fraser et al. [3-5] reported the gain behaviors of MCP detectors using X-ray or UV illumination with 13 different models and MCP configurations such as single, chevron, and z-stacked; the individual plate resistance ranged from 27 to 2,450 MΩ. They assumed that the charge instantaneously removed from a channel is exponentially replenished with a time constant τ, which is a product of k, resistance (R), and capacitance (C) represented as:

$$\tau = kRC \tag{3-2}$$

where k embodies the properties of an unknown channel recharge circuit in their model, which depends on the effective area of illumination, the configuration (i.e., single or multiple stages), the channel diameter, the illumination (beam spot) area, and the model of the MCP detector. They noted that the possible k factors vary from 2 to 12 for single-stage MCP detectors and in the order of 100 for multistage MCP detectors. They also reported that the k factor is independent of the illumination area in single-stage MCP detectors but highly dependent on the area in multistage MCP detectors. However, in the case of a "point-like" illumination area, even in multistage MCP detectors, the obtained k factors behave similarly to single-stage MCP detectors. The measured dependence of the multistage MCP detector recovery time (time constant τ) on the illuminated area was interpreted in terms of "interchannel coupling" or "adjacency" [3-10] of each channel of MCP. Finally, Fraser et al. [3-6] confirmed in detail the "pore bleaching" hypothesis of Anacker et al [3-4]. They presented the radial "gain suppression," a local gain as a function of distance from high count-rate spots by using a position-sensitive MCP detector and measuring the structured UV images using a sheet of transparent photographic film containing a central pin-hole with a diameter of ~0.5 mm. They noted that it is likely that the adjacency observed in the macroscopic behavior of chevron or Z-stack MCP detectors arises, on a microscopic level, from the transverse electric fields set up, over distances of some millimeters, by active microchannel groups. They proposed another MCP gain model named "reservoir model" described in the next section. However, these studies used only photons (UV or X-ray) without a sophisticated monochromator. Such photon-based experimental conditions irradiate a large number of photons per event, which generates homogeneous irradiation in many of the microchannels. In contrast, in TOF mass spectrometry, the irradiation of only less than one ion per microchannel per event might occur. As a result, such a photon-based method is not suitable for studying the gain-drop phenomenon observed by MALDI mass spectrometry, wherein no protein peaks were observed because of high ion-flux detection in the low-mass region. This phenomenon

has also been reported for polymer analysis using MALDI mass spectrometry [3-11]; however, its mechanism is yet to be investigated using ions because of the lack of a method that can control the TOF of an ion at a controlled time delay for a duration between 10^{-6} and 1 s.

In this chapter, the method to measure the gain-drop rate as a function of Δt using a pair of ions on a multi-turn TOF mass spectrometer, which can extract an ion without disturbing the flight of other ions, was developed. By using this method, the gain recovery time constants of two chevron MCP detectors were also evaluated.

Reservoir model

A region of MCP loses gain if the detection event depleted all electrons, which, however, can be recovered by recharging, as described in Eq. (3-1). The recharge models were discussed standing on the "dead-time," where the detector will not respond for a given time. It is also split into models whether "dead-time" will be extended (paralyzable model [3-5]) or not (non-paralyzable model [3-10]) by another detection event during the "dead-time." Both models have been discussed, assuming that every pulse fully depletes; however, this assumption is intuitively unphysical. Fraser et al. [3-6] discussed a more sophisticated analytical model called "reservoir model [3-12]." As shown in Fig. 3-1, it considers the evolution of charge in a reservoir of fixed depth, which represents in the G_{max}. The gain of a given pulse then depends on the magnitudes and temporal spacings of previous pulses. Westman et al. [3-2] reported that the peak of cytochrome c becomes smaller when the voltage of the detectors switches earlier. This observation can be explained quite well using the reservoir model. Although this model is simple and reasonable, no experimental evidence for the existence of such reservoirs has been reported yet.
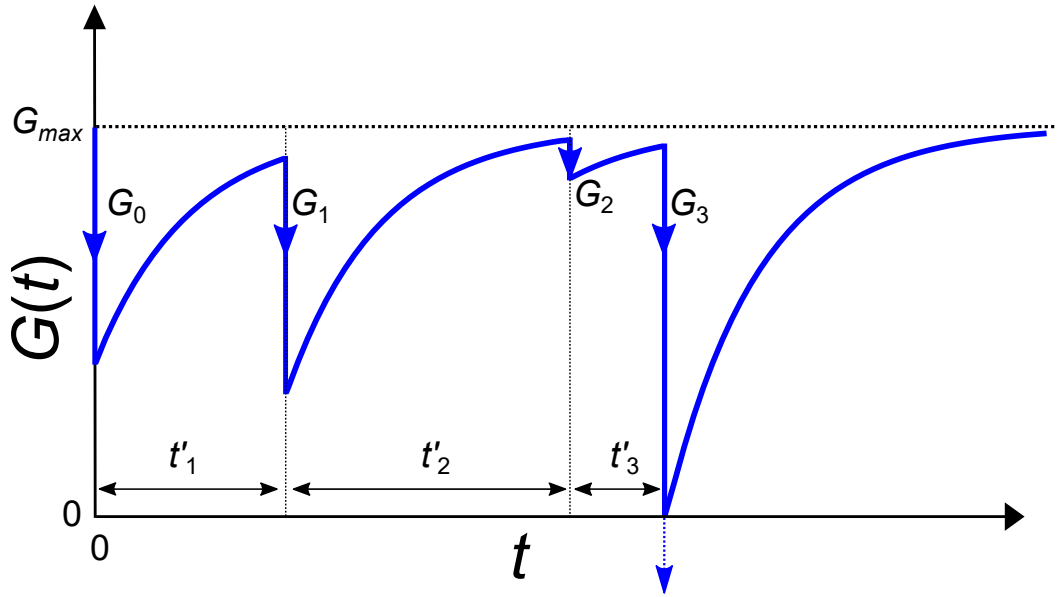
Fig. 3-1. Evolution of charge in a reservoir with depth G_{max}. The photon arrival times t'_n (n = 1, 2, 3 …) are random. The G_n (n = 0, 1, 2 …) corresponds to charges to deplete by detection event that is identical to peak height, which the height of each peak follows pulse height distribution. In this example, the G_3 has been limited by the finite reservoir depth.

3.2 Experimental

A miniaturized multi-turn TOF mass spectrometer [3-13] infiTOF-UHV (infiTOF) (MSI. Tokyo, Inc., Tokyo, Japan) was used with in-house modifications as reported previously [3-14,15]. Since the figure-of-eight orbit of the mass analyzer comprises a slit (hole) of 1 mm diameter and an additional exit hole to the detector of 2.5 mm diameter, the beam irradiation diameter on the detector surface is considered to be 1–2.5 mm. The ion beam diameter at the detector was assumed to be 1 mm hereafter for related calculations.

Two chevron MCP detectors were prepared using F1551-01 and F1551-011 (Hamamatsu Photonics K.K., Hamamatsu, Japan) and were named MCP 1 and MCP 2, respectively. The channel diameter for both the microchannel plates in each chevron MCP detector was 12 μm, with an open-

area fraction of 0.6. Each chevron MCP detector was assembled into the housing [3-16] as a detector assembly and stored in a vacuum desiccator until required for use. Table 3-1 lists the parameters of the microchannel plate combinations employed herein. The resistance listed in the table was obtained from the inspection sheet shipped with the product. The capacitances were experimentally obtained, as described later in this section.

As shown in Fig. 3-2, the MCP IN potential was set to −5.0 kV, and the GND plate with a 2.5-mm-diameter slit was placed between the MCP detector and the mass analyzer. The slit was covered by a mesh of 40-μm width and 500-μm pitch. The detector was mounted on the back of the infiTOF ejection sector at the time of use. The detector signal was passed through a 30-dB attenuator (AT-130V, Hirose Electric Co., LTD., Tokyo, Japan) and a preamplifier (model C11184, Hamamatsu Photonics K.K., Hamamatsu, Japan), followed by waveform acquisition using an Acqiris U5303A 1GSs^{-1} high-speed digitizer (Acqiris, Geneva, Switzerland). Data acquisition and analysis were performed using the open-source software "QtPlatz" (https://github.com/qtplatz) with its plugin for infiTOF.

Table 3-1. MCP detector assembly parameters employed in the experiment. The open-area fraction was 0.6 for both MCPs.

Name	MCP parts-number	serial number	bias angle	channel diameter	effective diameter	plate thickness	resistance	capacitance
MCP 1	F1551-01	A015482 A015505	8°	12 μm	14.5 mm	0.48 mm	500 MΩ	6.5 pF
MCP 2	F1551-011	AC2270 AC2271	12°	12 μm	14.5 mm	0.48 mm	71 MΩ	6.5 pF
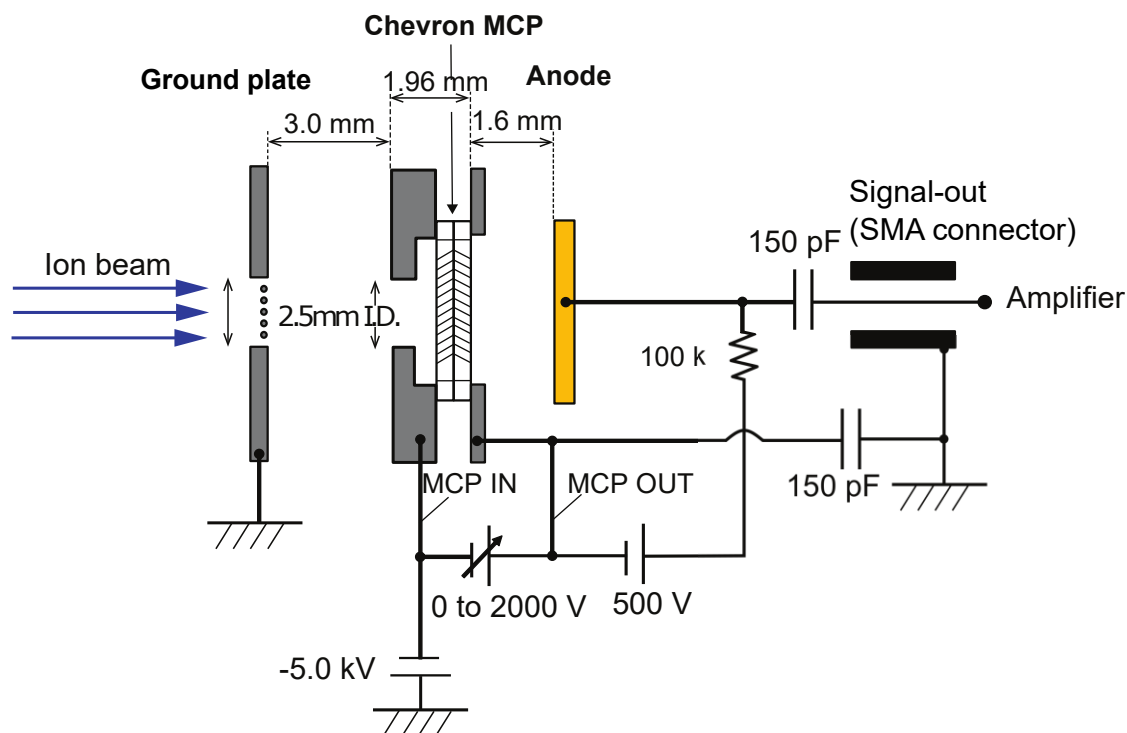
Fig. 3-2. Schematic representation and experimental setup for the MCP 1 and MCP 2 detectors.

The modal response value for a single argon ion at a low count rate was determined with an area moment for the full width at half maximum fraction of the bell curve obtained from the single argon peak height distribution under the given MCP IN-OUT voltage. Modal responses of 34 and 31 mV were obtained at MCP IN-OUT voltages of 1,740 and 1,570 V for MCP 1 and MCP 2, respectively. The argon ion count rates while determining the modal responses were 209 and 135 counts per second per plate for MCP 1 and MCP 2, respectively, which correspond to 0.05 and 0.03 counts per second per channel, respectively, estimated by assuming a 1-mm diameter for the ion beam and the MCP parameter.

Reagent-grade xenon gas (Takachiho Chemical Industrial Co., Ltd, Tokyo, Japan) was introduced into the electron ionization (EI) chamber using a PEEK (polyether ether ketone) capillary tubing of

1 m in length and 0.1 mm inner diameter. The ionization chamber pressure was maintained at 3.4×10^{-3} Pa while introducing the sample (the pressure when the sample-introduction valve was closed was 2.2×10^{-4} Pa). The ionization energy was set to 30 eV.

The capacitance of each MCP in the MCP detector was measured as the output amplitude from the MCP under 100 kHz, with an amplitude of 5.36 V at a pressure of 1.3×10^{-3} Pa. A digital oscilloscope (model DSOX6004, Keysight Technologies, Inc., Santa Rosa, California, US) with a function generator was used to supply power and determine the output amplitude. The electrical circuit for this experiment is shown in Fig. 3-3. The observed amplitudes from the single MCPs were 1.7 V for F1551-01 and F1551-011, respectively. Using these results, the overall capacitances of the experimental circuit were calculated as (47 ± 2) pF for both MCPs in the MCP detector. The amplitude obtained from the experimental circuit without an MCP was 2.94 V, corresponding to (23 ± 0) pF; hence, the capacitance of a single MCP was determined to be (24 ± 2) pF. The capacitance of the rim (i.e., the solid glass edge of the MCP) was calculated to be 11 pF from the MCP dimensions and the relative permittivity of soda-lime-silica glass (6.9) as obtained from the literature [3-17]. Therefore, the capacitance of a rimless MCP was assumed to be (13 ± 2) pF. The total capacitance of two MCPs stacked in series was (6.5 ± 0.7) pF.
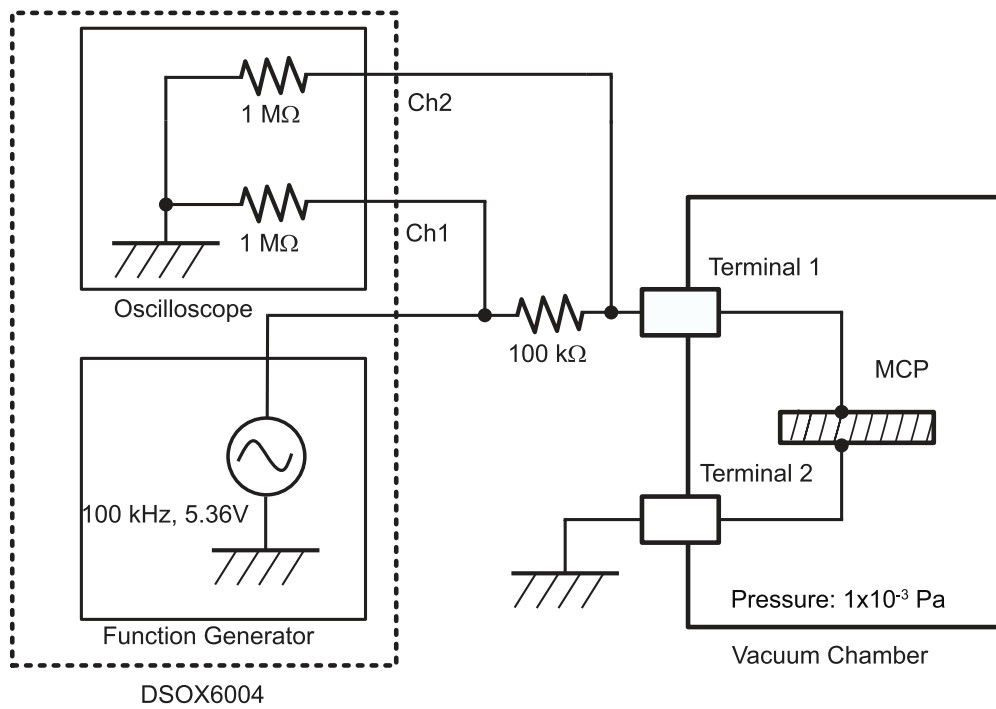
Fig. 3-3. Schematic representation of the apparatus employed for the capacitance determination experiments.
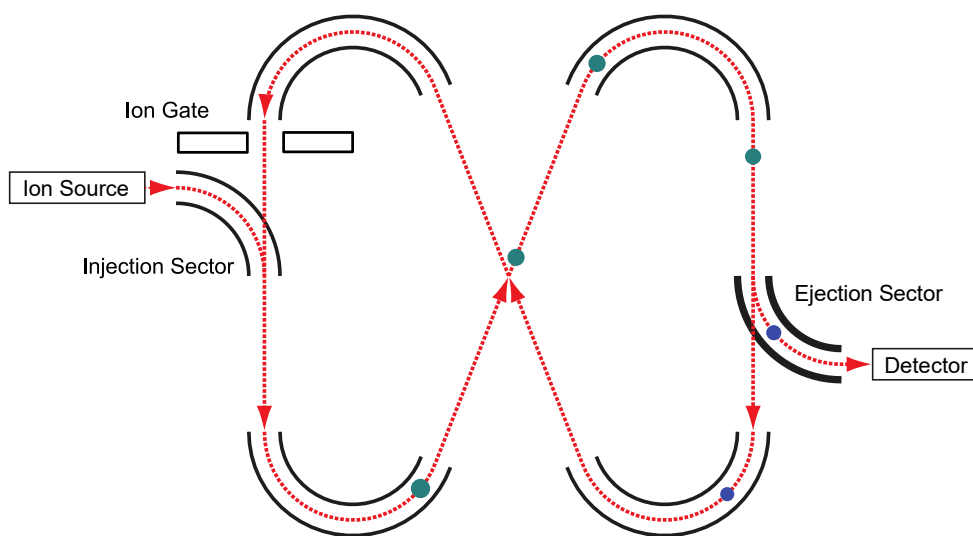

Fig. 3-4. Electric sector layout and ion trajectory.

3.3 Results and Discussion

Xenon is an excellent material to study detector gain drops from the peak area ratio changes because of its unique isotope cluster distribution. A novel method was developed to exclude $^{130}Xe^+$ and $^{131}Xe^+$ by electric sector control and manage the time difference (Δt) between $^{129}Xe^+$ and $^{132}Xe^+$. The MCP detector was irradiated with $^{129}Xe^+$ as the first detection event to cause the gain drop and the response for $^{132}Xe^+$ was measured while changing Δt.

Two methods were used to investigate the relationship between Δt and gain. In these methods, two ions (i.e., $^{129}Xe^+$ and $^{132}Xe^+$) were detected sequentially for a series of TOF differences ranging from microseconds to subseconds using a multi-turn TOF mass spectrometer. In the first method, an ion such as $^{129}Xe^+$ is withdrawn and detected at a given lap number without disturbing other isotopes, and then the ions remaining in the analyzer are extracted and detected a few laps later as a single TOF event [3-15]. Figure 3-4 schematically represents the ion trajectory of the analyzer. The xenon ions were injected into a figure-of-eight orbit from the ion source, and then unwanted ions are rejected by turning on the ion gate. Figure 3-5 shows the timing diagram that controls each electric sector for "protocol 0" (p0) and "protocol 1" (p1). These protocols are alternatively switched in sequence. Protocol 0 opens an ejection sector for 700 ns after 87 μs on the TOF time domain, which extracts ten-laps of $^{129}Xe^+$ from the figure-of-eight orbit to irradiate the detector. All the other ions continued to fly without disturbing their motion. And then, $^{132}Xe^+$ was selected and introduced into the detector at a series of lap numbers, i.e., 12, 14, and 16, which resulted in a TOF difference Δt for a series of n-folds of the orbital period (8.258 μs) for $^{132}Xe^+$, where n is the lap number difference between $^{129}Xe^+$ and $^{132}Xe^+$. Protocol 1 set the same timing with p0 for $^{132}Xe^+$ detection except for no $^{129}Xe^+$ irradiates the detector at all. Two protocols, p0 and p1, correspond to the $^{129}Xe^+$ detection on and off, which makes two spectra shown in Fig. 3-6 alternatively. Therefore, two $^{132}Xe^+$ peak areas were compared in all cases, i.e., p0 and p1, where p0 is affected by $^{129}Xe^+$, while p1 is not.

34

This method may cancel and compensate for the instrumental intensity drift for long experimental procedures as well as ion transparency changes between the lap numbers. Also note that the ^{132}Xe$^+$ peak obtained from p0 is known as the "dependent peak," while that obtained from the p1 is known as the "independent peak." In the previous work, the variation in the xenon isotope abundance ratio when a monoisotopic ion was withdrawn at an early lap number was reported to be less than 1.55% [3-18].

The second method, as illustrated in Fig. 3-7, involves combination of the ion-push-repetition rate change with the protocol sequence, where p0 withdraws only ^{129}Xe$^+$ and p1 withdraws only ^{132}Xe$^+$. The obtained Δt between ^{129}Xe$^+$ and ^{132}Xe$^+$ is the sum of the ion-push interval and TOF difference of ^{129}Xe$^+$ and ^{132}Xe$^+$. An additional protocol (p2) was added, in which no ions were ejected from the analyzer after waiting for a sufficient time (minimum of 8 ms until the next protocol). Furthermore, protocol 3 (p3) detects only ^{132}Xe$^+$, which represents the no-gain-dropped peak response. The ion-push-repetition time can be set as any time in the range from 1 ms to 500 ms with a resolution of 0.001 ms, which can rapidly result in variations in Δt up to 500 ms. One drawback of this method is that the last ^{132}Xe$^+$ detection suppresses the peak intensity of ^{129}Xe$^+$; Δt for ^{129}Xe$^+$ from the last ^{132}Xe$^+$ detection is approximately 500 µs. However, the ^{129}Xe$^+$ peak height >300 mV was maintained. Here, the ^{132}Xe$^+$ peak obtained from p1 is the "dependent peak," where the gain affected by ^{129}Xe$^+$ is on p0, and the peak obtained from p3 is considered the "independent peak."
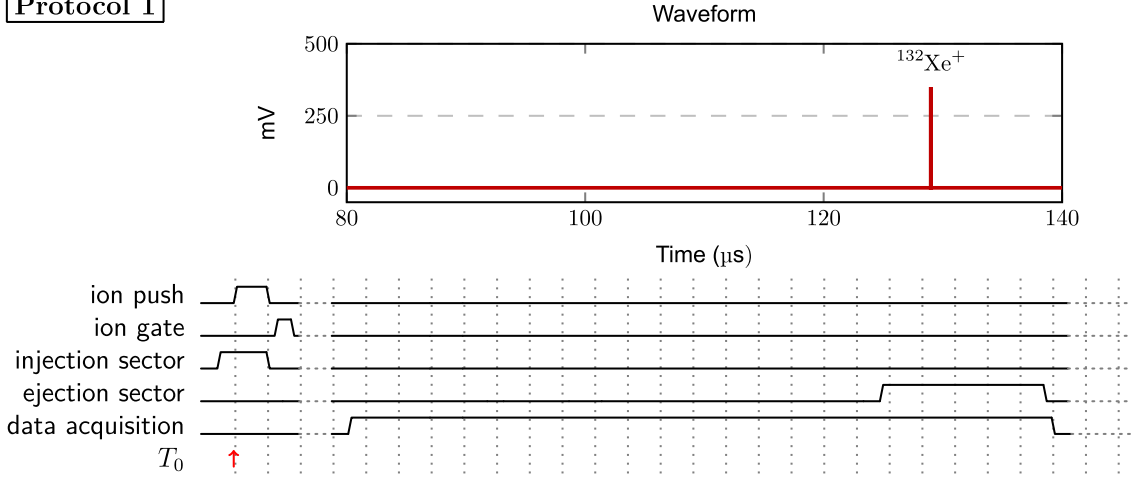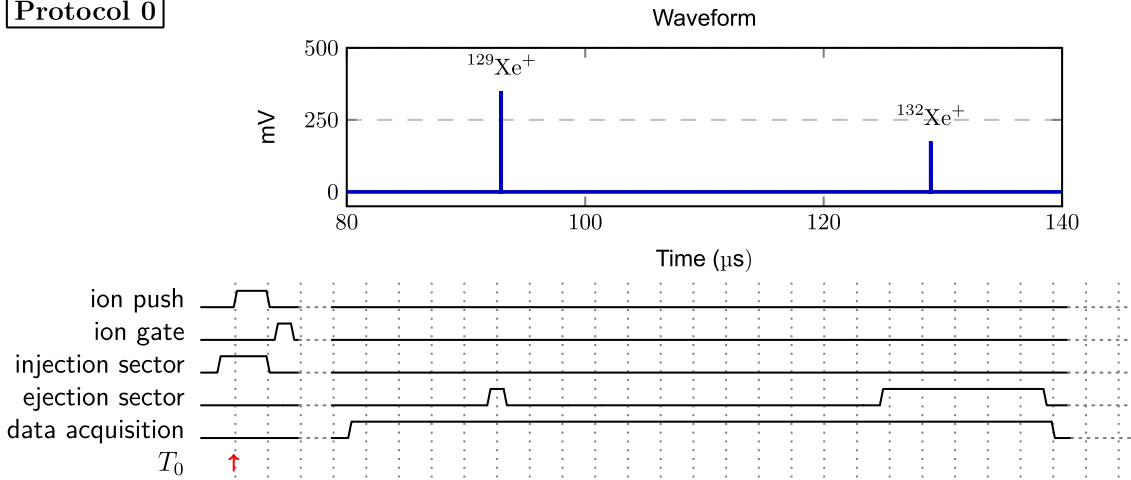
Fig. 3-5. Schematic diagram for the selective extraction of monoisotopic ion. The "protocol 0" (p0) (bottom) extracts ^{129}Xe$^+$ by opening an ejection sector for 700 ns after 87 µs on the TOF time domain. All the other ions continued to fly without disturbing their motion, and then the ejection sector turned on at a given lap number. Protocol 0 makes a spectrum contains ^{129}Xe$^+$ and ^{132}Xe$^+$ with a given time difference between them by a lap number difference. In contrast, "protocol 1" (p1) (top) makes a spectrum where no ^{129}Xe$^+$ is detected at all.
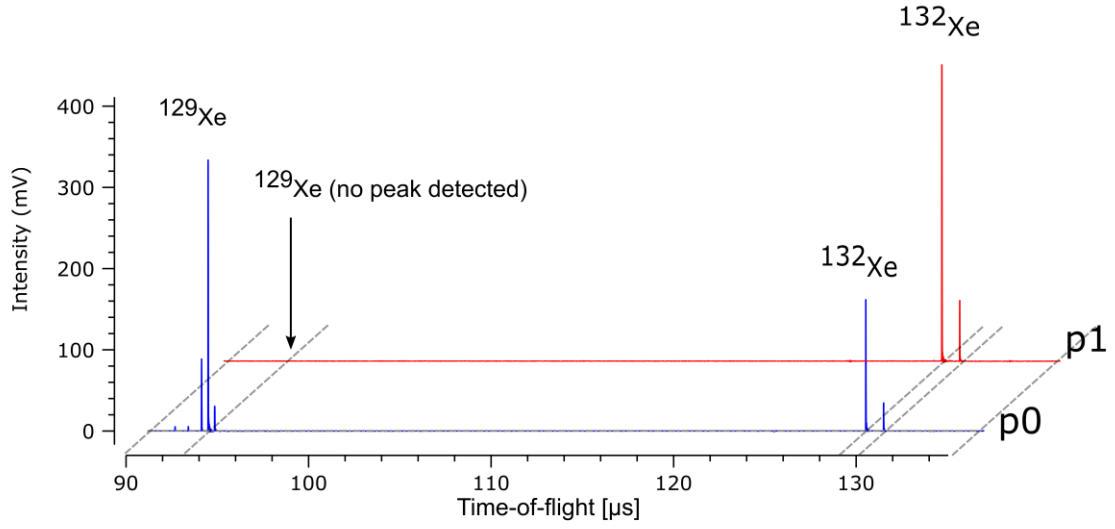
Fig. 3-6. Xenon acquisition protocols and obtained spectra. The bottom and top spectra correspond to p0 and p1, respectively, where p0 withdraws $^{128}Xe^+$, $^{129}Xe^+$, and $^{130}Xe^+$ at 10 laps, and then detects $^{132}Xe^+$ and $^{134}Xe^+$ at 14 laps. The p1 protocol detects $^{132}Xe^+$ and $^{134}Xe^+$ at 14 laps without detecting any other ion beforehand. The TOF for 10 laps of $^{129}Xe^+$ and 14 laps of $^{132}Xe^+$ were 92.952 and 128.985 μs (Δt = 36.03 μs). The peak areas for 14-lap $^{132}Xe^+$ for p0 and p1 were corresponding to 38 and 84 pC, respectively (ratio = 0.45). The detector conditions were as follows: MCP 1 with an MCP IN-OUT voltage of 1,740 V. The EI filament was set to 3,640 mA. The ion-push-repetition rate was set to 100 Hz.
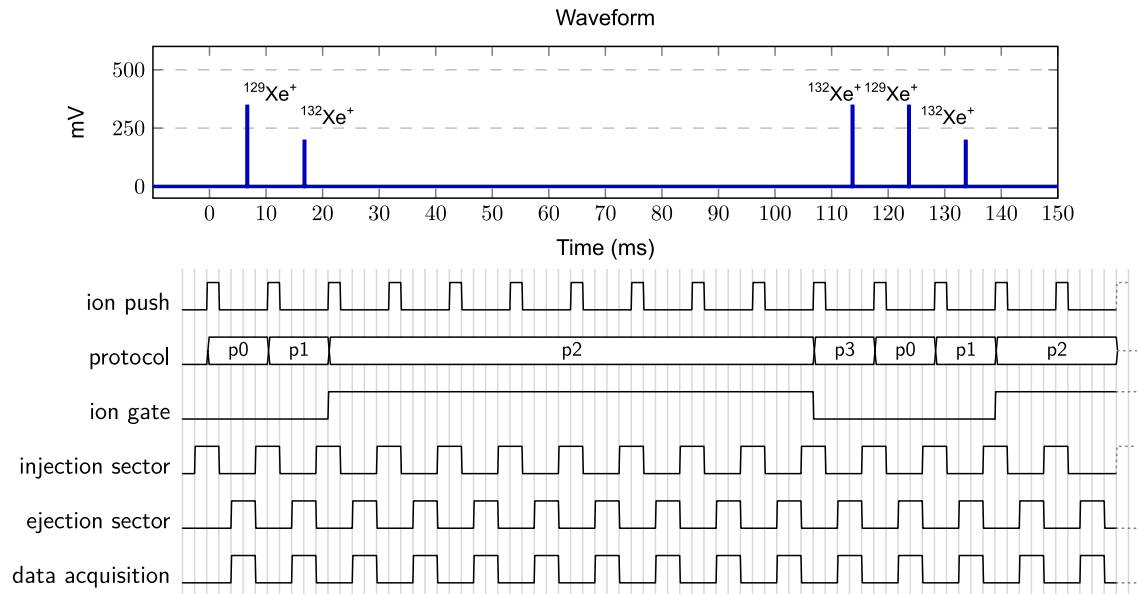
Fig. 3-7. Ion-push repetition and protocol sequence to gain-drop monitoring. Protocol zero (p0) detects only $^{129}Xe^+$; protocol 1 (p1) and protocol 3 (p3) detect only $^{132}Xe^+$; protocol 2 (p2) excludes all ions that are replicating eight times, thereby providing enough time to fully recharge the detector. Therefore, the subsequent $^{132}Xe^+$ intensity on p3 represents a full gain response.
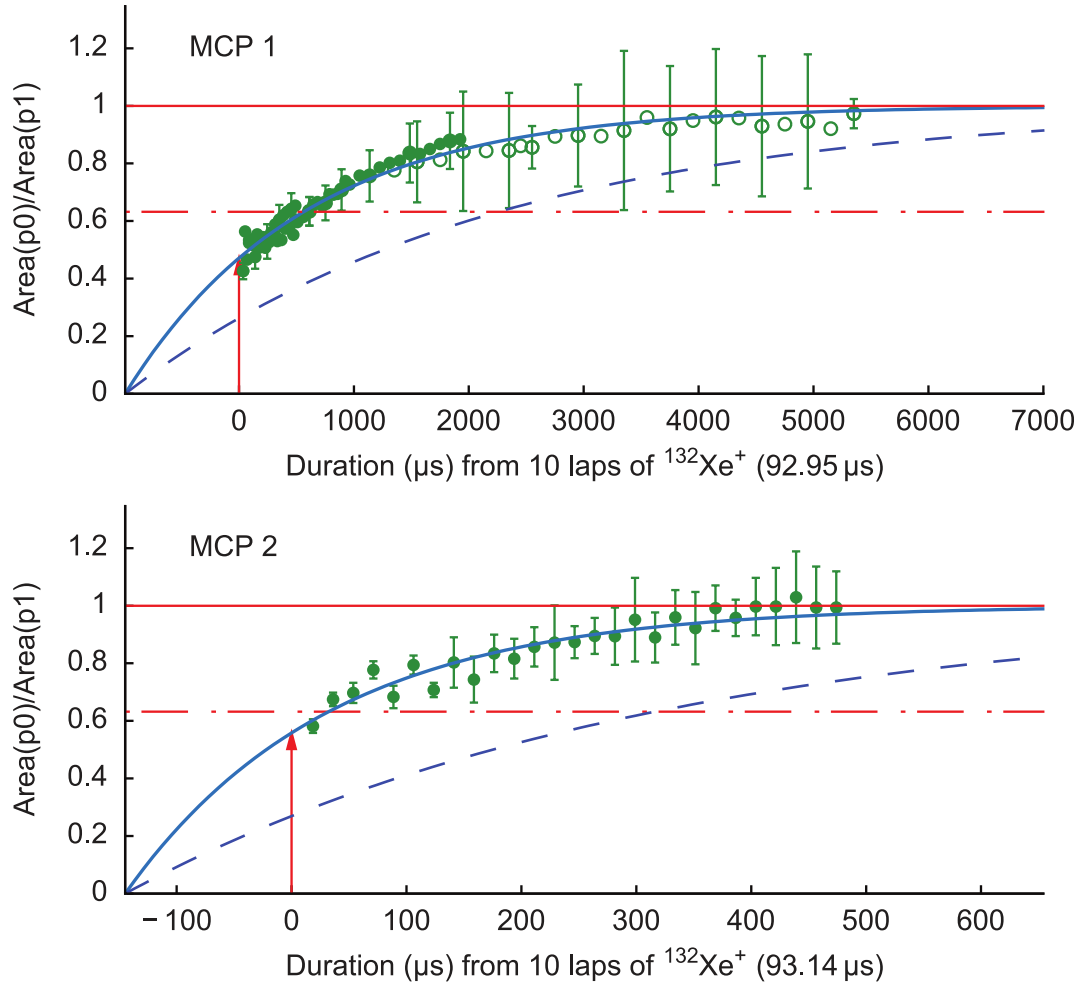
Fig. 3-8. Time-course of ^{132}Xe$^+$ peak area ratio p0/p1. The detector conditions were as follows: MCP 1 with an MCP IN-OUT voltage of 1,740 V, and the EI filament was set to 3,640 mA. Closed circles represent the first method (Figs 3-5 and 3-6) described in the text, while open circles represent the second method (Fig. 3-7). Vertical arrows indicate t_0 where ^{129}Xe$^+$ was detected. MCP 2 with an MCP IN-OUT voltage of 1,570 V; the EI filament was set to 3,850 mA. Dashed lines represent RC charging curves $V_c = 1 - \exp(-t/RC)$ calculated from the externally obtained capacitance and resistance shown in Table 3-1. The time-constant values estimated from curve fitting were 1,600 and 180 μs for MCP 1 and MCP 2, respectively. The curve fits against the RC models obtained for MCP 1 and MCP 2 were $G_t = 1 - \exp\left(\frac{-(t+990)}{1600}\right)$, and $G_t = 1 - \exp\left(\frac{-(t+150)}{180}\right)$, respectively.

39

The time-course for the relative gain calculated as the area ratio of the "dependent peak" over the "independent peak" is shown in Fig. 3-8. One of every 100 waveforms was co-added and stored in the data file as a spectrum, and processed for mass peak area determination. Each sample point shown in Fig. 3-8 was obtained from 60 replicates of co-added spectrum. The estimated time constants from the experimentally obtained curves were 1,600 and 180 μs for MCP 1 and MCP 2, respectively. The estimated relative gains at t_0, the time of $^{129}Xe^+$ ion detection, were approximately 0.47 and 0.56. Extrapolating the fit-curves, the estimated time points where the gain was assumed to be zero were 990 and 150 μs ahead of the t_0 values for MCP 1 and MCP 2, respectively. The peak intensity of $^{129}Xe^+$ was approximately 350 mV for both MCP 1 and MCP 2 experiments, and the obtained peak areas were corresponding to 95 and 58 pC for the MCP 1 and MCP 2 experimental runs, respectively. The number of $^{129}Xe^+$ ions that irradiated MCP 1 and MCP 2 were estimated to be 93 and 140, respectively, based on the obtained peak areas, the modal peak height of the argon single ion, and the single argon peak width (2 ns) under the given MCP conditions.

The capacitance obtained from the method described in the Experimental section was (6.5 ± 0.7) pF for both MCP detectors. The RC values were computed as 3,250 and 461 μs using the resistance values listed in Table 3-1; thus, the k factors of Equation 2 were 0.48 ± 0.07 and 0.38 ± 0.06 for MCP 1 and MCP 2, respectively. These obtained k factors indicate that the experimentally obtained time constants using an ion pair with various Δt values were smaller than those determined using the capacitance and resistance. A discrepancy in the time-constant values between those suggested from RC and those obtained from LED illumination experiments has also been reported [3-9,19]. However, the majority of papers report that the RC-suggested value is more rapid (i.e., $k > 1.0$) than that obtained experimentally using photons.

The MCP gain model has long been discussed as an array of independent channels, and it is known that the gain drops to zero at the time of signal input. However, the ion of the "dependent peak"

(^{132}Xe$^+$) may not hit the same channel as the ion of the proceeding peak (^{129}Xe$^+$) because the estimated number of ions in a peak per ion-push event is between 93 and 140, while the total number of 1-mm-diameter channels is 4,200 in the MCP detector. In other words, approximately 93–140 ^{129}Xe$^+$ ions may hit the detector surface simultaneously, and several microseconds later, 93–140 ^{132}Xe$^+$ ions will hit the detector surface simultaneously over the area corresponding to 4,200 microchannels. Statistically, the majority of ^{132}Xe$^+$ ions will not hit precisely the same location hit by the ^{129}Xe$^+$ ions. The relationship between the radial distance and gain depression for the pin-hole spot illumination was intensively studied by Fraser et al [3-6]. They clearly showed that a multistage MCP detector exhibits strong interchannel couplings. In addition, they developed the concept of the "reservoir model." The "reservoir model" has been considered as the evolution of charge in a reservoir of fixed depth. The gain of a given pulse then depends on the magnitudes and temporal spacings of the previous pulses.

  Since the gain remains at 47–56% when the proceeding ^{129}Xe$^+$ hits the detector, the assumption that the gain drops to zero does not seem to be true. Hence, it is more reasonable to conclude that adjacent channels are dependent on one another, and that the effect that one channel produces when it emits electrons also affects other channels. Moreover, the relationship between the channels affects the relaxation time as well.

  Until now, MCP manufacturers are attempting to reduce resistance for MCP products to obtain faster time constants. However, there is an apparent limit for the resistance, which is ~5 MΩ. If the MCP resistance is too low, it may cause meltdown by the generated heat itself, even if the pulse voltage supply is used or a heat-sink-equipped cooling system is employed. If the MCP resistance is 5 MΩ, the time constant will still be approximately 10 μs, which is not sufficiently fast for common practical applications of MALDI TOF mass spectrometry.

3.4 Conclusions

A method was developed to determine the gain-drop rate using an ion as a function of a series of time differences (Δt) between two different groups of ions. This method was established on a multi-turn TOF mass spectrometer, and involves the use of an isotope cluster of xenon ions that flies in a figure-of-eight orbit and the extraction of an ion at a given lap number. The time constants for two chevron MCP detectors with resistances of 500 and 71 MΩ were determined to be 1,600 and 180 µs, respectively, and their capacitance was estimated to be 6.5 pF. The k factors obtained in this chapter (k= 0.38 and 0.48) are quite different from those reported by Fraser et al [3-5,6]. They evaluated the gain recovery time constants from the ratio of the MCP output current to the nominal strip current for continuous X-ray and UV illumination using their analytical model (continuous irradiation method). The discrepancy can be attributed to the differences in the evaluation methods or in the input particles (photons and ions). In Chapter 4, a chevron MCP detector is evaluated by the continuous irradiation method and the double-pulse method.

References

[3-1]   R.C. Beavis, B.T. Chait, RAPID COMMUNICATIONS IN MASS SPECTROMETRY VOL.3 (1989) 233–237.

[3-2]   A. Westman, G. Brinkmalm, D.F. Barofsky, International Journal of Mass Spectrometry and Ion Processes 169–170 (1997) 79–87.

[3-3]   B.J. Sams, Review of Scientific Instruments 62 (1991) 595–599.

[3-4]   D.C. Anacker, J.L. Erskine, Review of Scientific Instruments 62 (1991) 1246–1255.

[3-5]   G.W. Fraser, M.T. Pain, J.E. Lees, J.F. Pearson, Nuclear Instruments and Methods in Physics Research Section A: Accelerators, Spectrometers, Detectors and Associated Equipment 306 (1991) 247–260.

[3-6]   G.W. Fraser, M.T. Pain, J.E. Lees, Nuclear Instruments and Methods in Physics Research Section A: Accelerators, Spectrometers, Detectors and Associated Equipment 327 (1993) 328–336.

[3-7]   A.J. Guest, ACTA ELECTRONICA (1971) 79–97.

[3-8]   E.H. Eberhardt, Appl. Opt. 18 (1979) 1418.

[3-9]   L. Giudicotti, M. Bassan, R. Pasqualotto, A. Sardella, Review of Scientific Instruments 65 (1994) 247–258.

[3-10]   A. Sharma, J.G. Walker, Quantum Opt. 1 (1989) 11–16.

[3-11]   H. Rashidzadeh, B. Guo, Anal. Chem. 70 (1998) 131–135.

[3-12]   D.J. Cho, Dead-Time Effects In Photon Counting, University of Rochester, 1989.

[3-13]   S. Shimma, H. Nagao, J. Aoki, K. Takahashi, S. Miki, M. Toyoda, Anal. Chem. 82 (2010) 8456–8463.

[3-14]   K.R. Jensen, T. Hondo, H. Sumino, M. Toyoda, Anal. Chem. 89 (2017) 7535–7540.

[3-15]   T. Hondo, K.R. Jensen, J. Aoki, M. Toyoda, Eur J Mass Spectrom (Chichester) 23 (2017) 385–392.

[3-16]   H. Kobayashi, T. Hondo, N. Imaoka, M. Suyama, M. Toyoda, Nuclear Instruments and Methods in Physics Research Section A: Accelerators, Spectrometers, Detectors and Associated Equipment 971 (2020) 164110.

[3-17]   W. Gao, Z. Li, N. Sammes, An Introduction to Electronic Materials for Engineers. 2nd Ed, World Scientific, 2011.

[3-18]   T. Hondo, H. Kobayashi, M. Toyoda, Mass Spectrometry 9 (2020) A0088–A0088.

[3-19]   G.W. Fraser, J.F. Pearson, Nuclear Instruments and Methods in Physics Research 219 (1984) 199–212.

4. Evaluation of gain-recovery time by ultraviolet irradiation

4.1 Introduction

The gain-recovery time constants obtained in the previous chapter were considerably smaller than those reported by Fraser et al [4-1,2]. Fraser et al. experimentally evaluated the time constant from the ratio of the MCP output current to the nominal conduction (strip) current for continuous X-ray and ultraviolet (UV) illumination using their analytical model (continuous irradiation method), where the time constant was proportional to the production of R and C but not equal to the RC constant [4-1,2]. They expressed the recharge time constant as

$$\tau = kRC \tag{4-1}$$

where k represents the properties of an unknown channel recharge circuit. The k factors of the MCP detectors with the plate electrical resistance in the range of 27–2,450 MΩ were evaluated for different illumination areas. The reported k factors were 2.5 to 27,500, and the k factors for the multi-stage detectors were a function of the illumination area. Close agreement between the X-ray and UV data has also been reported. Anacker et al. derived the recharge time constant as follows:

$$\tau = \frac{OAR}{1-OAR}\frac{1}{\pi}RC \equiv k'RC \tag{4-2}$$

assuming that currents are confined to the agglomerated semiconducting lead surface of the channel, where OAR is the open area ratio of the MCP [4-3]. By substituting 0.6 for OAR, typical for most MCPs, the k' factor is found as 0.47 from Eq. (4-2).

Instead of continuous irradiation method, the recovery time of an MCP was obtained via the irradiation of double pulses [4-4,5]. In these methods, the MCP detector is irradiated by the first pulse and multiplies the electrons. If the detector is irradiated with a second pulse with a time interval shorter than the MCP recovery time after the irradiation of the first pulse, the output signals for the second

pulse decrease (gain drop). The recovery time can be obtained by monitoring the dependence of the output signals on the second pulse while changing the time interval. Giudicotti et al. [4-4] evaluated the recovery time of an MCP photoelectron multiplier tube (manufactured by ITT Electro Optical Products Division), composed of an S-20 photocathode and a 3-stage MCP, using double pulses generated by a light-emitting diode (LED) ($\lambda = 670$ nm). The experimental recovery time is a few times longer than the theoretically determined value of the RC constant. Coeck et al. [4-5] investigated the 'saturation effect, ' which occurs when high-intensity ion bunches impinge on the MCP detector and can alter the structure and intensity of the MCP signal. They determined the gain-recovery time of a chevron MCP detector using ion double pulses and compared it with the expected RC constant. Using Eq. (4-1), the k factor is determined as two. Also in Chapter 3, the gain recovery was evaluated using double-ion pulses on a TOF mass spectrometer. The k factors of two MCP detectors with the R values of 500 and 71 MΩ were obtained as 0.48 and 0.38, respectively. As mentioned above, the reported k factors were not consistent and obtained under various evaluation methods and conditions, such as the MCP gain, types of incident particles, number of input particles, and illumination area. In particular, the k factors ($k = 2.5$ to 27,500) obtained by continuous UV illumination were considerably higher than those ($k = 0.38$ to 2) obtained by double-ion pulses. The difference in k factor is attributed to the experimental methods. Fraser et al. observed the spatial extension of the gain drop so that the gain drop occurred not only in the activated channels where the electrons were multiplied, but also in the surrounding channels, and suggested that this phenomenon affects the k factor obtained by the continuous irradiation method [4-2]. However, the k factor of the same MCP detector has not been evaluated using the continuous irradiation method and the double-pulse method. In this chapter, the gain-recovery time constants of a chevron MCP detector by two methods were compared. The k factors obtained by the two methods were quite different, and this difference is discussed.

4.2 Experimental

A schematic of the experimental setup is shown in Fig. 4-1. The chevron MCP detector used in this experiment consisted of two stacked MCPs (F1551-01, Hamamatsu Photonics K.K., Hamamatsu, Japan) with no gaps between them. A P-47 aluminum-coated phosphor screen was placed 1.0 mm behind the rear MCP, which also functioned as an anode for reading the output current of the MCP. Table 4-1 lists the MCP parameters. The RC constant of the detector was calculated as 2.7 ms, using the resistance of the inspection sheet and the capacitance obtained in Chapter 3. The MCP detector was placed in a vacuum chamber with a quartz window and irradiated with UV light through the window. To generate UV light pulses with a width of a few microseconds, a high-power UV LED with a ball lens (250 nm, 1 mW) (LED 250 J, Thorlabs, New Jersey, USA) was used as the irradiation source. A variable pinhole (F70, MISUMI Group Inc., Tokyo, Japan) and two lenses (f = 40 mm, 50 mm-diameter) (ASL5040-UV, Thorlabs, New Jersey, USA) were used, as shown in Fig. 4-1. An aperture (stainless steel) with a diameter of 3 mm was placed 50 μm in front of the MCP detector. The electrons from the MCP were converted into photons by the phosphor screen, and the image on the phosphor screen was acquired using an EM-CCD camera (C9100-13, Hamamatsu Photonics K.K., Hamamatsu, Japan) through a relay lens with × 3 magnification. The electrical signal from the phosphor screen passed through 20-dB attenuators (120082, Test Product International Inc., Beaverton, USA) and a transimpedance amplifier (C12419, Hamamatsu Photonics K.K., Hamamatsu, Japan) and was acquired using an oscilloscope (DSOX6004A, Keysight Technologies, Santa Rosa, USA). While the attenuators prevent amplifier saturation, the amplifier converts the signal from current to voltage. A delay pulse generator (DG 645, Stanford Research Systems, Sunnyvale, USA) controlled the timing of the UV LED emission and data acquisition on the oscilloscope. The UV LED was driven by a power amplifier (T-HVA03, Turtle Industry Co., Ltd., Tsuchiura, Japan) to obtain sufficiently high photon fluxes to cause the MCP gain drop.

Table 4-1. Parameters of the chevron MCP used in the experiment. The capacitance value was referred in Chapter 3

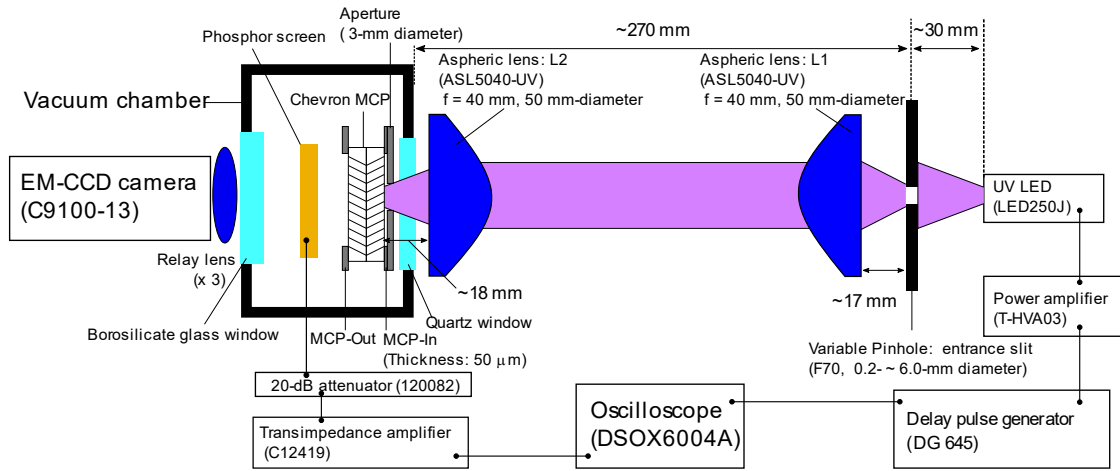| Name	MCP parts-number	serial number	bias angle	channel diameter	effective diameter	plate thickness	resistance	capacitance
Front	F1551-01	A056131	8°	12 μm	14.5 mm	0.48 mm	207 MΩ	13 pF
Rear		A056134					214 MΩ	

Fig. 4-1. Schematic of the experimental setup. The optical system of the apparatus employs the pseudo monochromatic light source (UV LED, 250 nm, 12 nm bandwidth), an entrance slit (variable pinhole, 0.2- ~ 6.0-mm inner diameter), two 50 mm-diameter aspheric lenses (L1 and L2) placed in the opposite direction as symmetric layout and the terminal plane (MCP). The radiating view half angle of the light source is 7.5°, which limits to 2.9° by the entrance slit; thus, the optics utilizes a narrow energy distribution range of 90% and higher for zero-order light. The light from the entrance slit turns to parallel by L1, then converges parallel light by L2, forming an entrance slit image on the MCP. The electrons from MCP were converted into photons by the phosphor screen coated with aluminum, and the image was acquired by an EM-CCD camera. The electrical signal was acquired by an oscilloscope through the phosphor screen. The delay pulse generator controlled the timings of UV irradiation and data acquisition.

4.3 Results and Discussion

4.3.1 Evaluation of gain recovery time by the double-pulse method

Fraser et al. reported that the k factors of the chevron MCP for X-rays and UV were 2.5 to 27,500 [4-1,2]. For example, the k factors were 34 and 95 in the illumination area of 0.79 mm^2 (1-mm diameter) and 14.5 mm^2 (4.3-mm diameter), respectively. However, the k factors reported by Coeck et al. and in Chapter 3 using ion double pulses were inconsistent with those reported by Fraser et al. The k factors reported by Coeck et al. [4-5] were two in the illumination area of 4-mm diameter and those described in Chapter 3 were 0.38 and 0.48 in the illumination area of 1-mm diameter. There is a large discrepancy between the k factors obtained with the continuous irradiation method and those obtained using the double-pulse method. It was considered that the discrepancy was caused by the evaluation method or type of incident particles. To specify the cause, the k factor was evaluated using the double-pulse method with a UV LED.

In this experiment, two identical pulses with a width of 2 μs were generated by the UV LED in time interval Δt, which is the time between the turn-off time of the first pulse and the start time of the second pulse. The repetition frequency was set to 10 Hz, which provided sufficient time to fully recover the MCP gain in one period. The voltages between MCP-In and MCP-Out (MCP voltage) and between MCP-Out and the phosphor screen were set to 2,000 and 500 V, respectively.

Figure 4-2 shows a waveform acquired by averaging 100 waveforms at Δt =10 μs and an illumination area 3 mm in diameter. The ratio of the output charge of the second pulse to that of the first pulse was defined as the relative gain $G'(\Delta t)$. The relative gain at Δt =10 μs was 47%. The relationship between the relative gain and Δt is shown in Fig. 4-3. The relative gain was gradually recovered as Δt was increased. The relative gain can be fitted by:

$$G'(\Delta t) = 1 - A_1 \exp\left(-\Delta t/kRC\right) \tag{4-3}$$

where $1 - A_1$ is the relative gain at $\Delta t = 0$. The same evaluation was performed for illumination

areas 2 and 1 mm in diameter. The spatial uniformity of the output electrons from the MCP was verified, as shown in Fig. S4-3 in Section 4.5.2 of the supplemental information. The fitted curves of 3-, 2-, and 1-mm diameter were $1 - 0.51 \exp\left(-\frac{\Delta t}{0.68 RC}\right)$, $1 - 0.43 \exp\left(-\frac{\Delta t}{0.64 RC}\right)$, and $1 - 0.40 \exp\left(-\frac{\Delta t}{0.62 RC}\right)$, respectively, where the RC constant was 2.7 ms. The k factors were 0.68 ± 0.1, 0.64 ± 0.2, and 0.62 ± 0.2, where C is 6.5 ± 0.7 pF. The k factors obtained with UV irradiation were in agreement with those obtained in Chapter 3 using xenon ions ($k = 0.48 \pm 0.07$) at an irradiation diameter of 1 mm. The k factor did not depend on the type of particles (photons and ions). The k factors obtained by this study were significantly smaller than those reported by Fraser et al. (2.5 to 27,500) [4-1,2]. Then, the differences between the k factors obtained in his study and those reported by Fraser et al. were considered because of the differences in the evaluation methods. Fraser et al. evaluated the k factors from the ratio of the output current to the strip current for continuous X-ray or UV illumination but did not measure the number using the double-pulse method. Then, it is necessary to evaluate the k factor using the same MCP detector as both the continuous irradiation method and the double-pulse method.

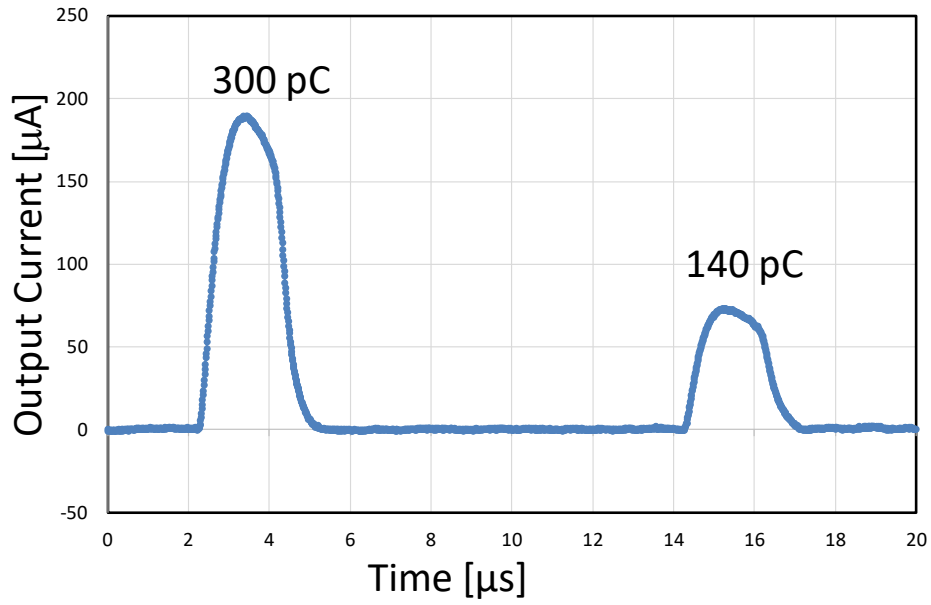Fig. 4-2. MCP response for double pulses at $\Delta t = 10$ μs and the illumination area of 3-mm diameter.
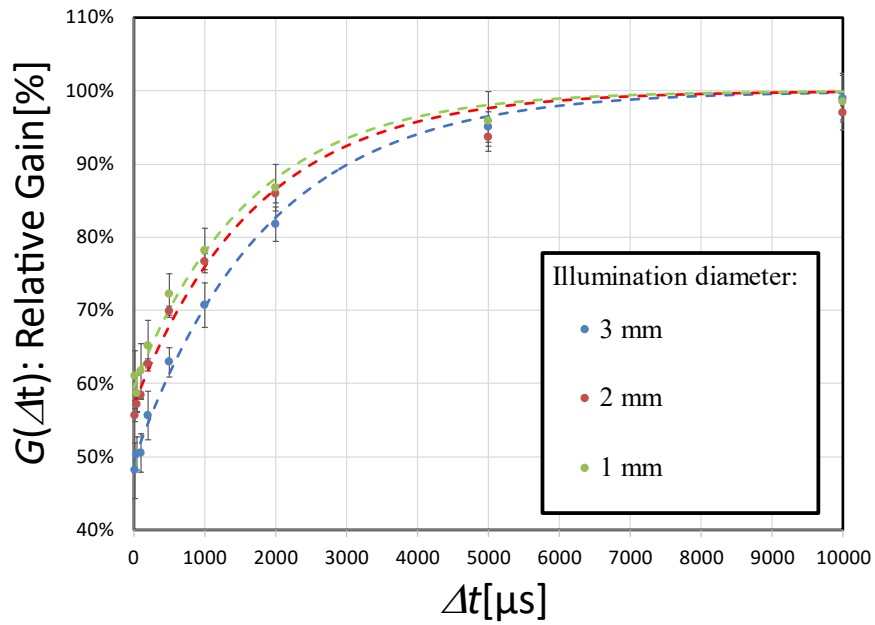

Fig. 4-3. MCP gain-recovery plots using the double pulse. Five measurements were performed at each point, and the average (dot) and standard deviation (error bar) are shown. At $\Delta t = 10$ μs, the relative gain values were decreased to 61%, 56%, and 48% at 3, 2, and 1 mm-diameter, respectively.

50

4.3.2 Evaluation of gain-recovery time by the continuous irradiation method

As discussed in the previous subsection, the k factor is expected to depend on the evaluation method. The k factor for the same MCP detector should be evaluated using the continuous irradiation method. Fraser et al. derived the relationship between the ratio of the output current to the strip current per channel (I_p/I_s) and input count rate per channel (N), expressed as:

$$\frac{I_p}{I_s} = \frac{G_0 M R}{V(\frac{1}{N}+kRC)} \tag{4-4}$$

where G_0, M, and V are the output charge per particle when the time interval between incidents is sufficiently long, total number of channels, and MCP voltage, respectively. Fraser *et al.* experimentally obtained the ratio (I_p/I_s) and N, and then calculated the k factor using Eq. (4-4). Using this method, the k factor was evaluated using the same experimental setup as for the double-pulse method with the LED operated in continuous mode. The relationship between I_p/I_s and N was determined by changing the light intensity of UV LED. The details of obtaining I_p, I_s, and N are described in Section 4.5.3 of the supplemental information.

Figure 4-4 shows the relationship between I_p/I_s and N when the illumination area was changed to 3, 2, and 1 mm in diameter, where G_0, M, and V are 1.1 pC, 8.8 $\times$ 10^5, and 2,000 V, respectively. These results are good agreement with those reported by Fraser et al. [4-1]. The output current per channel I_p was also larger than the strip current per channel I_s at high count rates, which was attributed to the increase in the strip current. According to Guest et al. [4-6], the effective resistance of the MCP decreases because the cascade of electrons forms a parallel resistive path. The strip current flowing to an activated channel was expected to be considerably larger than I_s at a high count rate, thus enabling the activated channels to output a current larger than I_s. In this experiment, the strip current to all channels $M I_s$ was increased from 4.7 to 6.1 µA when N was increased up to 3,700 CPS/ch at an illumination diameter of 3 mm. By fitting the relationship using Eq. (4-4), the k factors at illumination diameters of 3, 2, and 1 mm were derived as 17, 11, and 6.6, respectively. The k factors

were quite different from those obtained using the double-pulse method.

The reason behind the considerable difference between the k factors obtained by the double-pulse method and continuous irradiation method was investigated. The models and assumptions used to derive Eq. (4-4) were considered, where the distribution of the time interval t between successive events is assumed as the Poissonian (random) source and is expressed as follows:

$$I(t) = N \exp{(-Nt)} \tag{4-5}$$

Assumably, the output charge for a single particle $G(t)$ is zero immediately after a particle reaches one channel and recovers to level G_0 with the time constant $kRC, i.e.,$

$$G(t) = G_0(1 - \exp{(-t/kRC)}) \tag{4-6}$$

The average output charge for a single particle at N can be obtained by

$$\overline{G(N)} = \frac{\int_0^\infty G(t)I(t)\,dt}{\int_0^\infty I(t)dt} = \frac{G_0}{(1+NkRC)} \tag{4-7}$$

Equation (4-7) assumes that only the gain of the channel that is hit by a particle is decreased, thus the gains of the neighbor channels are not affected. In addition, Fraser et al. reported that the spatial extension of the gain drop was a factor in determining the maximum sustain rate (k factor) of a chevron MCP detector. Equation (4-5) was modified to assume that electron multiplications for one particle decrease the gains of multiple channels in consideration of the spatial extension of the gain drop. If the gains of the surrounding a channel are affected, the input count rate of the particles decreasing the gain N' can be expressed as follows:

$$N' = aN \tag{4-8}$$

The distribution of the time intervals t' between successive events that decrease the gain of one channel can be expressed as

$$I'(t') = N' \exp(-N't') \tag{4-5'}$$

By using Eq. (4-5)', Eq. (4-7) can be modified as follows:

$$\overline{G(N')} = \frac{\int_0^\infty G(t')I\prime(t\prime)\,dt\prime}{\int_0^\infty I\prime(t\prime)dt\prime} = \frac{G_0}{(1+aNkRC)} \qquad (4\text{-}7)\text{'}$$

The output current per channel I_p and strip current per channel I_s can be calculated as follows:

$$I_p = \overline{G(N')}N = \frac{G_0}{(1+aNkRC)}N \qquad (4\text{-}9)$$

$$I_s = \frac{V}{MR} \qquad (4\text{-}10)$$

Therefore, Eq. (4-4) can be rewritten as Eq. (4-4)', assuming that the electron multiplications for one particle decrease the gains of the surrounding channel a.

$$\frac{I_p}{I_s} = \frac{G_0 MRN}{V(1+aNkRC)} = \frac{G_0 MR}{V(\frac{1}{N}+akRC)} \qquad (4\text{-}4)\text{'}$$

The relationship between I_p/I_s and N shown in Fig. 4-4, was reconsidered according to Eq. (4-4)'.

Here, the value (k = 0.6) obtained using the double-pulse method was adopted as the k factor in Eq. (4-4)'.

The dashed lines in Fig. 4-5 represent Eq. (4-4)' when the value of a is changed to 1, 10, 20, and 50, where G_0, M and V are 1.1 pC, 8.8×10^5, and 2,000 V, respectively. The dots in Fig. 4-5 are the same as those in the experimental results in Fig. 4-4. As shown in Fig. 4-5, the ratio I_p/I_s became saturated even for small N as the value of a was increased. When a = 20, the experimental results closely matched the trend suggested by Eq. (4-4)'. This suggests that the gain drop extends to the second neighboring channel of the activated channels.
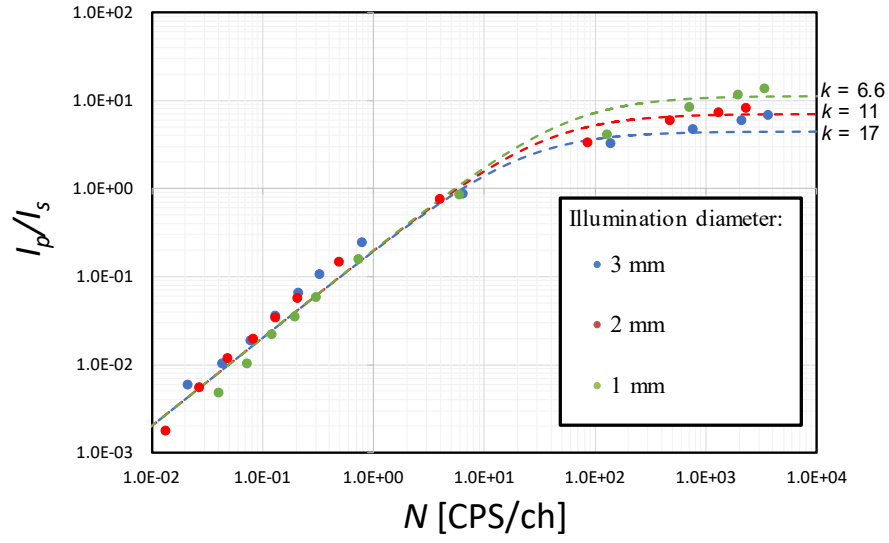
Fig. 4-4. Relationship between the ratio of the output current to the strip current per channel I_p/I_s and input count rate per channel N, where G_0, M, and V are 1.1 pC, 8.8 $\times$ 10^5, and 2,000 V. Dashed color curves were obtained by fitting the experimental results with Eq. (4-4), where the k factors were 17, 11, and 6.6 at 3-, 2-, and 1-mm diameters, respectively.
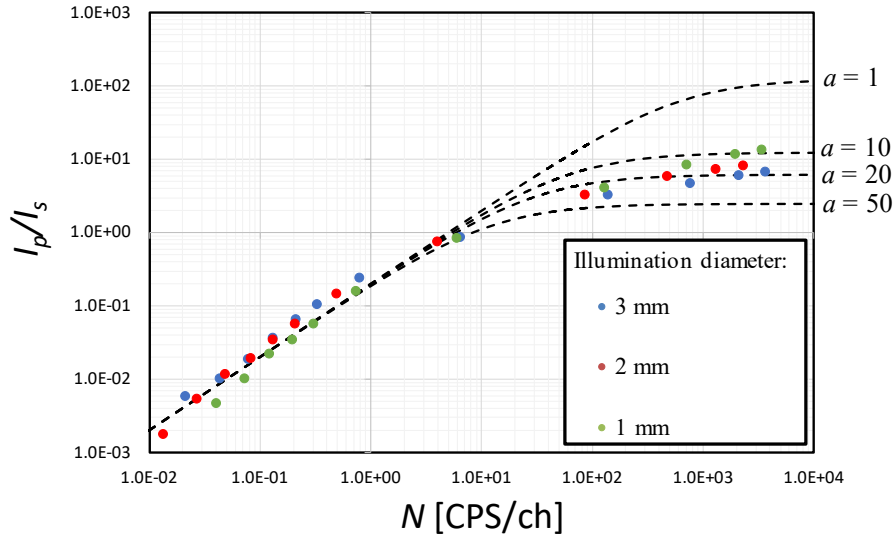

Fig. 4-5. Relationships between $\frac{I_p}{I_s}$ and N obtained by the experiment and Eq. (4-4)'. The dots are the same as the experimental results in Fig. 4-4. The dashed lines show Eq. (4-4)' when the value of a is changed to 1, 10, 20, and 50, where G_0, M, k, and V are 1.1 pC, 8.8 $\times$ 10^5, 0.6, and 2,000 V, respectively.

The spatial spread of the 'gain drop' was also observed in an experiment using the double-pulse method. As shown in Fig. 4-2, the relative gain decreased to 47% at an illumination area of 3-mm diameter, corresponding to 38,000 channels when 300 pC was the output for the first pulse. The number of photoelectrons generated per pulse was estimated as 270 from the average output charge of 1.1 pC for a single photoelectron at the MCP voltage of 2,000 V (information about the detector gain is shown in Figs. S4-1 and S4-2.). The number of photoelectrons was approximately two orders of magnitude smaller than the number of channels, suggesting that the gain drop for a single photoelectron extended to the channels surrounding the activated channel. In Chapter 3, similar results were observed for the detection of ions. The gain was reduced to 47% when 140 ions were entered into a 1-mm diameter corresponding to 4,200 channels.

The continuous irradiation method does not account for the spatial extension of the gain drop, which can cause an overestimation of the k factor. Since k factors were obtained from 0.38 to 2.0 using the double-pulse method, including the previous study [4-5], it was concluded that the gain-recovery time constant of the MCP was comparable to the RC constant. The k factors ($k = 0.38$ to 0.68) obtained in this study somewhat differed from those obtained by Coeck et al. ($k = 2.0$). In this evaluation, R and C are the electrical resistance and capacitance of the effective area with channels, respectively, and were measured in vacuum. In contrast, Coeck et al. used the resistance and capacitance of assembled MCP detectors (MCP-MA25, Del Mar photonics, Inc., San Diego, USA) as R and C, respectively. Seemingly, C includes the capacitances of the gap between the electrodes and the MCP's rim part that does not have channels. In addition, it is not mentioned whether the measurements of R and C were performed under vacuum. Generally, the resistance of the MCP in the atmosphere is over one order of magnitude lower than that in vacuum. The k factor was overestimated when a small RC constant was used to calculate the k factor. In contrast, Anacker et al. derived the k factor as described in Eq. (4-2), assuming that current flows only to the surface of the MCP channel [4-3]. In their model, the

definitions of R and C are the same as those in this study. Substituting the OAR value (0.6) of the MCP used in the experiment, the k factor was 0.47, which is consistent with the results obtained in this study. This assumption seems more reasonable than the assumption that the MCP is an isotropic medium as the mechanism of electrical conduction in the MCP has been considered to be electron hopping between Pb islands on the channel surface [4-7,8]. The gain-recovery time constant appears smaller than the RC constant of the effective area under a vacuum.

The range in which the gain drops may extend to an area larger than that of the electron multiplication channel. This causes distortion of the image and degradation of quantification. Previously, the gain drop for continuous high UV photon fluxes was evaluated [4-2,9]. Edgar et al. reported that gain depression occurs up to 1.5 mm from the center of the activated region. However, it is difficult to explain the spatial extent of the gain drop by a single photoelectron or ion from their report because these results are the sum of the spatial gain drop extents for multiple photoelectrons. In this investigation, the k factor obtained using the continuous irradiation method increased as the illumination area increased, as shown in Fig. 4-4. The spatial extension of the gain drop appears to depend on the illumination area because the k factor obtained by the double-pulse method was almost independent of the illumination area. Further studies are necessary to evaluate the spatial extent of the gain drop for a single photoelectron.

4.4 Conclusion

The gain drop of the chevron MCP detector was investigated using a UV LED with the double-pulse method and the continuous irradiation method. The gain-recovery time constant of the chevron MCP detector was evaluated by the double-pulse method as 0.62 ± 0.2 to 0.68 ± 0.1 times of the RC constant in the illumination area of 1 to 3 mm in diameter. The k factors obtained were in good agreement with those obtained by xenon ion irradiation in Chapter 3, implying that the gain-recovery

time is independent of the type of incident particles. However, the gain-recovery time constants obtained using the continuous irradiation method were overestimated by over one order of magnitude. This overestimation was attributed to the fact that the model formula used in the continuous irradiation method does not consider the spatial extension of the gain drop. The k factor obtained by the continuous irradiation method was consistent with that obtained by the double-pulse method if electron multiplications for one photoelectron affect the gains of neighboring channels. Based on the assumption that one photoelectron decreases the gains to zero, the number of affected channels was 20. However, if the gains are not decreased to zero, the number of channels should be larger than 20. Conclusively, the MCP gain-recovery time constant was comparable to the RC constant according to the results obtained using the double-pulse method, including past results. As shown in this chapter and ion irradiation in Chapter 3, a gain drop was observed in a considerably smaller number of incident particles (photoelectrons or ions) than in the irradiated channels. This suggests that the gain drop occurs in not only activated channels, but also the neighboring channels. The spatial extent of the gain drop for a single pulse should be evaluated to determine the number of channels affected by the multiplication processes for one particle. Gatii et al. and Anacker et al. [4-3,10] suggested that the electric field produced by the wall charges caused the spatial extension of gain drop. Assuming this mechanism, the spatial extent of the gain drop is estimated in Chapter 5. Also in Chapter 6, the spatial extent of gain drop for a single pulse irradiation is experimentally evaluated.

4.5 Appendix: Supplemental information

4.5.1 Response of the chevron MCP to a single UV photon

The time response and pulse height distribution (PHD) for a single photoelectron were evaluated by continuous UV irradiation at below 0.01 count per second per channel (CPS/ch) to avoid the influence of the MCP gain drop. The voltages between MCP-In and MCP-Out (MCP voltage) and between MCP-Out and the phosphor screen were set to 2,000 and 500 V, respectively. Figure S4-1 (a) shows the output waveform for a single photoelectron acquired by the oscilloscope using self-triggering at an average of 1,000 times. The pulse height was 67 mV, and the amount of output charge was calculated as 1.1 pC, corresponding to the gain of 6.9×10^6. Figure S4-1 (b) shows the PHD of single photoelectron. The average pulse height was 68 mV, which was consistent with that shown in Fig. S4-1 (a). Then, the gain of the detector for MCP voltages from 1,200 to 2,000 V was evaluated. The output current was measured using an electrometer (model 8240, ADCMT, Hiki, Japan) at an MCP voltage from 1,200 to 2,000 V. Gain values were calculated from the values of the output current and gain of 2,000 V. Figure S4-2 shows the gain of the detector for the MCP voltage.

(a) Averaged output waveform
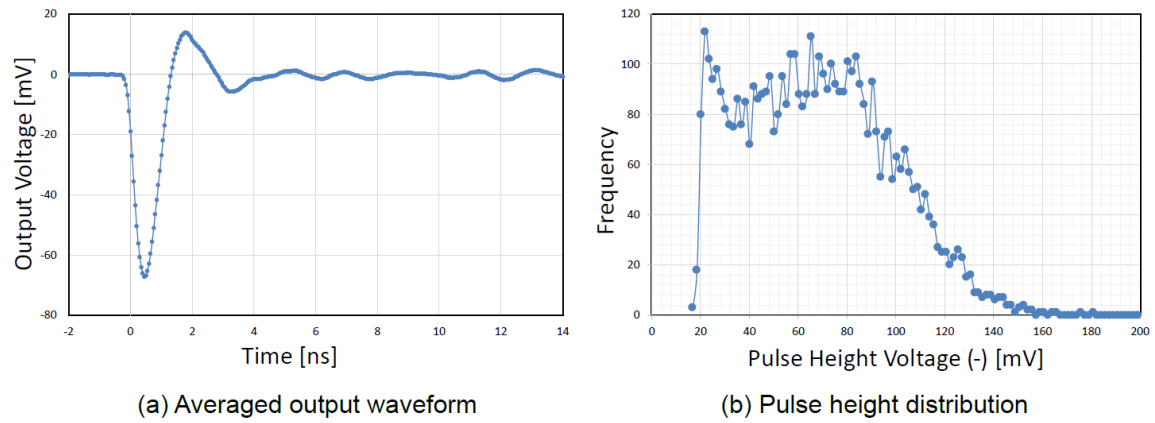
(b) Pulse height distribution

Fig. S4-1. Response to a single photoelectron at an MCP voltage of 2,000 V. (a) shows the output waveform by averaging 1,000 shots. (b) shows the PHD for 5,000 shots.
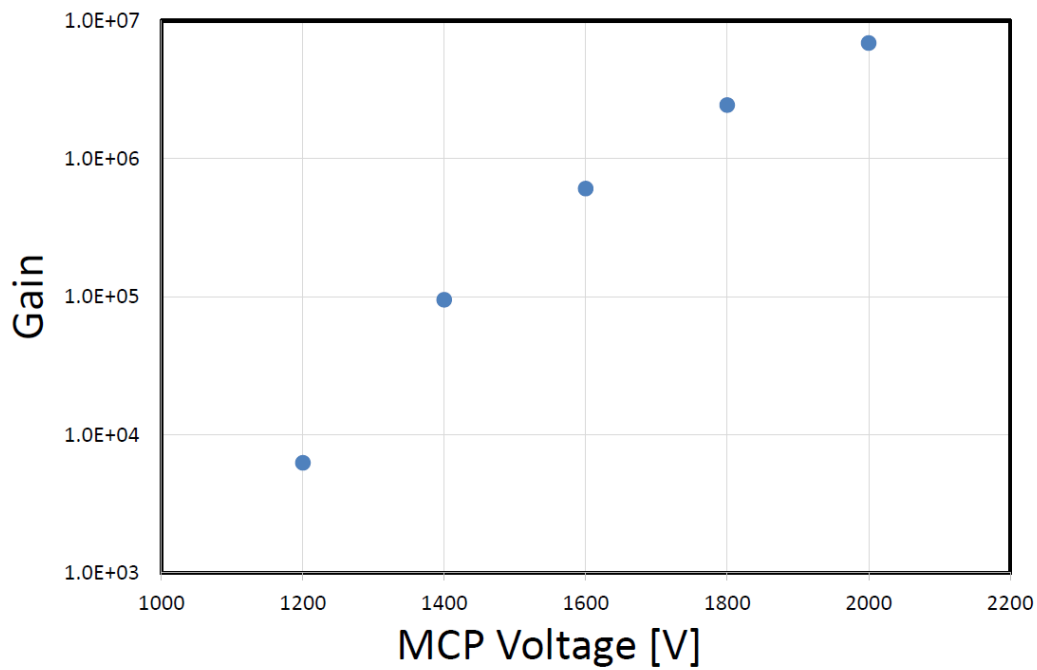

Fig. S4-2. Gain characteristic of the detector as a function of the MCP voltage. The gains were 6.9×10^6, 2.5×10^6, 6.1×10^5, 9.1×10^4, and 6.3×10^3 at the MCP voltage of 2,000, 1,800, 1,600, 1,400, 1,200 V, respectively, corresponding to the amount of the output charge of 1.1, 0.39, 0.097, 0.015, and 0.0010 pC, respectively.

4.5.2 Uniformity of MCP output

The spatial distribution of electrons from the MCP detector was evaluated. The MCP voltage and the acceleration voltage were set to 1,200 and 4,000 V so that the phosphor could convert the electrons to photons, and the image on the phosphor screen was acquired by an EM CCD camera. The illumination area was adjusted with an aperture of 1 or 2 mm diameter in front of the LED. Figure S4-3 shows the electron images acquired by the camera at 5 second exposure. As a result of adjusting the optical system so that the spatial distribution became as uniform as possible, the output variations on the horizontal axis were 33, 26 and 17 % at 3, 2 and 1 diameter, respectively, at peak to peak.

(a) 3 mm   (b) 2 mm   (c) 1 mm

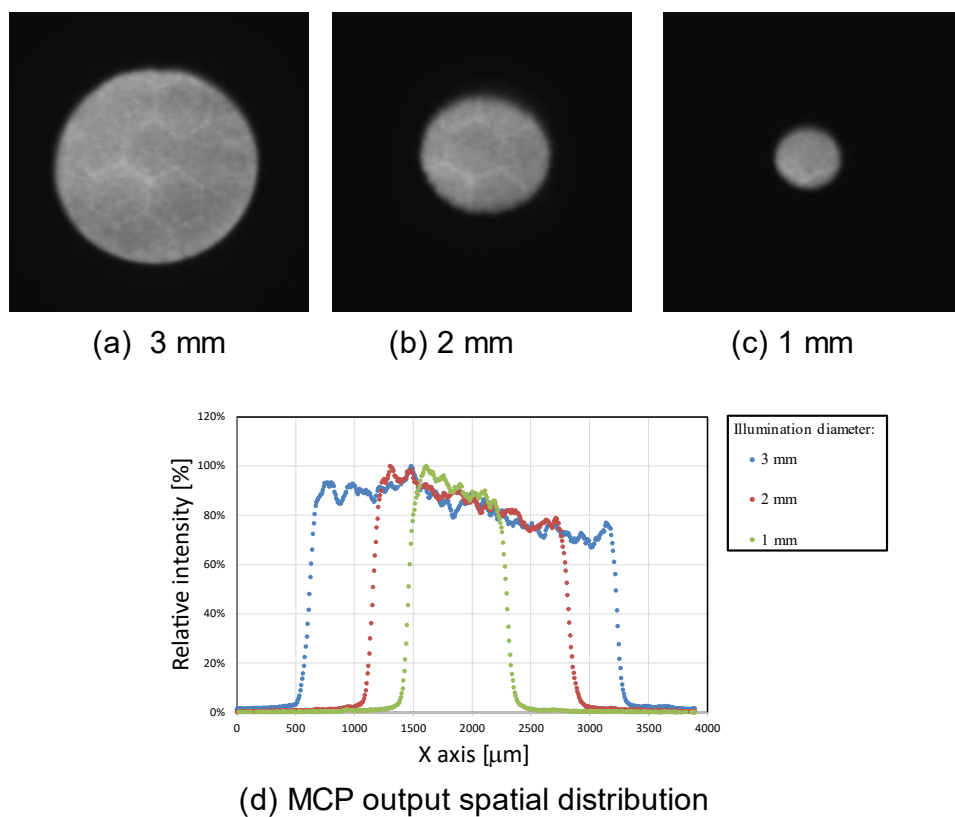(d) MCP output spatial distribution

Fig. S4-3. MCP output spatial distribution acquired by the EM-CCD camera.

(a) electron image at 3-mm diameter. (b) electron image at 2-mm diameter.

(c) electron image at 1-mm diameter. (d) MCP output spatial distribution on the horizontal axis.

4.5.3 Method to obtain current ratio I_p/I_s and count rate per channel N

In the continuous irradiation method, the k factor is evaluated from the output current per channel I_p, strip current per channel I_s and count rate per channel N using Eq. (4-4). In this section, the method used to obtain I_p, I_s, and N is explained. The currents I_p, I_s can be expressed using the following equations:

$$I_p = I_{out}/ N_i \qquad\qquad\qquad (S4\text{-}1)$$

$$I_s = I_{strip}/ M \qquad\qquad\qquad (S4\text{-}2)$$

where I_{out}, I_{strip}, M, and N_i are the output current from the MCP, the total strip current flowing through all channels, the number of all channels ($M = 8.8 \times 10^5$), and the number of channels in the illumination area, respectively. The output current I_{out} was measured from the phosphor screen using an electrometer. The strip current I_{strip} was measured from the conduction current between MCP-In and MCP-Out. The number of channels N_i is 38,000, 17,000, and 4,200 at illumination areas of 3, 2, and 1 mm in diameter, respectively.

The input count rate per channel N was estimated from the UV photon flux density from the LED. The photon flux density was measured as the current I_{UV} (photocurrent) using a photodiode (S2281, Hamamatsu photonics K.K., Hamamatsu, Japan). N can be expressed by

$$N = N_{out}/ N_i \qquad\qquad\qquad (S4\text{-}3)$$

where N_{out} is the output count rate. The count rate N_{out} was measured using an oscilloscope. The relationship between N and I_{UV} is plotted in Fig. S4-4 at the illumination areas 3-, 2-, and 1-mm diameter. The plots were fitted using the following equation:

$$N = c\, I_{UV} \qquad\qquad\qquad (S4\text{-}4)$$

where c is the proportionality coefficient. The values of c were 3.5×10^7, 3.0×10^7, and 3.3×10^7 at an illumination area of 3-, 2-, and 1-mm diameter, respectively. A linear relationship between N and I_{UV} was derived at $N < 0.5$. In this experiment, the value of N was obtained

from the measured I_{UV} using Eq. (S4-4). If there are sufficiently high photon fluxes causing the gain-drop input into the MCP detector, the amplitude of the output pulse is decreased below a threshold level for counting, making the obtained output count rate N_{out} nonlinear to the actual input count rate N.
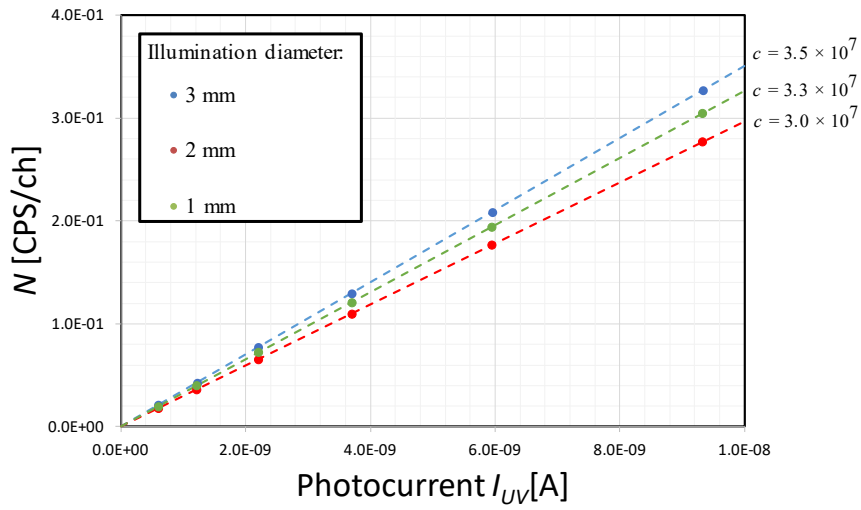

Fig. S4-4. Relationship between input count rate per channel N and measured photocurrent by photodiode I_{UV}.

References

[4-1]   G.W. Fraser, M.T. Pain, J.E. Lees, J.F. Pearson, Nuclear Instruments and Methods in Physics Research Section A: Accelerators, Spectrometers, Detectors and Associated Equipment 306 (1991) 247–260.

[4-2]   G.W. Fraser, M.T. Pain, J.E. Lees, Nuclear Instruments and Methods in Physics Research Section A: Accelerators, Spectrometers, Detectors and Associated Equipment 327 (1993) 328–336.

[4-3]   D.C. Anacker, J.L. Erskine, Review of Scientific Instruments 62 (1991) 1246–1255.

[4-4]   L. Giudicotti, M. Bassan, R. Pasqualotto, A. Sardella, Review of Scientific Instruments 65 (1994) 247–258.

[4-5]   S. Coeck, M. Beck, B. Delauré, V.V. Golovko, M. Herbane, A. Lindroth, S. Kopecky, V.Yu. Kozlov, I.S. Kraev, T. Phalet, N. Severijns, Nuclear Instruments and Methods in Physics

Research Section A: Accelerators, Spectrometers, Detectors and Associated Equipment 557 (2006) 516–522.

[4-6] A.J. Guest, ACTA ELECTRONICA 14 (1971) 79.

[4-7] H. Cai, Y. Sun, X. Zhang, L. Zhang, H. Liu, Q. Li, T. Bo, D. Zhou, C. Wang, J. Lian, Materials 12 (2019) 1183.

[4-8] Y. Huang, P. Shi, Y. Zhou, Y. Wang, Y. Fu, J. Wang, J. Jia, Int J Appl Glass Sci 11 (2020) 285–293.

[4-9] M.L. Edgar, J.S. Lapington, A. Smith, Review of Scientific Instruments 63 (1992) 816–819.

[4-10] E. Gatti, K. Oba, P. Rehak, IEEE Transactions on Nuclear Science NS-30 (1983) 461–468.

5. Estimating the spatial extent of gain drop

5.1 Introduction

In this chapter, the spatial extent of gain drop is estimated, assuming that the electric field produced by the wall charges causes the spatial extension of gain drop. In the several previous studies, the mechanism of the spatial extent of the gain drop was proposed. Pearson et al. [5-1] proposed that charges in inactive channels are transferred to activate ones through lateral capacitances, which reduces the gains of the former. Eberhartz et al. [5-2] provided a detailed discussion of lateral capacitance between channels. Although Fraser et al. [5-3] tested the hypothesis of lateral capacitance, they could not confirm its presence. Anacker et al. observed a decrease in the output of the chevron MCP within 500 ns of detecting photoelectrons, which was attributed to gain drops in the surrounding channels [5-4]. Although Anacker et al. calculated the charge transfer time through the lateral capacitances as using the RC circuit model as $\tau \gg 9\,\text{ms}$, lateral capacitance was not the main mechanism of the spatial extension since τ was too long for the 500 ns timescale. On the other hand, Gatti et al. [5-5] suggested that the electric field generated by wall charges in activated channels extends into the surrounding channels and affects their gains. They calculated the wall-charge potential in activated channels based on Gauss' law and found that a wall charge of 0.1 pC placed 0.2 mm from the output end of the MCP increased the potential of the second neighbor channels by 6 V.

Anacker et al. [5-4] estimated the spatial extent of the gain drop from the magnitude of the transverse electric field $E_T(x)$ produced by uniform line charges on the rear MCP of a chevron MCP detector. The transverse electric field was computed assuming the wall charge as an infinite uniform along the channel axis, as shown in Fig. 5-1 (a). Further, the channel bias angle (i.e., the angle between the channel axis and the normal to the MCP front surface) in their calculation was taken to be zero.

64

$$E_T(x) = \frac{(\varepsilon_r + 1)}{\varepsilon_r x} \rho \qquad\qquad (5\text{-}1)$$

where ε_r, ρ, and x are the relative permittivity of the lead glass, line-charge density, and radial distance from the line charge, respectively. Charge density ρ is given by

$$\rho = \frac{Q}{l_s} \qquad\qquad (5\text{-}2)$$

where Q and l_s are the wall charges corresponding to MCP output charges and the length of the wall charges, respectively. They defined the threshold electric field (E_{lim}) at which the gain drop first occurs, as follows:

$$E_{lim} = \frac{eE_o}{D} \qquad\qquad (5\text{-}3)$$

where e, E_0, and D are the elementary charge, initial average radial energy of the secondary electron, and channel diameter, respectively. E_{lim} prevents secondary electrons from hitting the opposite wall, thus affecting the gains in the region where $E_T(x) \geq E_{lim}$. Therefore, the radius of the gain-drop spatial extent (r_d) is expressed as:

$$r_d = \frac{(\varepsilon_r + 1)}{\varepsilon_r} \frac{Q}{E_{lim} l_s} \qquad\qquad (5\text{-}4)$$

In this model, the gain drop was extended proportionally to the MCP output charge, and the spatial extents of the gain drop were estimated as 106 and 190 μm for output charges of 0.43 and 0.83 pC, respectively. Although Edgar et al. [5-6] and Fraser et al. [5-7] evaluated spatial extent when continuously illuminated by UV photons at a high count rate, their results were not described by Eq. (5-4). Therefore, it is necessary to discover a more suitable model that can better explain gain drop spatial extension.

In this chapter, the electric field was calculated, assuming that the wall charges increase exponentially along the channel axis toward the electron exit. Subsequently, its effect on the chain-reaction of electron emission was investigated. Finally, the spatial extent of the gain drop was estimated using the calculated electric field.

5.2 Electric field generated by wall charges

Assuming that the wall charges in the rear MCP (Model F1551-01, Hamamatsu Photonics K.K., Hamamatsu, Japan) of the chevron detector increase exponentially along the channel axis, its electric field can be calculated. The channel diameter, pitch, and bias angle for this model are 12 μm, 15 μm and 8 ° respectively. Figure 5-1(b) shows a schematic of the coordinates used to calculate the electric field generated by wall charges. The coordinates of the input and output ends of the rear MCP, along which the wall charges were distributed, were taken as $z = 0$ and 480 μm, respectively. The channel bias angle was assumed to be zero and the MCP was treated as a uniform dielectric. Assuming the MCP to be a discrete dynode with n dynodes [5-2,8] its gain G can be described as:

$$G = \delta^n \qquad (5\text{-}5)$$

where δ is the gain per collision. The number of dynodes corresponds to the number of collisions, and is taken as 20 [5-2,9]. Assuming that the wall charges increase with the number of electrons, its distribution in the rear MCP can be expressed as follows:

$$q(z) = eN\delta^{\frac{n}{L}z}, \qquad (5\text{-}6)$$

where z, e, N, and L are the spatial coordinates along the channel axis (longitudinal direction), elementary charge, number of wall charges at $z = 0$, and MCP thickness ($L = 480$ μm), respectively. The total gain of chevron detector was 1.9×10^6, with a reduction in the gain of the rear MCP due to the space-charge effect [5-10] (The information of the detector's gain is shown in Fig. S6-1 in Section 6.5.1.) Assuming the gain of the rear MCP to be 10% of that of the front MCP, δ^n was obtained to be 440, which yields a δ value of 1.36. The wall charges were placed with a 1 μm pitch along the z-axis, from $z = 0$ to 480 μm. The total wall charge Q is calculated as follows:

$$Q = \sum_{z=0}^{z=480\mu m} q(z) \qquad (z = 0, 1, 2 \cdots 480 \text{ μm}) \qquad (5\text{-}7)$$

The total wall charge Q was defined as 1.0 pC corresponding to the typical chevron-detector gain of

6.3×10^6 and the resultant N was derived to be 170. Figure 5-2 depicts the wall-charge distribution for this case. Half of all the wall charges were distributed in the region of $z > 430$ μm. The transverse and longitudinal electric fields $E_T(x, z)$ and $E_L(x, z)$ as shown in Fig. 5-1 (b) produced by the wall charges were calculated using the following equations:

$$E_T(x,z) = \sum_{b=0}^{b=480\mu m} \left(\frac{q(b)}{4\pi\varepsilon_0\varepsilon_r(x^2+(z-b)^2)} \frac{x}{\sqrt{x^2+(z-b)^2}} \right) \quad (b = 0, 1, 2 \cdots 480\,\mu m) \quad (5\text{-}8)$$

$$E_L(x,z) = \sum_{b=0}^{b=480\mu m} \left(\frac{q(b)}{4\pi\varepsilon_0\varepsilon_r(x^2+(z-b)^2)} \frac{(z-b)}{\sqrt{x^2+(z-b)^2}} \right) \quad (b = 0, 1, 2 \cdots 480\,\mu m) \quad (5\text{-}9)$$

where b, ε_0, and ε_r denote the position along the z-axis, dielectric constant, and relative permittivity of the MCP. ε_r was taken as 4.5 since that is the average relative permittivity of vacuum and lead glass (7.8 to 8.3) [5-3,10]. Mathematica Online Version 13.2 (Wolfram Research, Inc., Champaign, IL, USA) was used to calculate the electric fields.

The electric field generated in the rear MCP was calculated for Q = 1.0 pC. Figure 5-3 illustrates the Coulomb force acting on an electron, with each force vector displayed at every 15 μm (corresponding to the channel pitch) along the x direction. In each channel, the transverse Coulomb force increased along the channel axis and peaked at z = 450 μm. Beyond this point (i.e., at z > 450 μm), the longitudinal Coulomb force acted in the opposite direction to the electrostatic force produced by the voltage application. However, the longitudinal electric field was not expected to have a significant impact on the spatial extension of the gain drop since the longitudinal Coulomb force was relatively weaker than the transverse Coulomb force as the distance x increased, as shown in Fig. 5-3.
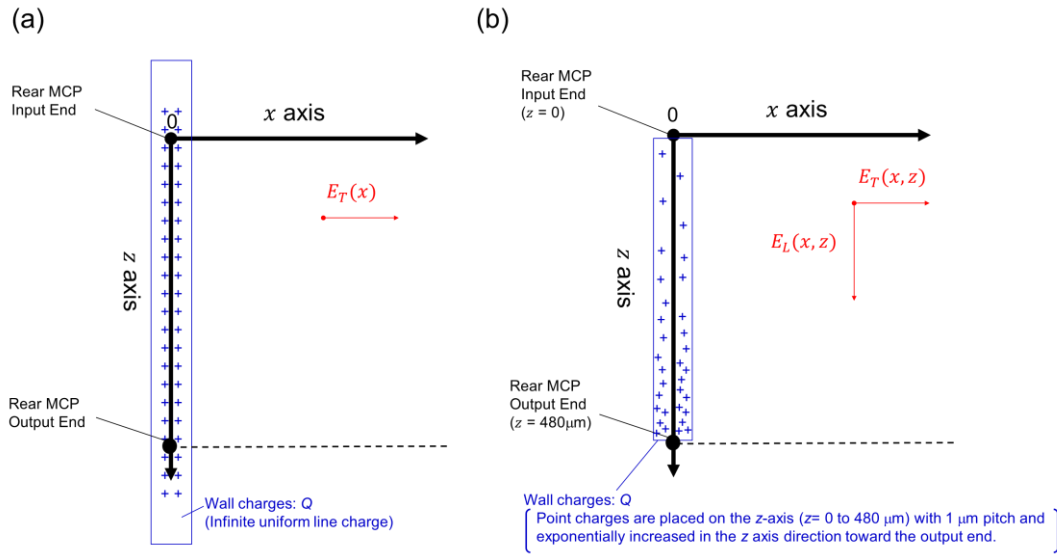
Fig. 5-1. Coordination diagram to calculate the electric field generated by the wall charges in the rear MCP. (a) Infinite, uniform line charge. (b) Finite, exponential line charge increasing along the channel axis; detailed distribution shown in Fig. 5-2.
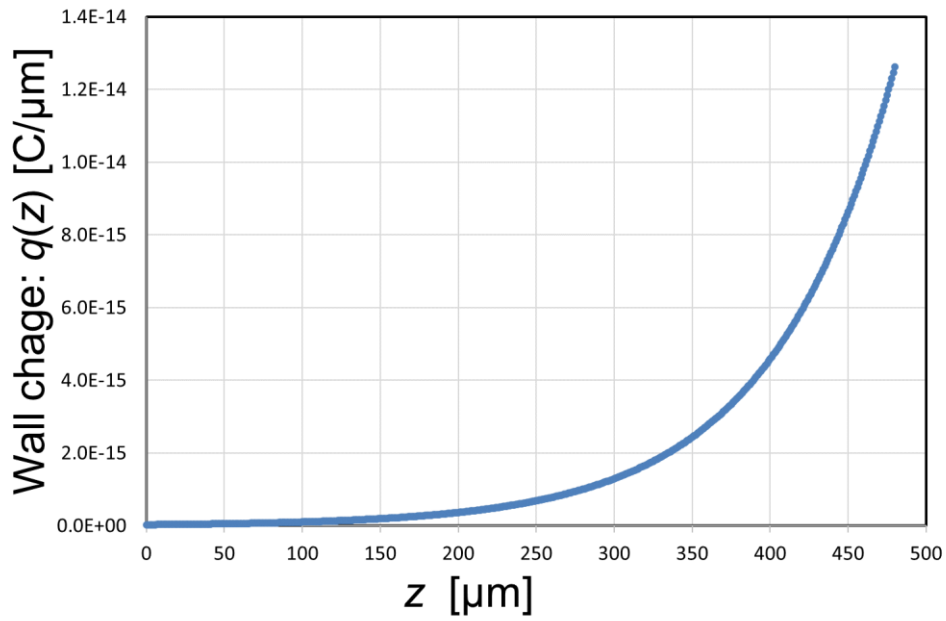

Fig. 5-2. Distribution of wall charge (q) along the channel axis (z) at a total charge Q =1.0 pC.
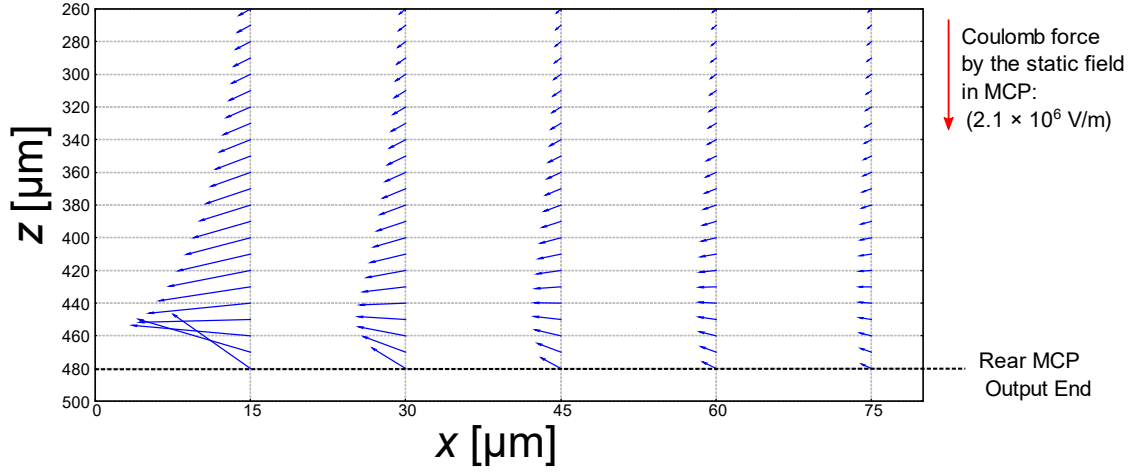
Fig. 5-3. Estimated Coulomb force in the rear MCP at $Q = 1.0$ pC. Each vector is displayed every 15 µm in the x direction (channel pitch) and every 10 µm in the z direction. The red arrow at the right top indicates the Coulomb force acting on an electron at the application of 1,000V.

5.3 Effect of the transverse field on the electron trajectory

The transverse electric field was expected to alter the collision energy of the secondary electron when it collides with the channel wall, flight distance between the collisions, and number of collisions of secondary electrons within the MCP, thereby reducing its gain. To better understand this effect, calculations were performed to determine the collision energy and flight distance, both in the presence and absence of the transverse electric field. Figure 5-4 illustrates the coordinate system used in these calculations. The initial velocity v_0 of the secondary electrons is expressed as:

$$v_0 = \sqrt{{v_{x0}}^2 + {v_{y0}}^2 + {v_{z0}}^2} \qquad (5\text{-}10)$$

where v_{x0}, v_{y0}, and v_{z0} are the initial velocities along the x, y and z directions, respectively. Therefore, the initial energy E_0 is:

$$E_0 = \frac{m}{2e}{v_0}^2 \qquad (5\text{-}11)$$

where m is the electron mass (9.1×10^{-31} kg). The direction of electron emission was expressed in the polar coordinate system, where each Cartesian velocity can be expressed as:

$$v_{x0} = v_0 \sin(\theta - \theta_B) \sin\varphi \qquad (5\text{-}12)$$

$$v_{y0} = v_0 \cos(\theta - \theta_B) \qquad (5\text{-}13)$$

$$v_{z0} = v_0 \sin(\theta - \theta_B) \cos\varphi \qquad (5\text{-}14)$$

where θ, φ, and θ_B are the polar angle (θ = 0 to 90 °), azimuth angle (φ = 0 to 360 °), and MCP bias angle (θ_B = 8 °), respectively. Assuming that the transverse electric field generated by the wall charges is electrostatic, the Cartesian coordinates of the location of the secondary electrons at any time are:

$$x(t) = -\frac{e}{2m} E_T t^2 \pm v_{x0} t + x_0 \qquad (5\text{-}15)$$

$$y(t) = \pm v_{y0} t + y_0 \qquad (5\text{-}16)$$

$$z(t) = \frac{e}{2m} \frac{V}{L} t^2 + v_{z0} t \qquad (5\text{-}17)$$

where t, E_T, and V are the time, transverse electric field, and voltage applied to the MCP (V = 1,000 V), respectively. Secondary electrons are emitted at $t = 0$, $x = x_0$, $y = y_0$, and $z = 0$. The surface of the channel wall is described by

$$x^2 + (y - (R + z \tan(\theta_B)))^2 = R^2 \qquad (5\text{-}18)$$

where R denotes the channel radius (6 µm). From Eqs. (5-15-18), the time elapsed before the electron collides with the channel wall (t_1) was obtained. By substituting t_1 for t in Eq. (5-17), the flight distance (F) along the z-axis was estimated. Following this, the electron collision energy E_c can be calculated as:

$$E_c = \frac{m}{2e} \left(\left(\frac{dx(t_1)}{dt}\right)^2 + \left(\frac{dy(t_1)}{dt}\right)^2 + \left(\frac{dz(t_1)}{dt}\right)^2 \right) \qquad (5\text{-}19)$$
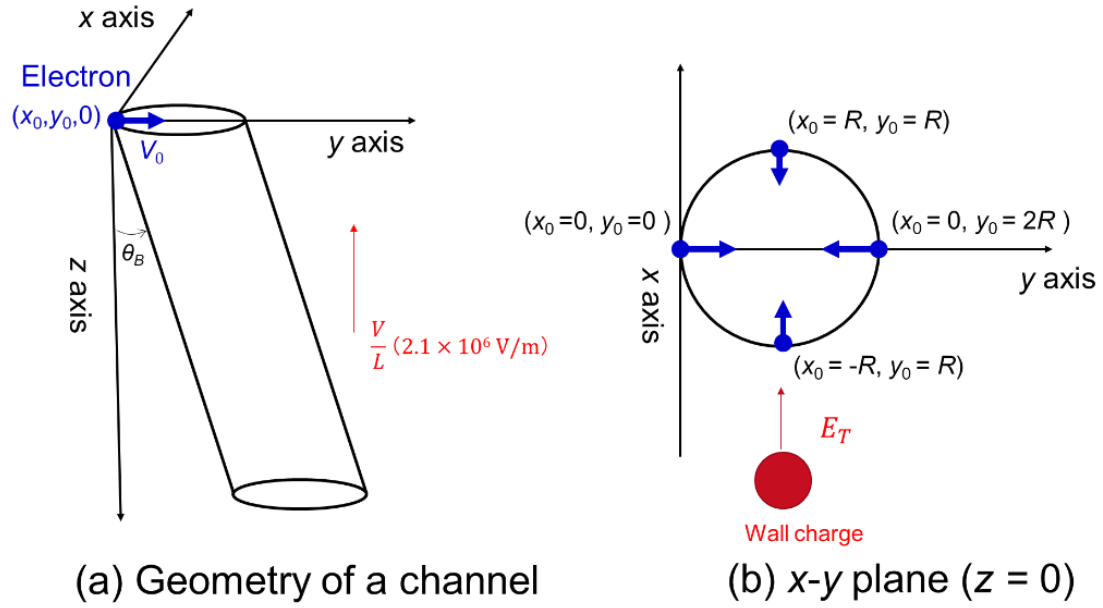
Fig. 5-4. Coordinate system for the estimation of flight distance and collision energy of secondary electron in the rear MCP.
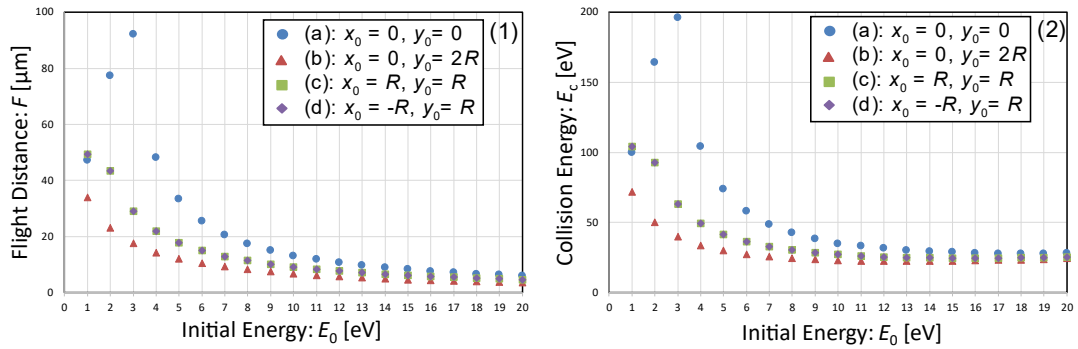

Fig. 5-5. Average flight distance (F) and collision energy (E_c) for each initial energy (E_0) of the secondary electron in the absence of transverse electric field. (1) F against E_0, (2) E_c against E_0.

First, the calculation of F and E_c was performed for initial-energy values (E_0) from 1 to 20 eV at every $2°$ and $5°$ interval of θ and φ, respectively, in the absence of a transverse electric field. Average F and E_c for each E_0 were calculated as shown in Fig. 5-5, assuming electron emission follows a cosine polar distribution and uniform azimuthal distribution [5-11,12]. The distribution of the initial energies of secondary electrons can be expressed by the Maxwell-Boltzmann probability distribution [5-12]:

$$P(E_0) = C \frac{E_0}{E_p} exp\left(-\frac{E_0}{E_p}\right), \qquad\qquad (5\text{-}20)$$

where E_p is the most probable energy of the secondary electron and C is a normalization constant. Considering $E_p = 3$ eV [5-12,13] the average values of F and E_c, thus calculated, are shown in Tables 5-1 and 5-2.

The emissions were calculated at locations $(x_0 = 0, y_0 = 0)$, $(x_0 = 0, y_0 = 2R)$, $(x_0 = R, y_0 = R)$, and $(x_0 = -R, y_0 = R)$, as depicted in Fig. 5-4(b). At locations of $(x_0 = R, y_0 = R)$ and $(x_0 = -R, y_0 = R)$, Eqs. (5-12-14) simplify to:

$$v_{x0} = v_0 cos\theta \qquad\qquad (5\text{-}12)'$$

$$v_{y0} = v_0 sin\theta\ sin\varphi \qquad\qquad (5\text{-}13)'$$

$$v_{z0} = v_0 sin\theta\ cos\varphi \qquad\qquad (5\text{-}14)'$$

As shown in Fig. 5-5, F and E_c at $(x_0 = 0, y_0 = 0)$ were relatively larger than those at other locations. Most of the electrons emitted from this location with $E_0 < 4$ eV cannot collide with the opposite wall ($y > R + z \tan(\theta_B)$) since the channel wall shifts along the y direction. As a result, electrons travel a long distance along the axis and collide with the wall at $y < R + z \tan(\theta_B)$.

Second, F and E_c were similarly calculated while varying E_T from 1.0×10^5 to 4.0×10^5 V/m, with the results portrayed in Figs. 5-6 and 5-7. At emission locations of $(x_0 = 0, y_0 = 0)$ and $(x_0 = R, y_0 = R)$, F and E_c changed sharply at $E_T \geq 2.0 \times 10^5$ V/m. However, at $(x_0 = 0, y_0 = 2R)$, their changes were negligible. Since the channel wall shifted along the y direction, most of the electrons

emitted from $(x_0 = 0, y_0 = 2R)$ immediately collided with the opposite wall regardless of the presence of a transverse electric field.

To understand how variations in E_c impact the gain, both quantities can be related via the following expression [5-11,13] :

$$\delta(E_c) = \delta_{max} \frac{s(\frac{E_c}{E_{max}})}{s - 1 + (\frac{E_c}{E_{max}})^s} \tag{5-21}$$

where δ_{max}, E_{max}, and s are the maximum δ, its corresponding collision energy, and a material-dependent parameter, respectively. In this estimation, impact of the incident angle was neglected. Wu et al. [5-13] reported that the MCP gain calculated using their Monte Carlo simulation model was in good agreement with the experimental data when $\delta_{max} = 4.0$, $E_{max} = 270$ eV, and $s = 1.3$. At $(x_0 = 0, y_0 = 0)$, the average E_c was 91, 82, 72, 63, and 56 eV at E_T of 0, 1.0×10^5, 2.0×10^5, 3.0×10^5 and 4.0×10^5 V/m, respectively, as shown in Table 5-2. From Eq. (5-21), δ was 3.2, 3.1, 2.9, 2.7, and 2.5 at E_c of 91, 82, 72, 63, and 56 eV, respectively. When E_T exceeds 2.0×10^5 V/m, it is expected to result in a gain drop.
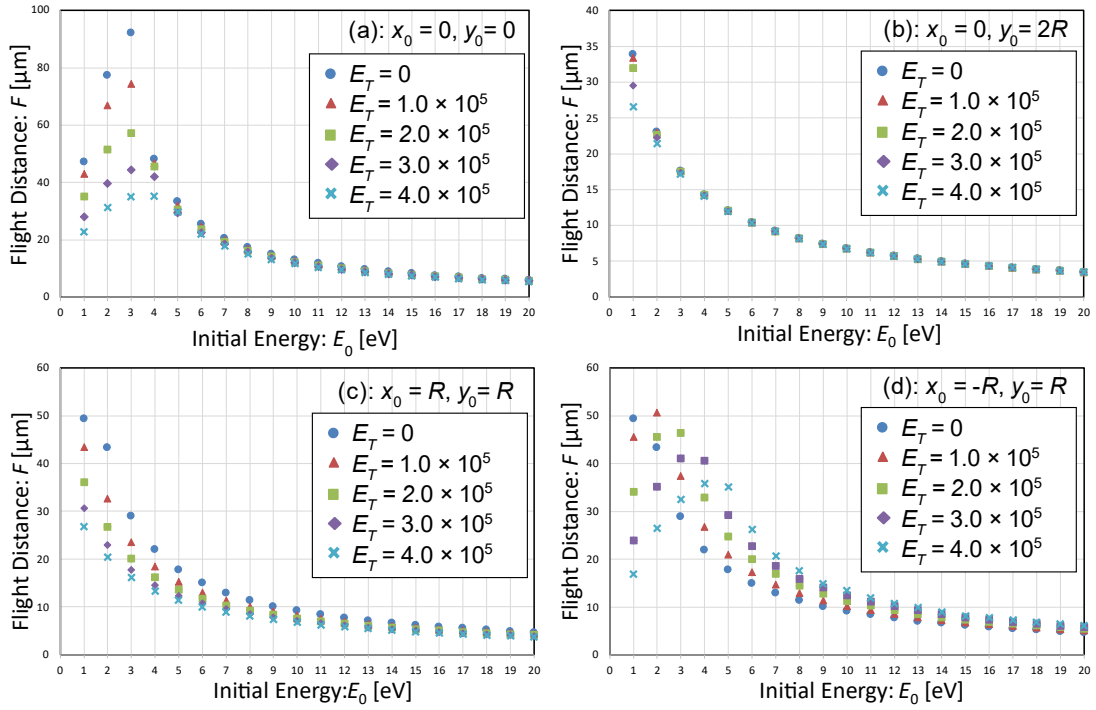
Fig. 5-6. Average flight distance (F) for each initial energy (E_0) of the secondary electron under

five different magnitudes of the transverse electric field (E_T).

Table 5-1. Average flight distance (F) for each transverse electric field (E_T).

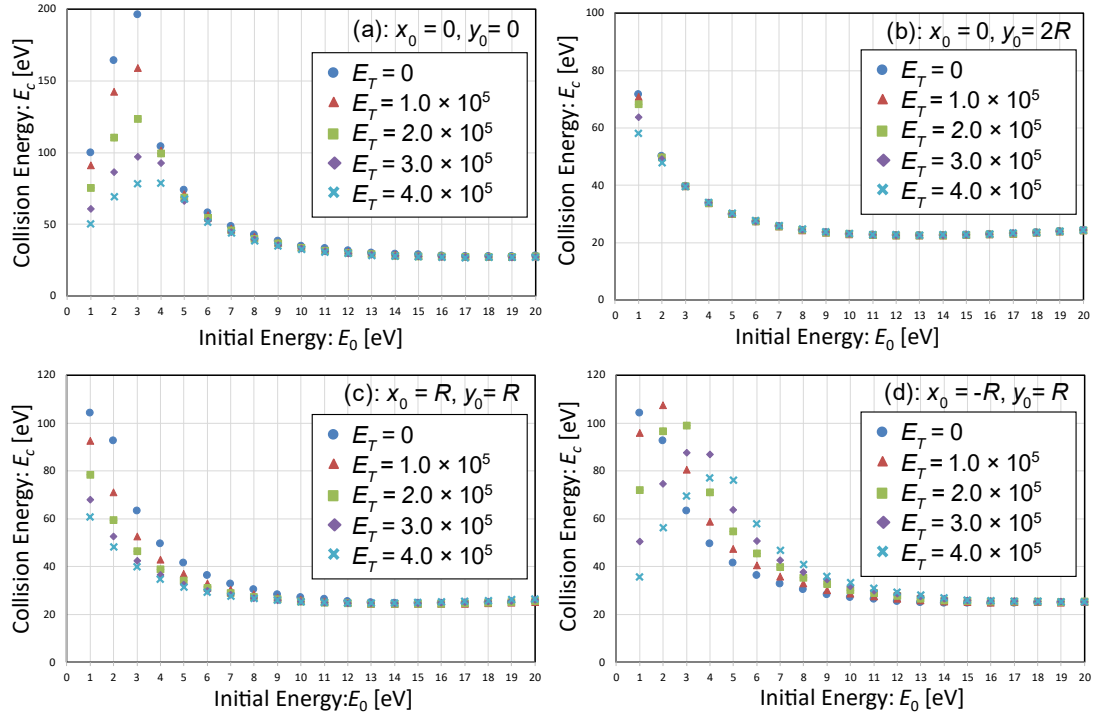|	Emission location			
	(a) $x_0 = 0, y_0 = 0$	(b) $x_0 = 0, y_0 = 2R$	(c) $x_0 = R, y_0 = R$	(d) $x_0 = -R, y_0 = R$
$E_T = 0$ [V/m]	41 μm	14 μm	22 μm	22 μm
$E_T = 1.0 \times 10^5$ [V/m]	37 μm	14 μm	18 μm	25 μm
$E_T = 2.0 \times 10^5$ [V/m]	32 μm	14 μm	16 μm	27 μm
$E_T = 3.0 \times 10^5$ [V/m]	27 μm	14 μm	14 μm	26 μm
$E_T = 4.0 \times 10^5$ [V/m]	24 μm	13 μm	13 μm	24 μm

Fig. 5-7. Average collision energy (E_c) for each initial energy (E_0) of the secondary electron under

five different magnitudes of the transverse electric field (E_T).

Table 5-2. Average collision energy (E_c) for each transverse electric field (E_T).

	Emission location			
	(a) $x_0 = 0, y_0 = 0$	(b) $x_0 = 0, y_0 = 2R$	(c) $x_0 = R, y_0 = R$	(d) $x_0 = -R, y_0 = R$
$E_T = 0$ [V/m]	91 eV	35 eV	51 eV	51 eV
$E_T = 1.0 \times 10^5$ [V/m]	82 eV	35 eV	44 eV	57 eV
$E_T = 2.0 \times 10^5$ [V/m]	72 eV	35 eV	40 eV	60 eV
$E_T = 3.0 \times 10^5$ [V/m]	63 eV	34 eV	37 eV	58 eV
$E_T = 4.0 \times 10^5$ [V/m]	56 eV	34 eV	35 eV	54 eV

5.4 Estimation of the gain-drop spatial extent

Moving forward, the spatial extent of the gain drop using the calculated electric field was estimated. The assumption was that gain drop occurs in the region where $E_T \geq E'_{lim}$. The threshold electric field, E'_{lim} was defined as $2 \times 10^5, 3 \times 10^5$, or 4×10^5 V/m. First, since E_T peaked at $z = \sim 450$ µm, $E_T (x, z = 450$ µm$)$ was calculated at $Q = 0.2, 0.5, 1.0, 2.0, 3.0,$ and 4.0 pC; this is shown in Fig. 5-8. Subsequently, the maximum distances at which the transverse electric field exceeded E'_{lim} were plotted as the spatial extent of the gain drop in Fig. 5-9. The spatial extent gradually increased as Q rose. Anacker et al. expected it to be proportional to Q; however, this is inconsistent with Fig. 5-9.

The model, as described earlier, assumes the wall charge to exponentially increase along the channel axis, with half of them concentrated within 50 µm from the exit. When the radial distance from the activated channel is sufficiently long, the wall charges behave as point charges. However, at shorter distances, they function as line charges. This is supported by calculated results as shown in Fig. 5-9, where spatial extent is confirmed to be proportional to Q at radial distances under 50 µm and to $\sqrt{Q}$ at those exceeding 50 µm. A distance of 50 µm corresponds to the neighboring third channel.
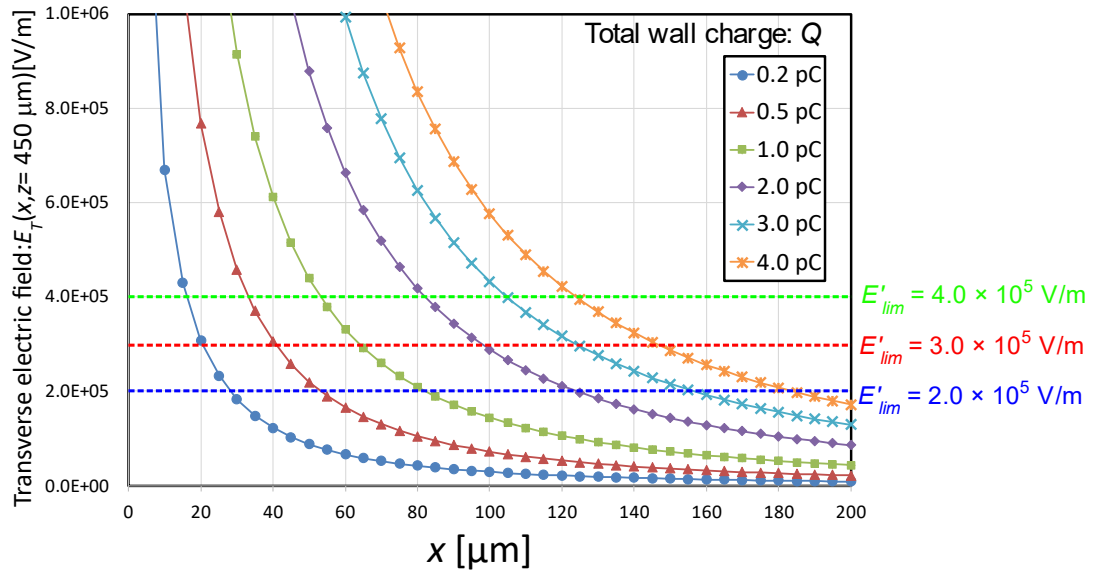
Fig. 5-8. Transverse electric field $E_T(x, z = 450\,\mu m)$ at Q = 0.2, 0.5, 1.0, 2.0, 3.0, and 4.0 pC.
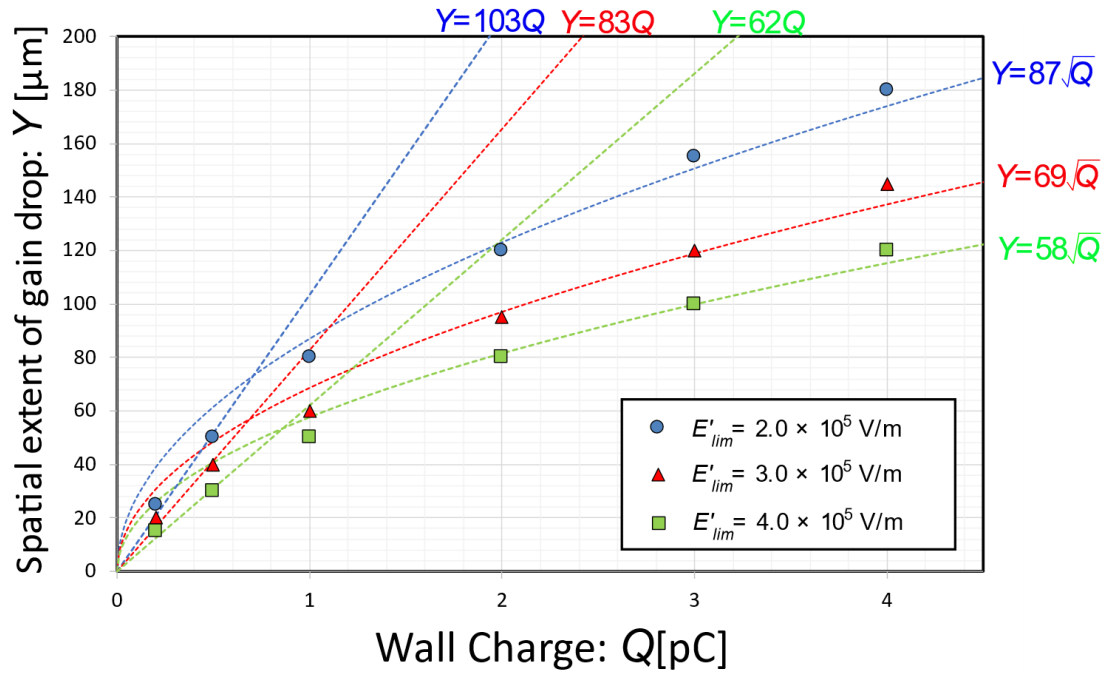

Fig. 5-9. Variation of the spatial extent of gain drop with wall charge.

5.5 Conclusions

In this chapter, an investigation was conducted on the relationship between the gain drop in the rear MCP of a chevron detector and the transverse electric field generated by its wall charge. Previously, the spatial extent of the gain drop was expected to be proportional to the amount of wall charges, assuming that the wall charges were the uniform line charges. However, the wall charges are expected to increase exponentially along the channel axis toward the exit of the channel. The previous model may not have correctly estimated the spatial extent of the gain drop. Considering the distribution of wall charges, the electric field was calculated, and its effect on the gain was investigated by calculating the electron trajectory in the channel. The collision energy of the electrons began to change significantly at a transverse electric field of approximately 2×10^5 V/m, suggesting that this was the threshold for the initiation of the gain drop. The spatial extent of the gain drop estimated from the transverse electric field was proportional to the square root of the wall charge when the distance exceeded 50 μm corresponding to the neighboring third channel. Although the calculations provide insight into the relationship between the gain-drop spatial extent and wall charge, experimental investigation is needed to confirm these findings. In Chapter 6, the spatial extent of the gain drop is experimentally investigated and compared with the estimates.

References

[5-1]   J.F. Pearson, J.E. Lees, G.W. Fraser, IEEE Transactions on Nuclear Science Vol.35 (1988) 520–523.

[5-2]   E.H. Eberhardt, IEEE Transactions on Nuclear Science NS-28 (1981) 712–717.

[5-3]   G.W. Fraser, M.T. Pain, J.E. Lees, J.F. Pearson, Nuclear Instruments and Methods in Physics Research Section A: Accelerators, Spectrometers, Detectors and Associated Equipment 306 (1991) 247–260.

[5-4] D.C. Anacker, J.L. Erskine, Review of Scientific Instruments 62 (1991) 1246–1255.

[5-5] E. Gatti, K. Oba, P. Rehak, IEEE Transactions on Nuclear Science NS-30 (1983) 461–468.

[5-6] M.L. Edgar, J.S. Lapington, A. Smith, Review of Scientific Instruments 63 (1992) 816–819.

[5-7] G.W. Fraser, M.T. Pain, J.E. Lees, Nuclear Instruments and Methods in Physics Research Section A: Accelerators, Spectrometers, Detectors and Associated Equipment 327 (1993) 328–336.

[5-8] E.H. Eberhardt, Appl. Opt. 18 (1979) 1418.

[5-9] L. Giudicotti, M. Bassan, R. Pasqualotto, A. Sardella, Review of Scientific Instruments 65 (1994) 247–258.

[5-10] J.L. Wiza, Nuclear Instruments and Methods 162 (1979) 587–601.

[5-11] M. Furman, M. Pivi, Phys. Rev. ST Accel. Beams 5 (2002) 124404.

[5-12] Q. Wang, Z. Yuan, Z. Cao, B. Deng, T. Chen, K. Deng, Rev. Sci. Instrum. 87 (2016) 073303.

[5-13] M. Wu, C.A. Kruschwitz, D.V. Morgan, J. Morgan, Review of Scientific Instruments 79 (2008) 073104.

6. Evaluation of the spatial extent of gain drop

6.1 Introduction

In Chapter 4, the continuous irradiation method was hypothesized to overestimate the k factor, because the analytical model of the continuous irradiation method does not consider the spatial extension of the gain drop. This phenomenon of gain drop extends from the activated channels, where electrons are multiplied, to the surrounding channels. Assuming that the electron multiplications for a single photoelectron decrease the gains of 20 channels to zero, the analytical model of the continuous irradiation method can express the trend of the experimental results at $k =$ 0.6, where the average output charge for a single photoelectron is 1.1 pC.

In this chapter, the gain-drop spatial extent of a chevron MCP detector is evaluated when specific channels were activated, by placing a phosphor screen behind the MCP. The phosphor screen converted the electron output from the MCP to photons and projected an image reflecting the MCP spatial gain distribution. The MCP detector was irradiated with two UV light pulses. A pulsed laser light was used for the first pulse because the laser light could be focused on the determined channels, and the first pulse irradiated the MCP detector, which multiplied the electrons. If the second pulse irradiates the detector within a time interval shorter than the MCP gain recovery time, the output due to the second pulse decreases (gain drop). Thus, the spatial gain-drop extension caused by the first pulse irradiation could be observed by irradiating the surrounding area with a second pulse. The experiment was conducted over a much shorter time interval (150 μs) than the RC constant (2.7 ms). Because the wall charges cannot be replenished during this time interval, the amount of output charge from the MCP after the first pulse irradiation must correspond to that of the wall charge in the channels. The relationship between the spatial gain-drop extent and amount of output charge for the

first pulse irradiation was investigated. The mechanism of the gain-drop spatial extension was discussed based on the experimental results. Comparing the experimental result with the estimates in Chapter 5, the mechanism of the spatial extension of gain drop is discussed.

6.2 Experimental

6.2.1   MCP detector

A schematic of the experimental setup is shown in Fig. 6-1. A chevron MCP detector composed of two MCPs (F1551-01, Hamamatsu Photonics K.K., Hamamatsu, Japan) with no separating gap was placed in a vacuum chamber. Table 6-1 lists the MCP parameters used in this experiment. The *RC* constant was calculated from the resistance and capacitance to be 2.7 ms. The channel diameter and the distance between two adjacent channel centers were 12 and 15 μm, respectively. An MCP-In electrode (stainless steel) with an aperture diameter of 3 mm was placed 50 μm in front of the detector. A p47 aluminum-coated phosphor screen, placed 500 μm behind the output surface of the second MCP, converted the electrons to photons. The image on the phosphor screen was acquired using an EM-CCD camera (C9100-13, Hamamatsu Photonics K.K., Hamamatsu, Japan) through a relay lens with $\times 3$ magnification. A capacitor of 150 pF was connected to the second MCP output surface to detect the electrical signal using an oscilloscope (DSOX6004A, Keysight Technologies, Santa Rosa, CA, USA). The response to a single photoelectron is shown in Fig. S6-1.
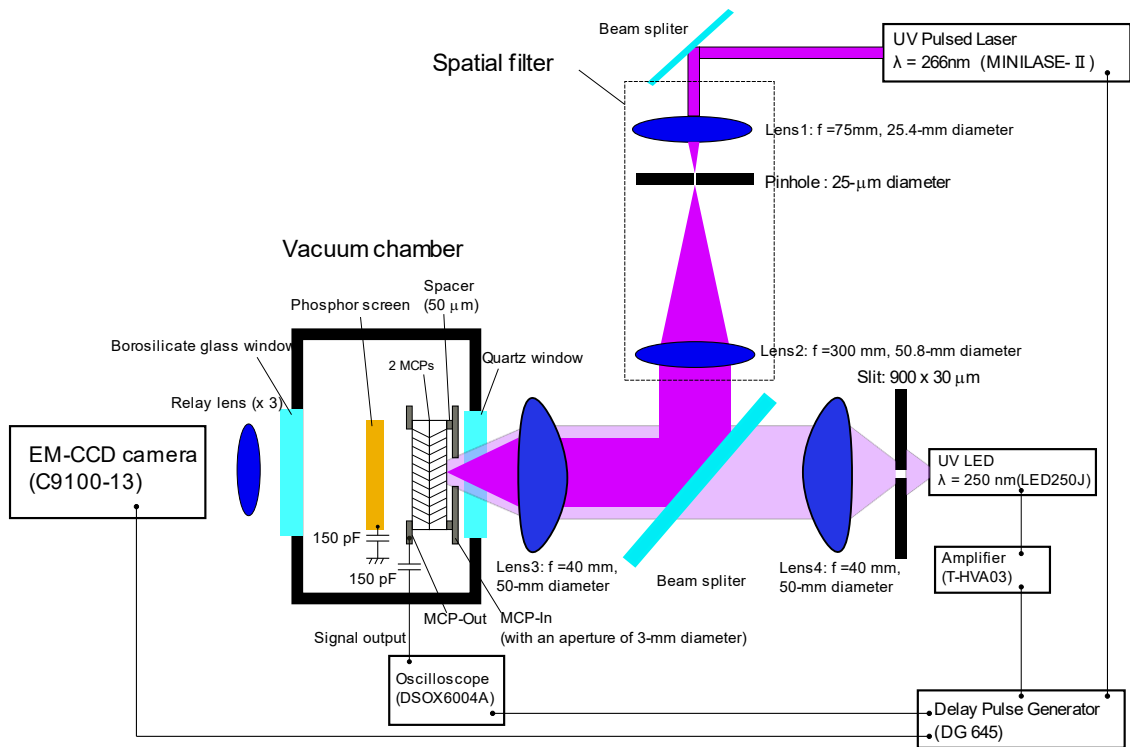
Fig. 6-1. Schematic of the experimental setup. The laser beam was expanded by the spatial filter comprising Lens 1, Lens 2, and a 25-μm pinhole and focused on the detector by Lens 3. The LED irradiated a 900×30 μm area using a slit, Lens 3, and Lens 4. The electrons from the MCP were converted to photons by the phosphor screen, and the image was acquired by an EM-CCD camera. The electrical signal from the MCP was read out by an oscilloscope through a capacitor of 150 pF. The delay pulse generator controlled the timings of the laser emission, LED emission, waveform acquisition with the oscilloscope, and image acquisition with the camera.

Table 6-1. Parameters of the chevron MCP used in the experiment. The capacitance value was referred in Chapter 3.

Name	MCP parts-number	serial number	bias angle	channel diameter	effective diameter	plate thickness	resistance	capacitance
Front		A054973					211 MΩ	
	F1551-01		8°	12 μm	14.5 mm	0.48 mm		13 pF
Rear		A054974					211 MΩ	

6.2.2   Method for evaluating spatial extent of gain drop

A 10 ns pulsed UV laser (λ = 266 nm) (Minilase-II, New Wave Research, Inc., Fremont, CA,

USA) and a high-power UV light-emitting diode (LED) with a ball lens (λ = 250 nm) (LED 250J,

Thorlabs, New Jersey, USA) were used as light sources. The laser light was focused on a 40 μm-

diameter spot on the MCP to create photoelectrons in one channel and the six neighboring channels.

A spatial filter comprising Lens 1 (f = 75 mm, 25.4 mm diameter) (LA4725-UV, Thorlabs, New

Jersey, USA), Lens 2 (f = 300 mm, 50.8 mm diameter) (LA4855-UV, Thorlabs, New Jersey, USA),

and 25 μm pinhole (P25k, Thorlabs, New Jersey, US) was used as illustrated in Fig. 6-1. The laser

beam was focused on the detector using Lens 3 (f = 40 mm, 50-mm diameter) (ASL5040-UV,

Thorlabs, New Jersey, USA). The LED light was irradiated onto a 900 × 30 μm area rectangle,

which is an image of the entrance slit (S30K Thorlabs, New Jersey, USA) via Lens 4 (f = 40 mm, 50

mm diameter) (ASL5040-UV, Thorlabs, New Jersey, USA) and 3. The image captured by the camera

is exhibited in Fig. 6-2(a). The voltage between MCP-In and MCP-Out (MCP voltage) and the

voltage between MCP-Out and the phosphor screen (acceleration voltage) were set to 2,000 and

3,500 V, respectively. The electron images projected onto the phosphor screen were acquired using

the EM-CCD camera. The camera outputs a digital number of 16 bits for each pixel. The size of the

pixels is 16 μm square, which corresponds to 5.3 μm square on the phosphor screen, and the central

256 × 256 pixels were used. A delay pulse generator (DG 645, Stanford Research Systems,

Sunnyvale, USA) controlled the timings of the laser emission, LED emission, and camera exposure.

(a) Laser irradiation
after charge transfer in camera

(b) Laser irradiation
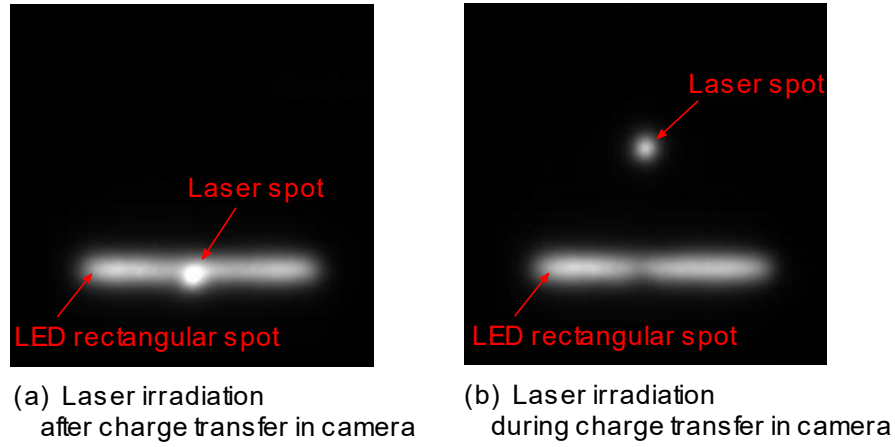during charge transfer in camera

Fig. 6-2. Images acquired by laser irradiation after and during charge transfer in the camera. Both

images were obtained from the co-addition of 1000 replicates of image acquisition. In image (a), the

laser and LED irradiated during the exposure time (i.e. after the vertical charge transfer finished). In

image (b), the laser irradiated 140 µs after the vertical charge transfer finished, and the LED

irradiated during the exposure time. Thereby, the isolation of the laser spot from the LED spot was

achieved, which enabled evaluating the intensity of the LED rectangular spot.
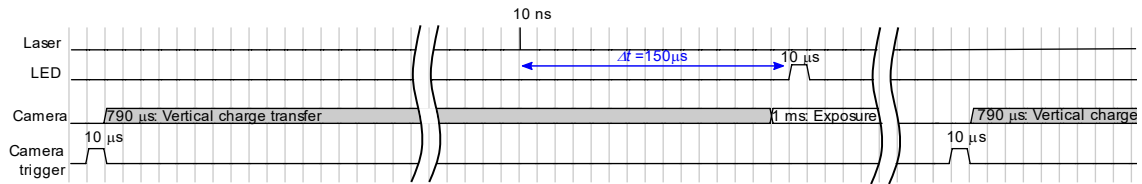
Fig. 6-3. Timing diagram of the laser and LED emissions and camera operation. One horizontal

division indicates 10 µs. The time interval Δt between the laser and the LED emissions was set to

150 µs. When the camera receives the trigger signal, the camera shifts vertically the charges on the

pixels and starts the exposure 790 µs later. The laser emitted 140 µs before the vertical charge

transfer finished, to isolate the laser spot from the rectangular LED spot.

Figure 6-3 shows the timings of light pulses and camera exposure. The repetition rate for the laser pulse was set to 20 Hz to provide sufficient time to fully recover the MCP gain in one period. The electron multiplication process was initiated using a 10 ns laser light pulse. After a delay of 150 μs, the resulting gain drop was observed. Because the gain recovery time was comparable to the *RC* constant (2.7 ms), the gain was expected not to recover at all during the 150 μs. A power amplifier (T-HVA03, Turtle Industry Co., Ltd., Tsuchiura, Japan) was used to operate the LED, and several photoelectrons per pulse were generated. When the EM-CCD camera, which is a frame transfer camera, receives the trigger signal, the charges in the pixels are transferred vertically for 790 μs and reset, and then, the exposure starts. When the laser and LED emitted light during the exposure period, their spots overlapped, as shown in Fig. 6-2(a). As the interval of 150 μs was too short for the frame rate, it was unfeasible to acquire the laser and LED spots separately. To avoid this superimposition and to isolate the two spots, the laser was emitted 140 μs before the exposure started, i.e. during the vertical charge transfer, as shown in Fig. 6-3. Consequently, the laser spot was shifted only in the vertical direction by 98 pixels, corresponding to 520 μm on the phosphor screen, as shown in Fig. 6-2(b). Image analysis and processing were performed using open-source software "ImageJ" <Version number 1.53U> (https://imagej.nih.gov/ij/). The relationship between the spot intensity on the image acquired by the EM-CCD camera and the output charge measured by the oscilloscope was verified, as described in Section 6.5.2 of the Supplemental Information.

6.3 Results and discussions

6.3.1   Evaluation of the spatial extent of gain drop for a single pulse

According to the method indicated in Section 6.2.2, the spatial extent of the gain drop was evaluated. The MCP voltage and the acceleration voltage were set to 2,000 and 3,500 V, respectively. The time

interval between laser and LED emissions Δt was set to 150 μs. The measurement was performed

for 2,850 seconds at a repetition rate of 20 Hz, namely, 57,000 images were acquired. In addition, the

images were acquired with the laser turned off and compared with the images with the laser turned on.

Figure 6-4 shows the output charge distribution for the first laser pulse. The output charge Q_1 for

the first pulse was obtained from the laser spot intensity on the image using the calibration curve

shown in Fig. S6-3. The average output charge was 2.3 pC. Based on the average output charge of

0.31 pC for a single photoelectron, the number of photoelectron occurrences per pulse was estimated

to be approximately seven photoelectrons in the illuminated channels (the single ion response data,

which represent the detector gain, are shown in Fig. S6-1). To verify the number of activated

channels, the location of the center of mass of the laser spot was calculated for each laser pulse

event. Figure 6-5 shows the distribution of the center of mass of the laser spot. The deviations in the

address of the spot center were less than 20 μm in the horizontal and vertical directions. This

characteristic implies that almost all the photoelectrons were generated in a specific channel and its

six neighboring channels. The distance between the center of a channel and the edge of its

neighboring channel is 21 μm, suggesting that photoelectron generation was predominantly

concentrated within this particular set of channels.

Figures 6-6(a) and (b) show 500 integrated images when the laser was on and off, respectively. The

images were classified by the histogram shown in Fig. 6-4. A gain drop was clearly observed in the

channels irradiated by the laser light and the surrounding channels. The output charge Q_1 was

considered to be equal to the amount of the wall charge in the MCP because a Δt of 150 μs was

much shorter than the RC constant and the charges were not replenished at all during the 150 μs. The

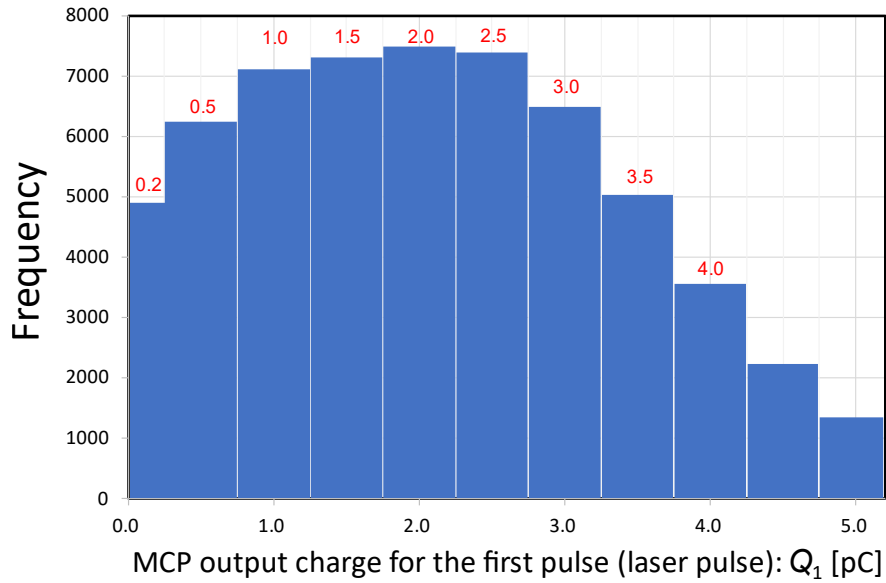dark area representing the gain-drop spatial extent was extended as Q_1 was increased.

Fig. 6-4. MCP output charge distribution for the first pulse (laser pulse). The number of data was 57000, and the average amount of charge was 2.3 pC. The data were classified into 8 classes with a bin width of 0.5 pC bin in the range from 0.25 to 4.25 pC. The first bin (0.2 pC) ranges from 0.15 to 0.25 pC. The frequency in the first bin (0.2 pC) in this figure is plotted five times of raw data to compensate for the difference in the bin width.
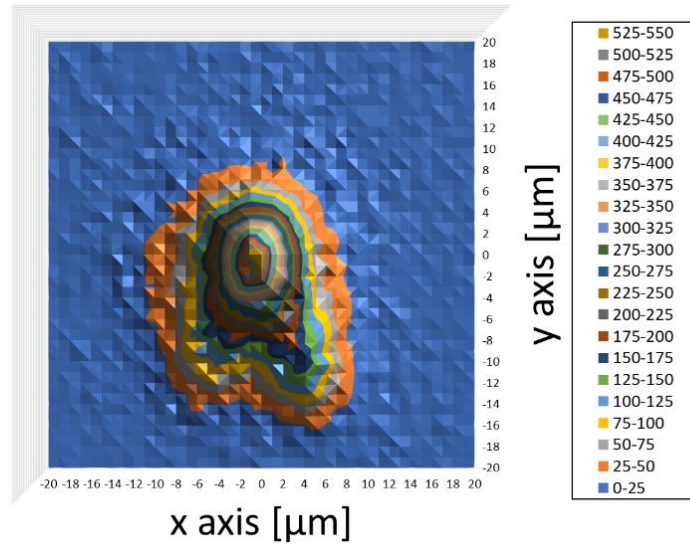

Fig. 6-5. Distribution of the center of the mass of the spot output by the MCP following laser irradiation. The most frequent point was set as the origin of the coordinate system.

(a) Laser on   (b) Laser off   (c) Q_1=0.2 pC   (d) Q_1=0.5 pC

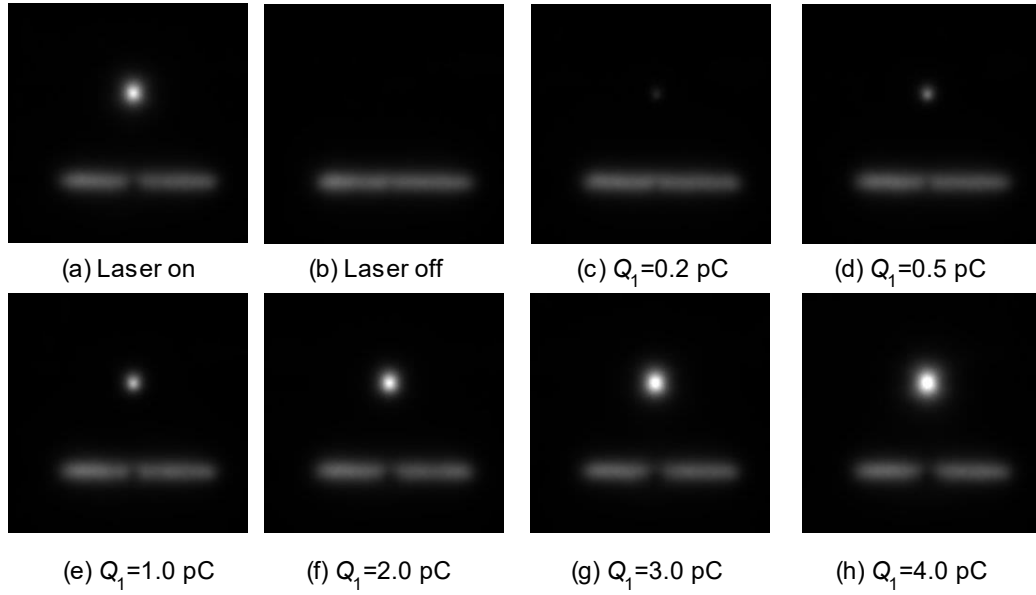(e) Q_1=1.0 pC   (f) Q_1=2.0 pC   (g) Q_1=3.0 pC   (h) Q_1=4.0 pC

Fig. 6-6. Integrated images of 500 images.

To quantitatively evaluate the spatial extent, the spatial distribution of the relative gain in the area irradiated by the LED beam was determined. First, the horizontal LED-beam profile was obtained by averaging the central 5 pixels (27 μm on the screen) in the vertical direction. Subsequently, the LED-beam profile with the first pulse was normalized to that without the laser pulse, resulting in a relative gain distribution $G(x)$ in the horizontal direction (x). The spatial gain distribution is plotted in Fig. 6-7 with Q_1 as a parameter. It appears that the gain hardly decreased at Q_1= 0.2 pC and started to decrease beyond 0.5 pC, and the extent of the gain drop was extended as Q_1 was increased. Both the magnitude of the gain drop and the spatial extent increased as Q_1 increased. The spatial extent W of the gain drop at which the relative gain is 90% is plotted against the output charge Q_1, as shown in Fig. 6-8. W was 260 μm (i.e., 130 μm in radius) at $Q_1 = 4$ pC. The extent of 130 μm in radius indicates that the gain drop was extended to the eighth neighboring channels, where there were approximately 280 channels.
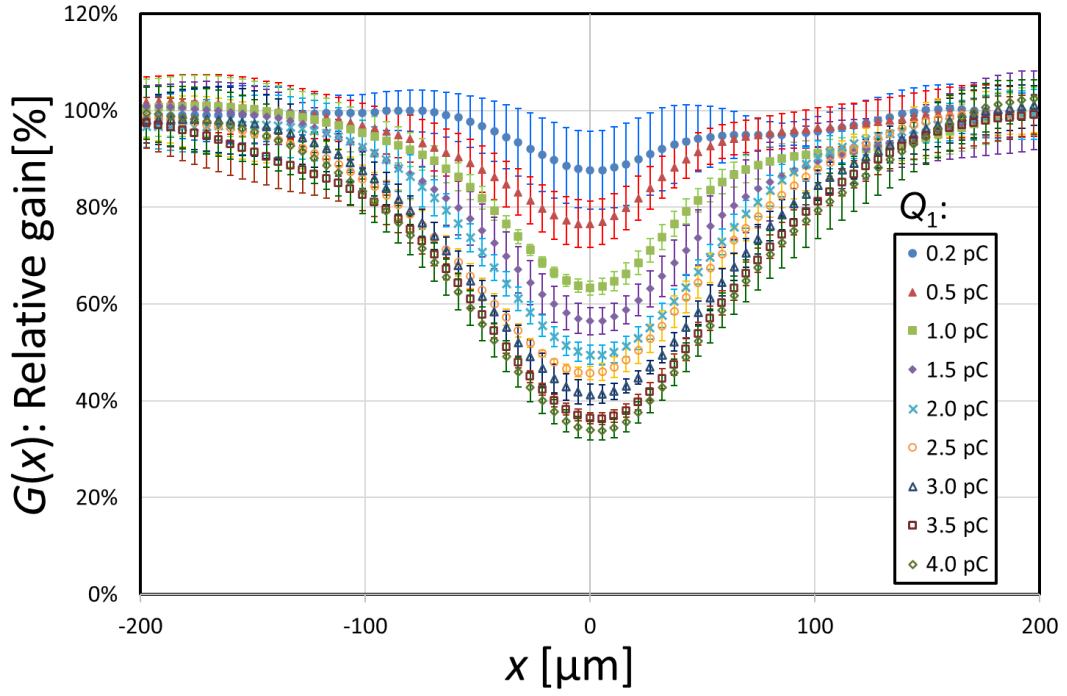
Fig. 6-7. Spatial distribution of the relative gain $G(x)$ in the horizontal direction (x), with the output charge Q_1 as a parameter for the first pulse. The 4 average data were plotted, and the error bars indicate the standard deviations. Only the 0.2 pC data consist of 2 data. The relative gain profiles were shifted such that the point where the relative gain was minimum was $x = 0$.

It was considered that the electric field produced by the wall charges in the activated channels caused the spatial extension of the gain drop. Previously, Anacker et al. calculated the transverse electric field produced by the wall charges and estimated the spatial extent of the gain drop from the electric field, assuming that the total wall charge, which is equal to the output charge Q_1, was a uniform line charge [6-1]. In their model, the spatial extent of the gain drop was extended proportionally to the output charge Q_1. However, in Chapter 5 the wall charges were considered to be increased exponentially along the channel axis toward the exit of the channel. In this model, the spatial extent of the gain drop estimated from the transverse field was proportional to the
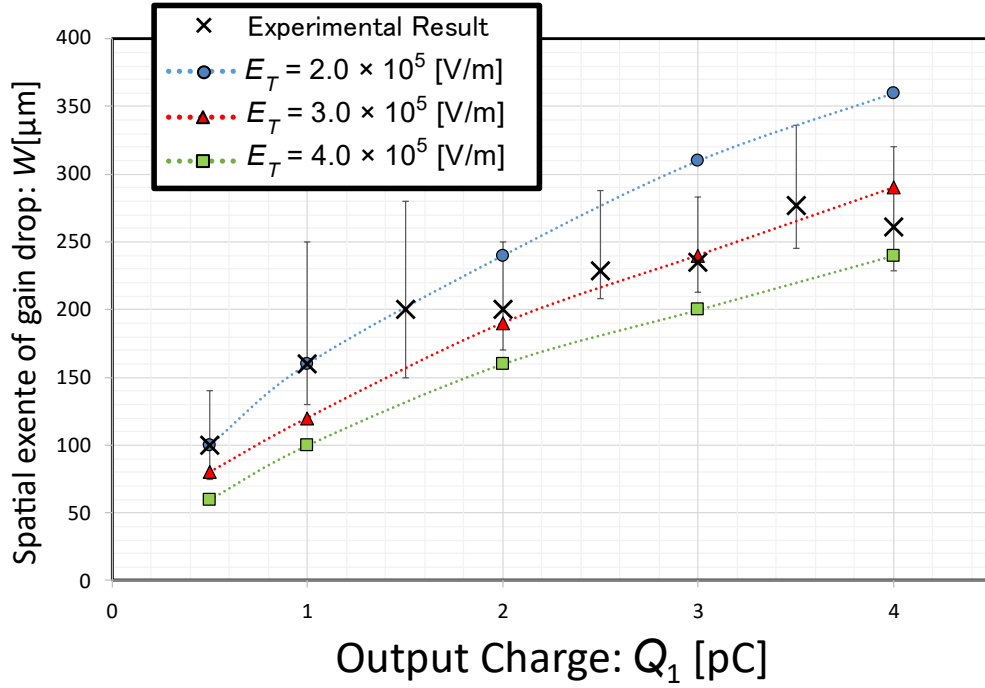
Fig.6-8. Spatial extent W of the gain drop against output charge Q_1 for the first pulse. The black dots show the experimental results. The colored dots with lines show the estimated spatial extents assuming that the gain drop begins when the transverse electric field E_T is 1.0×10^5, 2.0×10^5, or 3.0×10^5 V/m.

square root of the wall charge when the distance from the activated channel exceeded 50 μm. The experimental result agrees well with the estimates, assuming that the gain decrease begins when the transverse electric field E_T reaches 2.0×10^5 or 3.0×10^5 V/m, as shown in Fig. 6-8. This agreement suggests that the transverse electric field produced by the wall charge caused the spatial extension of the gain drop, and that the wall charge was not a uniform line charge.

In Chapter 4, the gain recovery time constant of the chevron MCP was evaluated using the double pulse and continuous irradiation methods. The continuous irradiation method was expected to overestimate the time constant because it does not take into account the spatial extent of the gain

drop. Assuming that the multiplication processes for a single photoelectron decreased the gains of 20 channels to zero ($a = 20$) when the average output charge was 1.1 pC, the time constant obtained by the continuous irradiation method was in good agreement with that obtained by the double pulse method. This implies that 20 channels were dead because of the detection of one photoelectron. On the other hand, the gain-drop spatial extent W was 160 μm at $Q_1 = 1.0$ pC, as shown in Fig. 6-7. The spatial extent corresponds to approximately 110 channels. In order to compare the experimental results with the estimates, the influence of the spatial extension of the gain drop must be investigated by considering the product of the gain and area. In this study, the gain was normalized by the gain when no gain drop occurs, which is defined as the relative gain. Consequently, an evaluation index of "gain volume," which is the product of the relative gain and area, was introduced. First, the gain volume per channel was calculated as follows. The gain volume per 1 mm diameter was $\frac{\pi}{4}$ [mm^2]. Because there are 4,200 channels within 1 mm diameter, the gain volume per channel was calculated as 1.87×10^{-4} [mm^2]. Subsequently, the gain volume reduction due to the gain drop was calculated. The relative spatial gain $G(x)$ was fitted using a Gaussian function as follows:

$$G(x) = 1 - A \cdot \exp\left(-\frac{x^2}{\sigma^2}\right) \qquad (6\text{-}1)$$

where $1 - A$ and σ are the relative gain at $x = 0$ and standard deviation, respectively. The experimental result at $Q_1 = 1.0$ pC can be fitted with Eq. (6-1) at $A = 0.345$ and $\sigma = 66.3$ μm, as shown in Fig. 6-9. Assuming that the relative gain distribution has rotational symmetry, the reduced gain volume can be derived from the following equation:

$$\pi \int_{G=1-A}^{G=1} x^2 \, dG = \pi \int_{G=1-A}^{G=1} \left(-\sigma^2 \ln \frac{1-G}{A}\right) dG = \pi A \sigma^2 \qquad (6\text{-}2)$$

The reduced gain volume was 4.76×10^{-3} [mm^2], corresponding to that the gains of 25 channels decrease to zero ($4.76 \times 10^{-3} / 1.87 \times 10^{-4}$). The influence of the gain-drop spatial extension obtained in this study is in good agreement with that expected in Chapter 4. Similarly, the number of

dead channels a was calculated as 44, 64, and 80 at $Q_1 = 2, 3,$ and 4 pC, respectively. The number a of dead channels was approximately increased proportionally to the output charge Q_1.
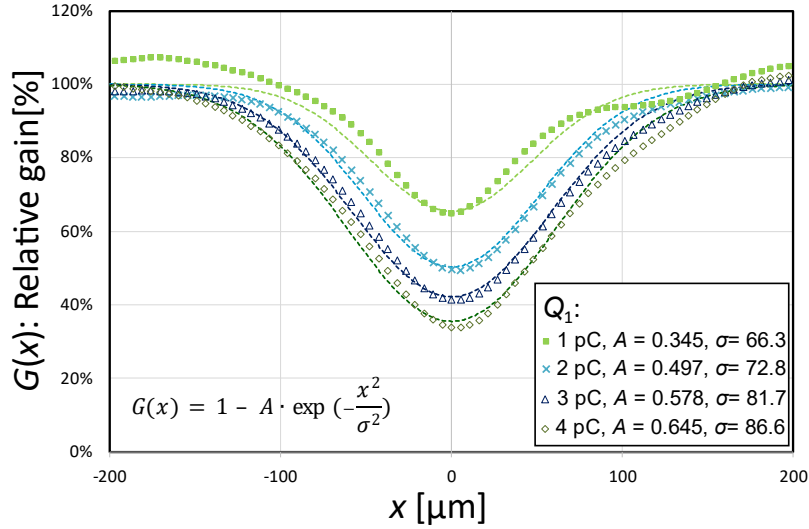

Fig. 6-9 Spatial distribution of the relative gain $G(x)$ fitted by Eq. (6-1)

6.3.2 Evaluation of temporal variation in gain-drop spatial extent

In this subsection, the time course of the spatial gain distribution was evaluated, as the time interval between the laser and LED irradiation Δt was changed from 500 µs to 5 ms by delaying the LED emission timing. Exposure time was changed from 1 to 5 ms to detect delayed LED emission by the camera. The negligible impact of the longer exposure time to dark noise was verified.

Measurement was carried out for 2,850 seconds at a repetition rate of 20 Hz for each Δt, namely 57,000 images were acquired. A total of 57,000 images were classified depending on Q_1. The spatial distribution of the relative gain at $Q_1 = 4.0$ pC is plotted in Fig. 6-10, as a parameter of Δt. As Δt was longer, the relative gain recovered. The gain recovery time was evaluated from the relative gain distribution at $x = 0$, 48 and - 48 µm. The relative gains are plotted as a function of Δt in Fig. 6-11. This relative gain $G(\Delta t)$ was fitted by the following equation.

92

$$G(\Delta t) = 1 - B \exp\left(-\Delta t / kRC\right) \qquad\qquad (6\text{-}3)$$

where $1 - B$ is the relative gain at $\Delta t = 0$. The fitted curves at $x = 0$, 48 and -48 μm were $1 - 0.70 \exp\left(-\dfrac{\Delta t}{0.73RC}\right)$, $1 - 0.50 \exp\left(-\dfrac{\Delta t}{0.47RC}\right)$, and $1 - 0.52 \exp\left(-\dfrac{\Delta t}{0.49RC}\right)$, respectively, where RC was 2.7 ms. The k factors were 0.73 ± 0.2, 0.47 ± 0.08, and 0.49 ± 0.08 at $x = 0$, 48, and -48 μm, respectively, where C is 6.5 ± 0.7 pF. The k factors were consistent with the results ($k = 0.38 \sim 0.68$) by ion and UV light irradiation in Chapters 3 and 4 at an irradiation diameter of 1 to 3 mm, suggesting that the gain recovery time was independent on the irradiation area.

To investigate the spatial extension of the gain drop after 150 μs from the laser irradiation, the relative gain distributions in Fig. 6-10 were compared with those of Fig. 6-7. Figure 6-12 shows an overlay of the relative gain distributions in Figs. 6-7 and 6-10. For example, the relative gain distribution at $\Delta t = 2$ ms and $Q_1 = 4$ pC is approximately the same as the one at $\Delta t = 150$ μs at $Q_1 = 0.5$ pC. The relative gain recovers as if the output charge Q_1 decreases. The results mean that the gain-drop spatial extent did not extend after 150 μs from the laser irradiation. In the past, Anacker et al. calculated the charge transfer time through the lateral capacitances as $\tau \gg RC$ by using the RC circuit model and expected that the charge transfer was not the main mechanism of the spatial extension of the gain drop. Also in this study, the charge transfer affecting the gain-drop spatial extension was not observed. Each channel seems to be electrically isolated from each other.
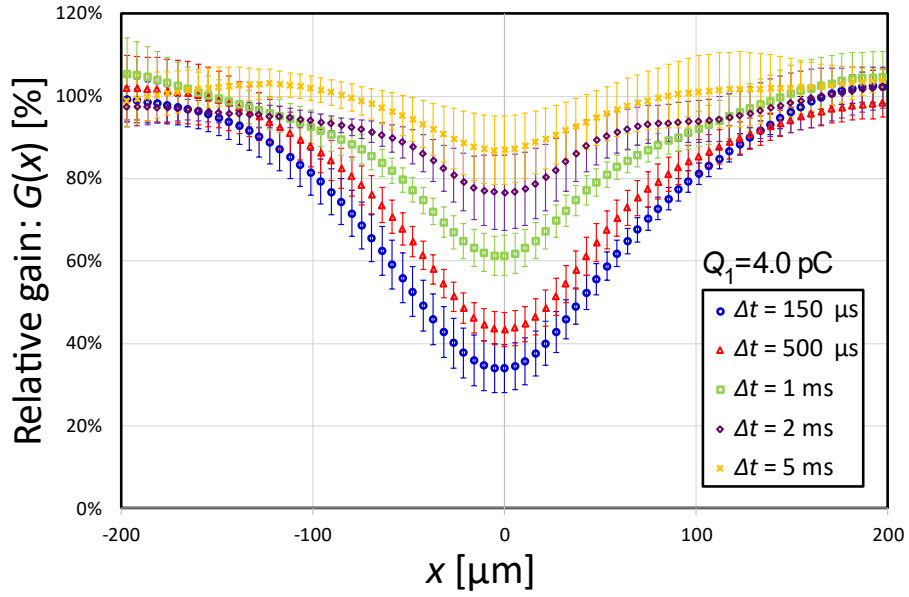
Fig. 6-10. Time course of spatial gain-drop extent at the first pulse charge of 4 pC when Δt was changed to 150 μs, 500 μs, 1 ms, 2 ms, and 5 ms. The 4 average data were plotted, and the error bars indicate the standard deviations. The profile was shifted so that the point where the relative gain was minimum was 0 on the horizontal axis.
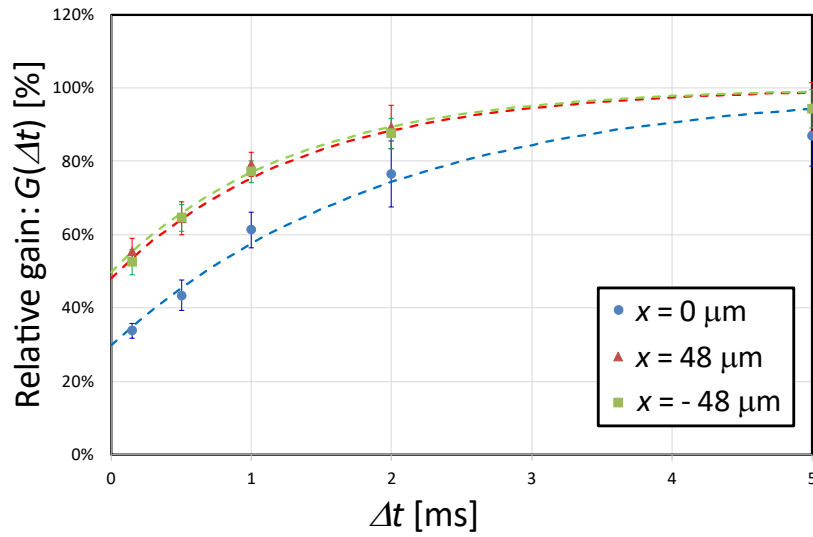

Fig. 6-11. Gain recovery time course at $x = 0$, 48 and - 48 μm. The fitted curves of $x = 0$, 48 -48 μm were $1 - 0.70 \exp\left(-\frac{\Delta t}{0.73RC}\right)$, $1 - 0.50 \exp\left(-\frac{\Delta t}{0.47RC}\right)$, and $1 - 0.52 \exp\left(-\frac{\Delta t}{0.49RC}\right)$, respectively, where RC was 2.7 ms.
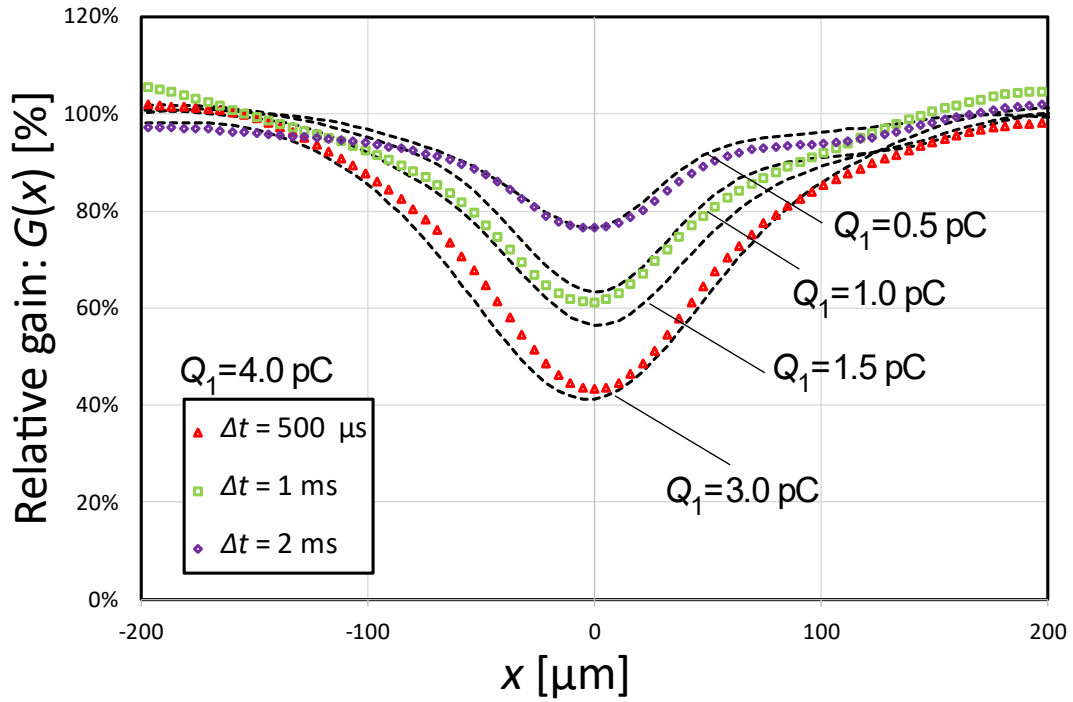
Fig. 6-12. Spatial distribution of relative gain in the horizontal direction. The colored dots indicate the relative gain distribution at $Q_1 = 4$ pC and $\Delta t = 500$ μs, 1 ms, and 2 ms in Fig. 6-10. The black dashed lines indicate the results at $Q_1 = 0.5, 1.0, 2.0,$ and 3.0 pC and $t = 150$ μs in Fig. 6-7. Error bars were removed for more visible.

6.4 Conclusions

The gain-drop spatial extent of a chevron MCP detector was evaluated by first irradiating a pulsed laser light, followed by another light pulse from an LED (exactly 150 μs after the laser pulse). The gain drop was observed not only in the irradiated channels, but also in the surrounding channels. The magnitude and spatial extent of the gain drop strongly depended on the output charge. In Chapter 5, the spatial extent of the gain drop was computationally estimated, assuming that the transverse electric field generated by the wall charges caused the gain drop. The model assumes that the wall charges increase exponentially along the channel axis toward the exit of the channel and that the

extent is proportional to the square root of the wall charge when the distance from the activated

channels exceeds 50 μm. The relationship between the spatial extent and the output charge obtained

in this chapter agrees well with that estimated from the calculated transverse electric field.

Therefore, the electric field produced by the wall charges was concluded to cause the spatial

extension of the gain drop. Furthermore, the influence of the spatial gain-drop extension was

evaluated using the newly introduced evaluation index called "gain volume." The obtained result

corresponded to that the gains of 25 channels decreased to zero when the MCP output was 1.0 pC,

which agrees well with the estimated value (20 channels) in Chapter 4.

6.5 Appendix: Supplemental information

6.5.1 Response of the chevron MCP detector to a single UV photon

  The time response and pulse height distribution (PHD) for a single photoelectron were evaluated by continuous UV light irradiation at less than 0.01 count per second per channel (CPS/ch) to avoid the influence of the MCP gain drop. The MCP and acceleration voltages were set to 2,000 and 500 V, respectively. The electrical signal was acquired by the oscilloscope in self-triggering mode, where the threshold level was 10 mV. Figure S6-1 (a) shows the 1,000 averaged waveform. The pulse height was 18 mV, which corresponds to an output charge of 0.31 pC and gain of 1.9×10^6. Figure S6-1 (b) shows the pulse height distribution for a single photoelectron after 10,000 shots. The average pulse height was 20 mV.

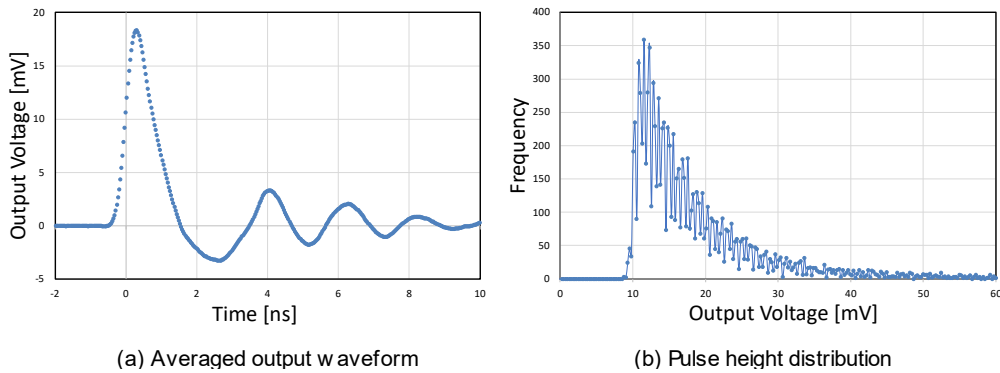(a) Averaged output waveform   (b) Pulse height distribution

Fig. S6-1. Response to a single photoelectron at an MCP voltage of 2,000 V. (a) shows 1,000 averaged output waveform. The pulse height was 19 mV. (b) shows the PHD for 10,000 shots. The average peak height was 20 mV.

6.5.2 Calibration of the EM-CCD camera

The correlation between the spot intensity on the image acquired by the EM-CCD camera and the output charge measured by the oscilloscope was evaluated at MCP and acceleration voltages of 2,000 and 3,500 V, respectively. While a short voltage pulse of 200 ns was applied to the LED to generate a single photon in the pulse, the image and a waveform for the same signal were obtained by the camera and oscilloscope, respectively. The repetition rate and exposure time were set at 20 Hz and 1 ms, respectively. Waveforms with a peaks higher than 8 mV or more were 402 against 21,200 triggers, which means that the photoelectron generation rate per trigger was 1.9%. Data with two peaks or two spots were excluded. Therefore, 390 pairs of waveforms and images were extracted as the effective data. Figure S6-2 shows four representative sets of waveforms and images. The output charge was calculated from the area of a pulse in the waveform, and the spot intensity on an image was calculated by summing the intensities of 101 × 101 pixels against the center of mass of the spot. Figure S6-3 shows the relationship between the output charge and spot intensity for a single photoelectron. The output charge is well correlated with the spot intensity and is expressed as

$$Q = \frac{1}{1.4 \times 10^6} \, I \, [\text{pC}] \qquad\qquad (S6\text{-}1)$$

where Q and I are the output charge [pC] and spot intensity, respectively. Using Eq. (S6-1), the output charge from the detector can be obtained from the image acquired using the EM-CCD camera. In addition, the average spot radius for a single photoelectron at full width at half maximum (FWHM) was evaluated to be 34 μm.
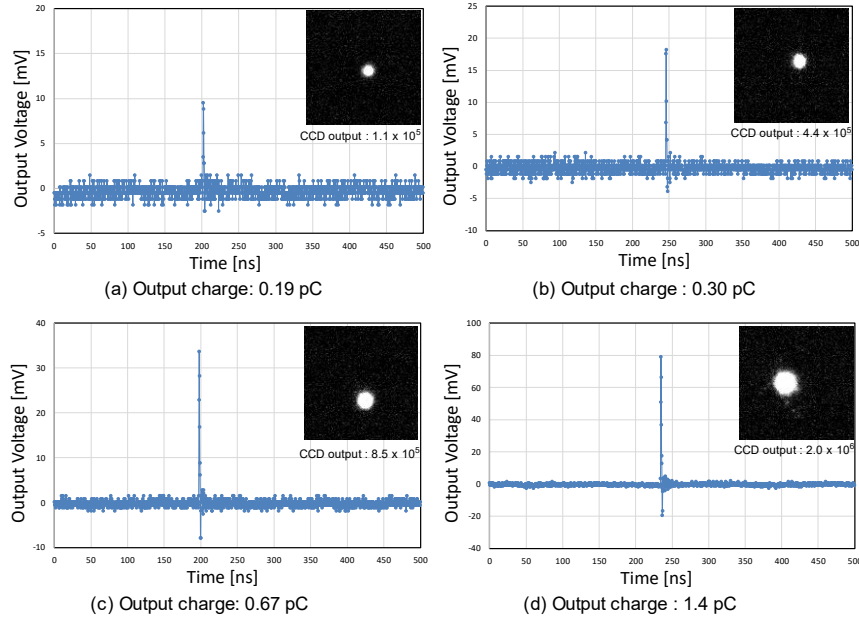
Fig. S6-2. Output waveforms and corresponding images (upper right).

(a) Output waveform and the image at the output charge of 0.19 pC.

(b) Output waveform and the image at the output charge of 0.30 pC.

(c) Output waveform and the image at the output charge of 0.67 pC.

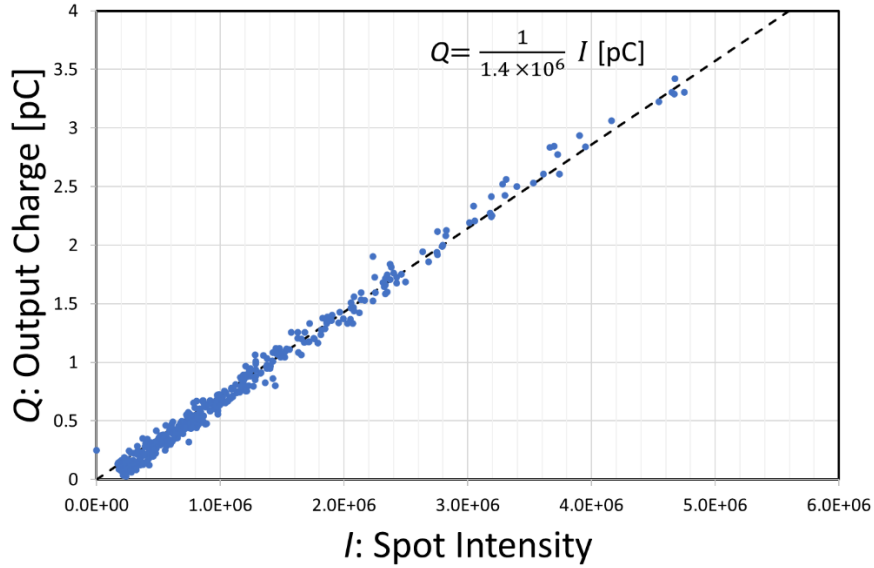(d) Output waveform and the image at the output charge of 1.4 pC.

Fig. S6-3. Relationship between the MCP output charge Q and spot intensity I for a single photoelectron. The output charge Q follows $Q = \frac{1}{1.4 \times 10^6} I$ [pC], where I is the spot intensity calculated from the image acquired by the EM-CCD camera.

References

[6-1]   D.C. Anacker, J.L. Erskine, Review of Scientific Instruments 62 (1991) 1246–1255.

7. Novel ion detector that combines a microchannel plate with an avalanche diode

7.1 Introduction

In the previous chapter, it was concluded that the spatial extension of the gain drop in the microchannel plate (MCP) was caused by the wall charges generated in the activated channels. In chevron MCP, it was expected that the effect of the gain drop is more prominent in the rear plate, because the amount of the wall charge in the rear plate is orders of magnitude higher than that in the front plate. In order to prevent the MCP from the gain drop while keeping sufficient high gain to detect a single particle, it is significant to operate the MCP at the low gain and multiply the electrons by another element which can output a high current. Semiconductor devices are candidates for another electron multiplication element. DeSalvo et al. [7-5] have reported on a photodetector based on a photocathode followed by a planar silicon diode in the bombarding mode, where response was linear up to 10^6 photoelectrons (equivalent to 1 nC of output charge). Alternatively the silicon diode may be replaced by an avalanche diode, which produces additional electron gain by avalanche ionization [7-6], [7-7]. By applying these concepts, the design of the new "MIGHTION" detector alters the rear plate of chevron MCP to be a linear responsive device that minimizes gain drop by combining an MCP with an avalanche diode (Fig. 7-1 (b)).

The gain drops of a conventional chevron MCP and MIGHTION were evaluated by using xenon as a sample for monitoring isotope profile changes on both detectors. Nitrogen with trace-level argon was also studied to validate that MIGHTION does not exhibit gain drop even under intense ion flux conditions.
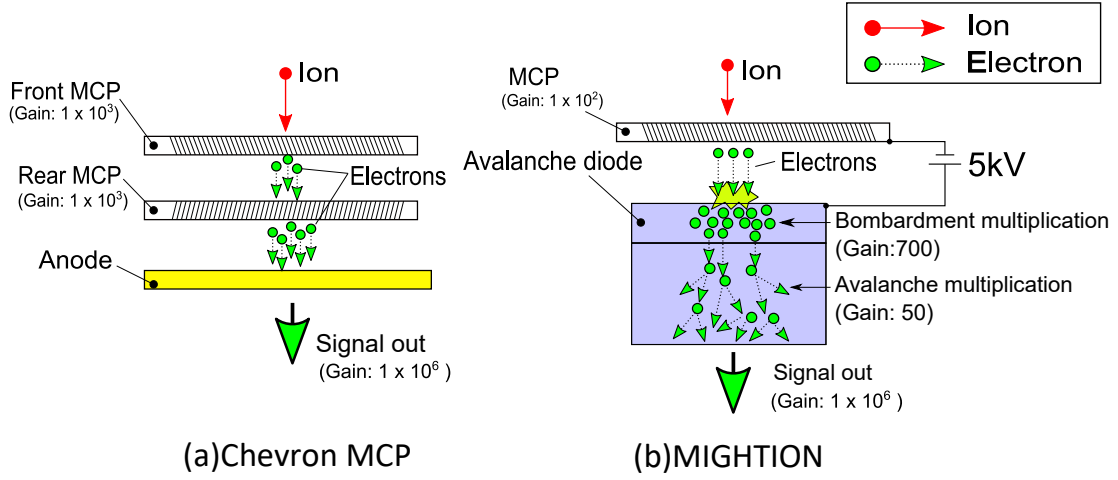
Fig. 7-1. Overview of chevron MCP (a) and MIGHTION (b).

7.2 Design of the detector 'MIGHTION'

The overview of MIGHTION is shown in Fig. 7-1 (b). The MCP converts input ions to electrons with an amplification range of 1 to 10^4 depending on the voltage of MCP-In and MCP-Out (Fig. 7-2). Giudicotti et al. [7-3] introduces the saturation parameter s' for an ion pulse with a duration much shorter than the MCP recharging time as

$$s' = \frac{k \cdot g_0 \cdot N \cdot e}{q_d} \tag{7-1}$$

where k, g_0, N, e, q_d are constant values that describe the shape of the secondary emission function, unsaturated gain, the number of ions or electrons, elementary charge, and charge initially stored in each dynode. In this model, MCP was described as a discreet electron multiplier with a certain number of dynodes. Charge gain g_1 was determined by the following equation:

$$g_1 = g_0 \frac{\ln (1 + s')}{s'} \tag{7-2}$$

The equation shows that g_1 against g_0 reduces to 95%, 69%, and 24% as s' changes to 0.1, 1.0, and 10.

For mass spectrometry, it is important to measure single ions for lower detection limits that require

about 10^6 of gain to the detector. In this detector, a gain of ten thousand, as indicated later, can reduce

the MCP gain to 10^2 while keeping a total gain of 10^6 (Fig. 7-1 (b)). The s' for 10^2 gain on the MCP

was computed as 0.001 for a single-ion input into a microchannel, where $k = 0.5$, $g_0 = 10^2$, $N = 1.0$ and $q_d = 8.1 \times 10^{-15}$. Parameters were estimated such that only 0.049% of the total intensity

are dampened. This combination was predicted to prevent the MCP from having gain attenuation.

As shown in Fig. 7-2 (b), the avalanche diode developed for the hybrid photo detector [7-6,7] is placed

behind the MCP, where the avalanche diode is bonded onto a glass epoxy board. The avalanche diode,

a reverse-type diode for electron detection, was designed so that electrons can be absorbed and

multiplied to a depth of 5 μm from the surface. To accelerate the electrons released from MCP, a

voltage of about 5 kV was applied between the MCP-Out and the AD-p anode, and was connected to

ground through an amplifier. Approximately four hundred volts was delivered to the AD-p anode and

AD-n cathode.

The signal amplification of the avalanche diode is the product of the bombardment gain and the

avalanche gain, with a range of 10^4. The electron bombardment is a process of energy dissipation of a

high energy electron in the silicon crystal. One electron-hole pair is generated by energy dissipation

of 3.6 eV in silicon, so that a gain of 1.4×10^3 should be obtained by applying 5.0 kV. However, the

observed gain was about 700 due to electrons backscattering and energy loss of electrons in the surface

dead layer [7-7,8]. This gain is enough to achieve the target gain of 10^4 by a combination of avalanche

multiplication of a few tens. The electrons generated by electron bombardment drift toward AD-n with

the electric field and reach the avalanche region, where a strong electric field over 2×10^5 V/cm is

applied to further multiply electrons by the avalanche ionization and the gain obtained (avalanche

gain). The avalanche gain is 1 to 300 and can be adjusted by controlling the AD-n potential [7-7].

However, the avalanche diode should be used at the avalanche gain of 50 or less, because the noise

and gain stability for temperature variation worsen with an increase in the avalanche gain. The

amplified signal is available at the SMA connector.
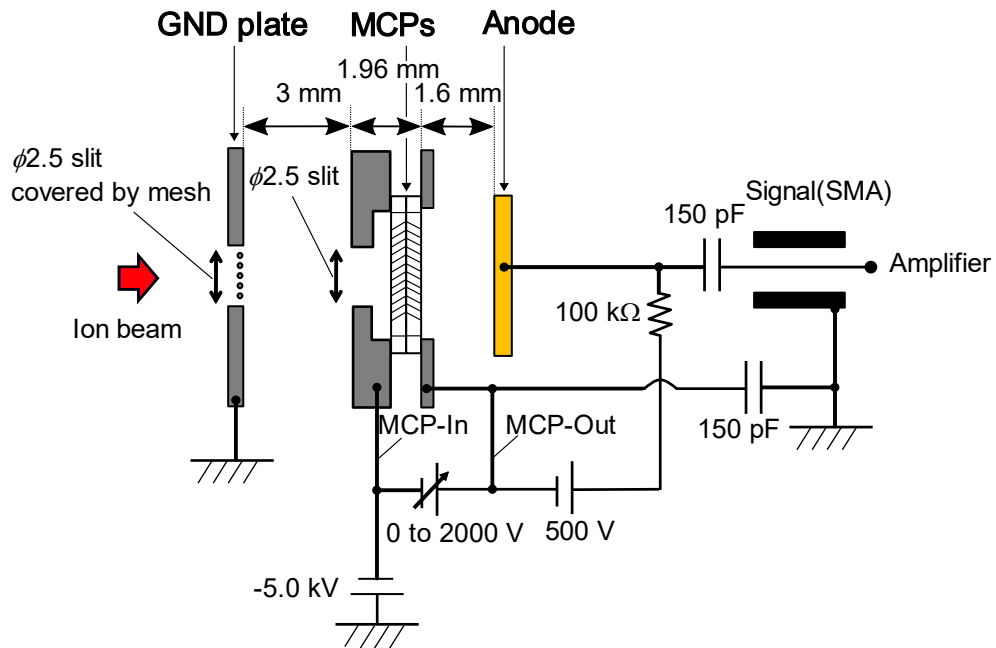
(a) Chevron MCP
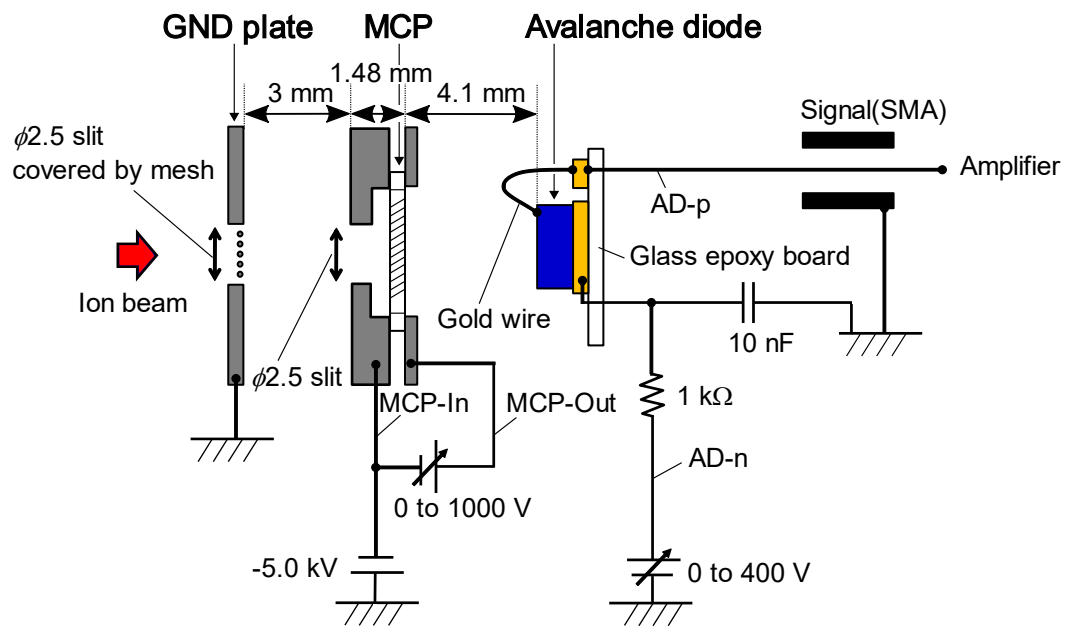
(b) MIGHTION

Fig. 7-2. Configuration of the chevron MCP (a) and MIGHTION (b).

7.3 Experimental

7.3.1 Instrumentation

The infiTOF-UHV (MSI.Tokyo, Inc., Tokyo, Japan) (infiTOF), is a small, portable, TOF mass spectrometer that was derived from the MULTUM-S II multi-turn TOF mass spectrometer. It is capable of high mass resolution and high mass accuracy [7-9,10].   As shown in Fig. 7-3, the infiTOF analyzer has an ion gate capable of excluding unwanted ions.
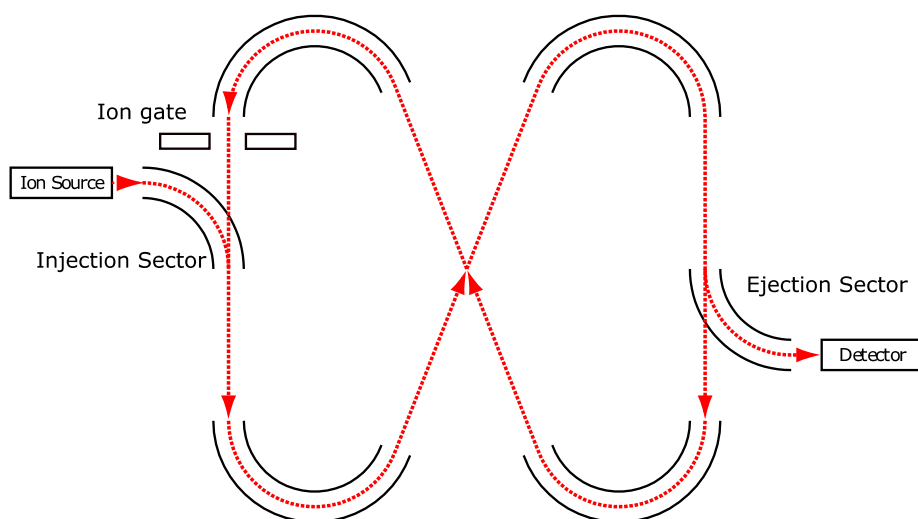

Fig. 7-3 Ion trajectory of infiTOF.

The MCP model F1551-011 (Hamamatsu Photonics K.K., Hamamatsu, Japan) which has 480 μm thickness, 12 μm pore, and approximate 30 MΩ electrical resistance, was used to assemble both the MIGHTION and the chevron MCP. The three-millimeter effective diameter of the electron-sensitive avalanche diode [7-7] was used for the MIGHTION assembly. As shown in Fig.7-2 (a) and 7-2 (b), the MCP-In potential was set to -5 kV and the GND plate with a 2.5 mm diameter slit was placed between the MCP and the analyzer. The slit was covered by a mesh of 40 μm width and 500 μm pitch.

Either the MIGHTION or the chevron MCP was mounted on the back of the infiTOF ejection sector at time of use. Detector gain was verified by the argon ion measurement whenever a detector was mounted onto the analyzer.

The detector signal was passed through a 30 dB attenuator (AT-130V, Hirose Electric Co., LTD., TOKYO, JAPAN) and a C11184 amplifier unit (Hamamatsu Photonics, Hamamatsu Japan), followed by waveform acquisition using an Acqiris U5303A 1GS/s high-speed digitizer (Acqiris, Geneva, Switzerland). The combination of 30 dB attenuator followed by 28 dB preamplifier protected the digitizer from accidents such as detector discharging while keeping the input voltage to the digitizer. Ion counting and waveform averaging coupled with rapid protocol sequence was used [7-11,12]. All data acquisition was performed using open-source software QtPlatz (https://github.com/qtplatz) with its plug-in developed for the infiTOF system. As described in [7-11], the data acquisition system simultaneously generates two series of spectra as a function of elapsed time for every one-second time interval. In essence, this is an averaged (AVG) waveform and ion counting data process.

7.3.2   Sample introduction

A TEDLAR BAG CC-1 (GL Sciences, Tokyo, Japan) was filled with pure argon (Air Liquide Japan) or xenon gas (Takachiho Chemical Industrial Co., Ltd.) and connected through a 10 m length of 0.32 mm inner diameter fused silica capillary. This was followed by a 1.0 m length of 0.1 mm inner diameter PEEK Tubing (Upchurch Scientific, US) used as pressure restrictor. PEEK tubing was then connected to the electron ionization (EI) ion source and used to limit the pressure. Gas flow was controlled by the length of the capillary tubing to maintain the ion source at a pressure range of 7.0×10^{-3} to 5.0×10^{-2} Pa.

The nitrogen gas (Iwatani Corporation) containing the trace-level argon sample was prepared by

adding appropriate amounts of pure argon gas to a TEDLAR BAG that contained pure nitrogen. The

nitrogen/argon mixture sample was introduced while maintaining an ion source pressure of 2.0×10^{-2}

Pa.

7.3.3   Ion counting and detector gain measurement

Detector gain was determined as a function of detector voltage and the obtained argon single-ion

peak height by using the simultaneous ion counting and waveform averaging technique [7-12]. This

technique was used to create a single number that represents the MCP gain at a given MCP voltage

condition. The detector gains were expressed as an average of the single ion peak height at given MCP

conditions, which is calculated from the area-moment of the 50% section of the most frequent ions on

the histogram as follows:

Ions were produced by EI at an ionization voltage of 30 eV and accelerated by 3.8 kV into the mass

analyzer at a repetition rate of 0.1 kHz. The ion count rate was controlled to 30% or less for each TOF

trigger by controlling the emission current of the electron beam. The target ions were selected with the

ion gate and stored in the closed orbit of the mass analyzer. After the 20 laps, the ions were ejected

into the detector through the ejection sector, and each waveform was acquired by the digitizer. The

time-of-flight and peak intensity for each ion of every trigger event were determined using the first

local apex on the waveform following a threshold event (an event where the ion pulse is higher than

10 mV). After a given time interval of 1,000 seconds of argon sample analysis, recorded peak height,

and time-of-flight data were read from the data file and used to build a peak-height frequency

histogram with 5 mV steps. The bell curves were observed, as shown in Fig. 7-4. The detector gains

were expressed as an average of the single ion peak height at given MCP conditions, calculated from

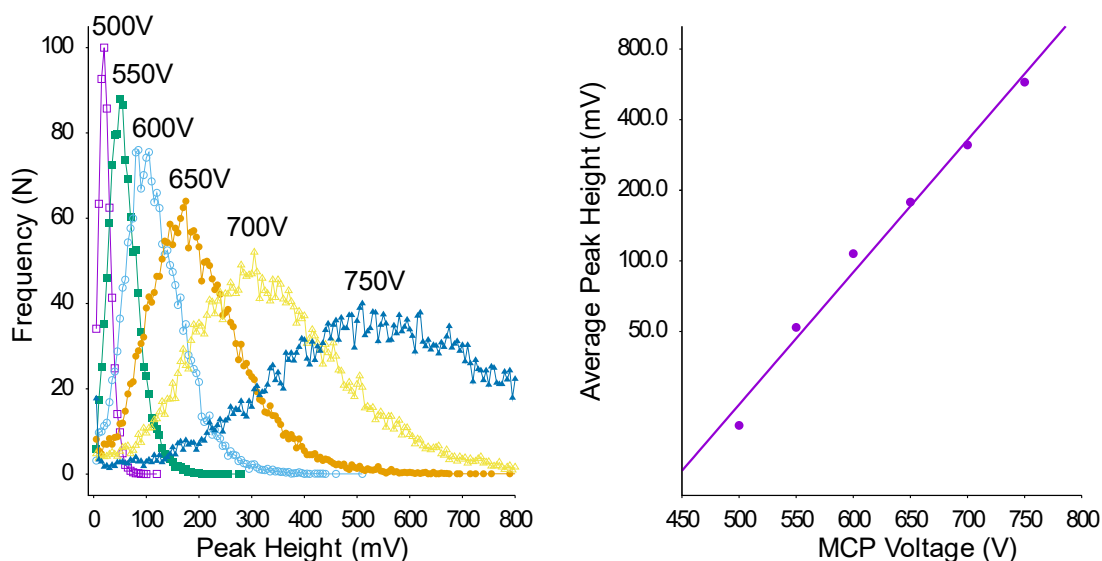the area-moment of the 50% section of the most frequent ions on the histogram.

Fig. 7-4 Relationship between MCP voltage and single argon-ion response histogram on MIGHTION. The peak intensity of the single argon-ion was recorded and represented it as a histogram classified by peak intensity for the step of 5 mV (Left plot). The average peak height (mV) was calculated as the area-moment of a 50% height fraction of the histogram. The logarithm of the average and MCP voltage have a linear relationship (right plot). The average peak heights of the above calculations were 20 mV, 52 mV, 107 mV, 178 mV, 312 mV, and 607 mV. The voltages for MCP-In and MCP-Out were indicated in the figure.

7.4 Results and Discussion

7.4.1   Comparison of xenon isotope ratios

In order to evaluate mass peak suppression for the second and subsequent peaks on a mass spectrum, the xenon isotope ratio was measured at 20 laps by using the ion counting method and the AVG peak area. The ^{128}Xe was excluded by the ion gate to prevent any effect from a minor peak. Peak suppression can be monitored on the AVG spectrum under ion-rich conditions where the count rate of a less abundant isotope, such as ^{130}Xe, was at least 100%.

In contrast, the ion counting result should not be affected by gain drop because the peak detection algorithm for counting is independent of absolute peak intensity. Also, only a few ions per several triggers appeared, in which the suppressor and subsequent ions only occasionally appear on a single trigger waveform. The ion counting results were obtained by accumulating 100,000 trigger events at a repetition rate of 0.1 kHz. The emission current of the electron beam was controlled so that the ion count rate was 30% or less and the ionization voltage was 30 eV.

In both detectors, MCP-in potential was set to -5 kV. MCP voltages for the chevron MCP and MIGHTION were set to 1,550 V and 550 V, respectively, and the avalanche diode voltage for the MIGHTION was set to +350 V. The detector response at the above conditions was verified by single argon ion detection using the method described in section 3.3. The average single argon ion peak was 42 mV·ns and 53 mV·ns for the chevron MCP and MIGHTION, respectively.

Figure 7-5 shows xenon spectra obtained by the chevron MCP and MIGHTION under an ion-rich condition. The acquired peak areas for the chevron MCP and MIGHTION were 1917 mV·ns and 3002 mV·ns, respectively. The ratios of ^{132}Xe/^{129}Xe from AVG waveform peak area to that from ion counting were 31% for chevron MCP and 92% for MIGHTION, as listed in Table 7-1.

Table 7-1. Comparison of xenon isotope ratios from ion counting and AVG peak area.

Recovery was calculated by dividing each ratio from AVG peak area by that from ion counting.
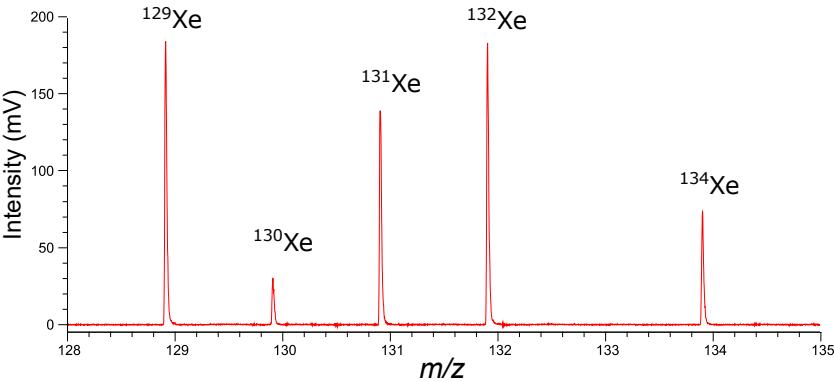
(a) Chevron MCP

	Counts		AVG Peak Area			Recovery
	Counts	Ratio	Peak Area (mV·ns)	CV	Ratio	
^{129}Xe	9433	1.00	1917	0.4%	1.00	100%
^{130}Xe	1498	0.16	184	3.3%	0.10	61%
^{131}Xe	7629	0.81	680	1.0%	0.35	44%
^{132}Xe	9294	0.99	585	4.5%	0.31	31%
^{134}Xe	3791	0.40	203	2.3%	0.11	26%

(b) MIGHTION

	Counts		AVG Peak Area			Recovery
	Counts	Ratio	Peak Area (mV·ns)	CV	Ratio	
^{129}Xe	9133	1.00	3002	1.7%	1.00	100%
^{130}Xe	1365	0.15	457	3.8%	0.15	102%
^{131}Xe	7455	0.82	2332	1.4%	0.78	95%
^{132}Xe	9332	1.02	2834	1.0%	0.94	92%
^{134}Xe	3778	0.41	1140	1.2%	0.38	92%
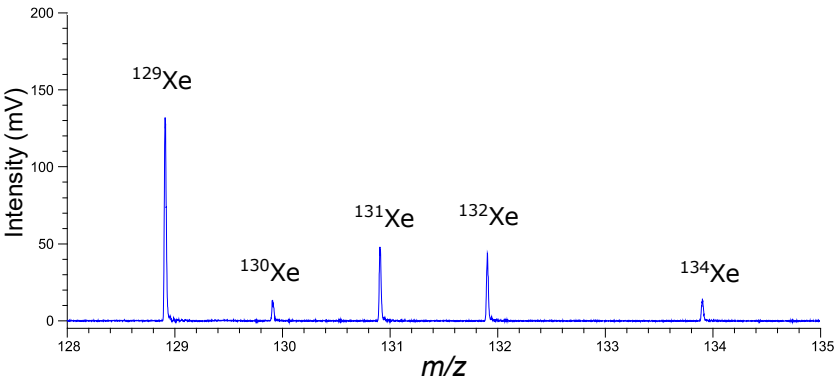
(a) Chevron MCP

(b) MIGHTION

Fig. 7-5. Xenon mass spectra obtained by chevron MCP (a) and MIGHTION (b).

110

7.4.2 The intense ion flux effect

The peak intensities of trace level argon ions with and without the presence of intense nitrogen ion flux were compared. As described in the experimental section, reagent grade argon was spiked into a bag of nitrogen at approximately 5 mL/1,000 mL, and the bag was connected to ion source. Detector output was connected directly to the digitizer input without attenuation or pre-amplification.

The infiTOF analyzer timing was set for 10 laps of N_2 and 9 laps of ^{40}Ar shown as adjacent peaks with 1.17 µs distance in Fig. 7-6. The presence of nitrogen was managed by alternating the ion gate off (Fig. 7-6 top) and on (Fig. 7-6 middle), and the argon ion intensity was monitored in real-time. The emission current of the electron beam was maximized so that the nitrogen ion peak was as intense as possible within the digitizer input limit voltage of 3.6 V, with the repetition rate at 1 kHz.

Setting MCP-In = -1.8 kV, MCP voltage = 800 V, AD-p = +250V, and the ionization voltage = 25 eV, the nitrogen peak voltage was 3.25 V and 22.5 ns at 5% full width, so that the peak area was calculated to be 36.6 V·ns. This corresponds to 0.73 nC of charge. However, no significant change on argon ion peak intensity was observed with or without the presence of high intensity nitrogen as shown in Table 7-2. The nitrogen peak intensity was about 240 times of the argon peak.

The estimated number of nitrogen ions that hit the detector can be calculated by following formula:

$$I = \frac{C}{G \cdot e} \qquad\qquad (7\text{-}3)$$

where I, C, G, and e are the number of input ions, output charge, detector gain, and elementary charge, respectively. About 4,800 nitrogen ions hit the detector per TOF trigger, where it was calculated from the output charge $C = 0.73$ nC, and the MIGHTION gain $G = 9.6 \times 10^5$. The detector gain, G, was determined by the product of avalanche diode gain and MCP gain. The total avalanche diode gain of a product of avalanche gain and electron bombardment gain at AD-p of 250 V and an acceleration voltage of 1.25 kV between MCP-out and AD-p was obtained as 3.0×10^2 from literature [7-7]. MCP gain of at 800 V was obtained from the quality inspection sheet attached to

the MCP. The MCP used for the detector has 4,200 microchannels for a 1 mm diameter that corresponds to instrumental ion beam size. Thus, the average of 1.1 nitrogen ions per trigger, per channel was determined at the extremely intense signal condition, which corresponds to 1.1×10^3 counts s^{-1} channel^{-1}, on average. According to gain model of Giudicotti, gain dampening was only 1.7% from the calculated saturation parameter s' of 0.035 by using $k = 0.5$, $g_0 = 3.2 \times 10^3$, $N = 1.1$, $q_d = 8.1 \times 10^{-15}$. This is sufficiently low to avoid gain drop for 1.1 ions input into the same channel.
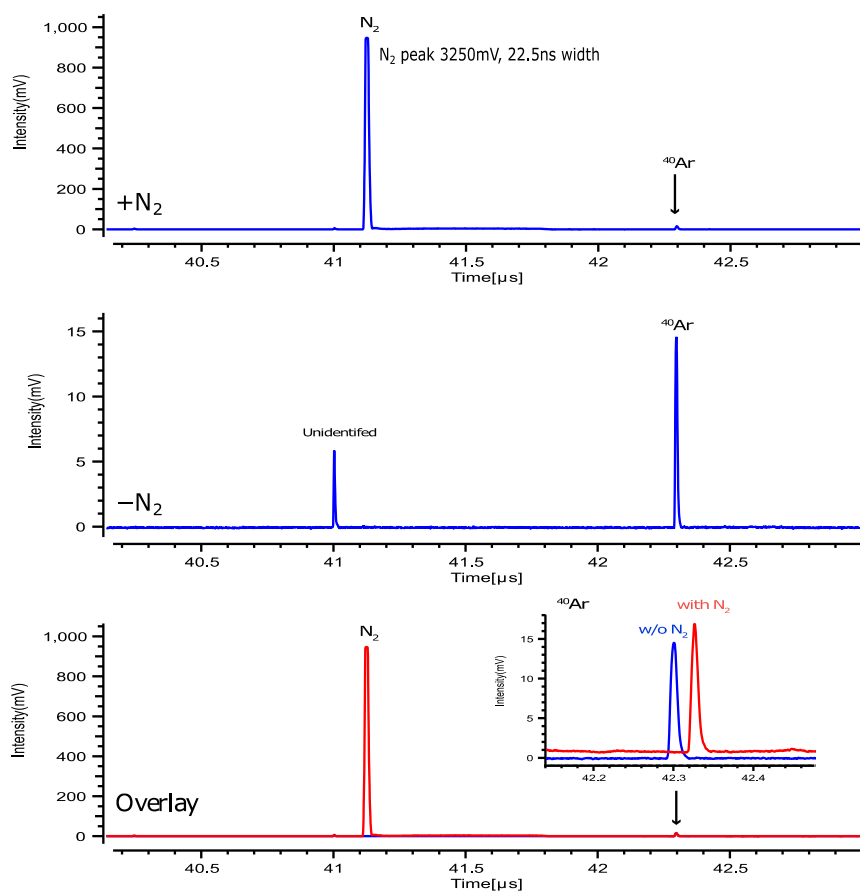
Fig. 7-6. TOF spectra of trace-level argon. Top and middle plots show the spectra with and without nitrogen, respectively. The bottom plot shows the overlaid spectra. In the magnified bottom plot, 0.2 μs and 1 mV are added from the obtained spectra with nitrogen to make them more visible.

Table 7-2. Effect of nitrogen ion presence to argon ion peak intensity on MIGHTION.

	Peak Hight(mV)	PeakArea (mV·ns)
with nitrogen	16.5	151
without nitrogen	15.7	141

7.5 Conclusions

No gain drop in MIGHTION was observed even after the measurement of an intense signal. In contrast, the gain drop was observed in the chevron MCP, and $^{132}Xe/^{129}Xe$ obtained from AVG waveform peak area was dampened to 31% compared to that from ion counting. In the escalated condition, a nitrogen ion signal was prepared to be as intense as possible and increased the nitrogen peak height to 3.25 V, which was almost at the digitizer input limit. The estimated number of nitrogen ions at this condition was about 1.1 per channel, which was not enough to cause the gain drop based on the gain model of Giudicotti. By combining MCP and the avalanche diode, a new detector was developed that resolves the gain drop problem inherent in MCP detectors.

References

[7-1]   A. Westman, G. Brinkmalm, D.F. Barofsky, International Journal of Mass Spectrometry and Ion Processes 169–170 (1997) 79–87.

[7-2]   G.W. Fraser, J.F. Pearson, G.C. Smith, M. Lewis, M.A. Barstow, IEEE Transactions on Nuclear Science NS-30 (1983) 455–460.

[7-3]   L. Giudicotti, M. Bassan, R. Pasqualotto, A. Sardella, Review of Scientific Instruments 65 (1994) 247–258.

[7-4]   C.A. Kruschwitz, M. Wu, K. Moy, G. Rochau, Review of Scientific Instruments 79 (2008) 10E911.

[7-5]   R. DeSalvo, W. Hao, Y. You, Y. Wang, C. Xu, Nuclear Instruments and Methods in Physics Research Section A: Accelerators, Spectrometers, Detectors and Associated Equipment 315 (1992) 375–384.

[7-6]   M. Suyama, Y. Kawai, S. Kimura, N. Asakura, K. Hirano, Y. Hasegawa, T. Saito, T. Morita, M. Muramatsu, K. Yamamoto, IEEE Transactions on Nuclear Science 44 (1997) 985–989.

[7-7]   A. Fukasawa, J. Haba, A. Kageyama, H. Nakazawa, M. Suyama, IEEE Transactions on Nuclear Science 55 (2008) 758–762.

[7-8]   M. Suyama, Development of Multi-Pixel Photon Sensor with Single-Photon Sensitivity, The

Graduate University for Advanced Studies, 2002.

[7-9]   S. Shimma, H. Nagao, J. Aoki, K. Takahashi, S. Miki, M. Toyoda, Anal. Chem. 82 (2010) 8456–8463.

[7-10]   T. Hondo, K.R. Jensen, J. Aoki, M. Toyoda, Eur J Mass Spectrom (Chichester) 23 (2017) 385–392.

[7-11]   K.R. Jensen, T. Hondo, H. Sumino, M. Toyoda, Anal. Chem. 89 (2017) 7535–7540.

[7-12]   Y. Kawai, T. Hondo, K.R. Jensen, M. Toyoda, K. Terada, J. Am. Soc. Mass Spectrom. 29 (2018) 1403–1407.

8. Conclusions

The gain-drop phenomenon on a microchannel plate (MCP), particularly the gain recovery time and spatial extension of the gain drop, was investigated, and a new ion detector, 'MIGHTION,' was developed based on the findings of this study.

8.1 Gain recovery time constant

First, the gain recovery time of the chevron MCP detector was evaluated by ion irradiation and ultraviolet (UV) light irradiation. In the past, Fraser et al. evaluated the gain recovery time constants and compared them with the RC constant, which is a product of the resistance R and capacitance C of the channel plate [8-1,2]. Because the time constants did not correspond well with the RC constant, the time constant τ was expressed using R and C.

$$\tau = kRC \qquad\qquad (8\text{-}1)$$

Moreover, in this study, the gain recovery time constants were compared with the RC constant, as well as the results of the work of Fraser et al. As described in Chapters 3 and 4, the following are the findings of this study.

(1) The gain recovery time does not depend on the type of incident particles (ions or photons). The k factors obtained by the double-pulse method were $k = 0.38\pm0.1$ and 0.48 ± 0.07 for ion irradiation and $k = 0.62\pm0.2$ to 0.68 ± 0.1 for UV light irradiation.

(2) The gain drop was caused by the input of a significantly smaller number of particles (photoelectrons or ions) than the number of channels irradiated. Under UV light irradiation, the MCP gain was decreased to 47% when ~270 photoelectrons were generated in a diameter of 3 mm corresponding to 38,000 channels. This suggests that the gain drop occurred not only in the activated channels but also in the surrounding channels of them.

(3) The k factors obtained by the continuous irradiation method were 6.6–17 and significantly different from those obtained by the double-pulse method (0.38–0.68). This overestimation is attributed to the fact that the model formula used in the continuous irradiation method did not consider the spatial extension of the gain drop described above (in point no. (2)). Assuming that electron multiplication for one photoelectron decreases the gains of 20 channels to zero (where the 1.1 pC output from the MCP for a single photoelectron), the k factors obtained by the continuous irradiation method closely match those obtained by the double-pulse method.

(4) The gain recovery time constant is comparable to the RC constant. Fig. 8-1 shows the relationships between the k factors and illumination areas obtained in previous studies and in this study.
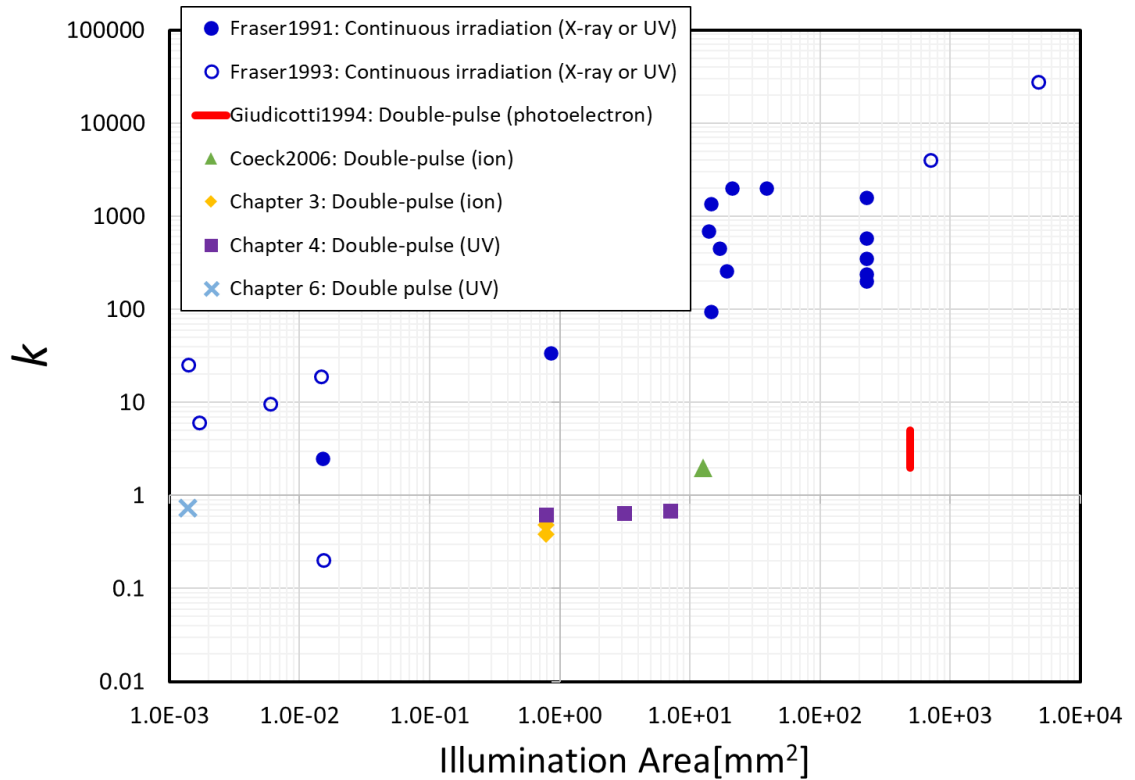
Fig. 8-1. Relationships between the k factors and illumination areas obtained from this study as well as previous studies [8-1], [8-2], [8-3], [8-4].

117

8.2 Estimating the spatial extent of the gain drop

One of the possible mechanisms of the spatial extension of the gain drop observed in result (2) in Section 8.1 was that the electric field produced by the wall charges in the activated channels leaks to the surrounding channels, thereby affecting the gains of the surrounding channels. In Chapter 5, the electric field produced by the wall charges is calculated, and the spatial extent of the gain drop is estimated, assuming that the wall charges increase exponentially along the channel axis toward the channel exit.

(1) The electron trajectory in the MCP was disturbed when the transverse electric field generated by the wall charges increased to approximately 2.0×10^5 V/m, suggesting the gain drop initiates.

(2) The spatial extent was expected to be proportional to the square root of the number of wall charges in the region where the distance from the activated channels exceeded 50 μm, corresponding to the third neighboring channel. The wall charges behaved as point charges when their distance from the activated channel was sufficiently long. However, the spatial extent of the gain drop was proportional to the wall charges when the distance was not large because the wall charges acted as a line charge.

8.3 Evaluation of the spatial extent of the gain drop

In Chapter6, the spatial extent of a single pulse was experimentally evaluated and compared with the estimates in Chapter 5. The first pulse from the UV laser was irradiated onto one channel and the first neighboring channels to cause a spatial extension of the gain drop. To observe the spatial extent of the gain drop, a second pulse from the UV LED was irradiated over an area of 900×30 μm around the activated channels. The spatial distribution of the MCP output was projected onto a phosphor screen behind the MCP and acquired using an EM-CCD camera. The results are as follows:

(1) The magnitude and spatial extent of the gain drop depended on the amount of the output charge per pulse. When the output charge exceeded 0.5 pC from the MCP, the gain drop was initiated. The relationship between the spatial extent and output charge corresponds well with our estimates in Section 8.2, suggesting that the transverse electric field produced by the wall charges causes the spatial extension of the gain drop.

(2) When the output charge was 1.0 pC, the spatial extent of the gain drop was 160 μm in diameter, and the gains of approximately 110 channels decreased by 10% or more. This effect corresponds to the fact that the gains of the 25 channels decrease to zero, which is comparable to the assumption in result (3) in Section 8.1.

(3) The spatial extension of the gain drop occurred within 150 μs, which is one order of magnitude shorter than the RC constant, after the laser irradiation and did not extend further. This result suggests that charge transfer did not affect the spatial extension of the gain drop.

8.4 Development of a novel ion detector combining an MCP with an avalanche diode

This study concludes that the spatial extension of the gain drop was caused by the electric field produced by the wall charges, which was comparable to the output charge. Thus, one of the most effective approaches is to keep the MCP gain low and multiply the electrons further using another element that has a high saturation current. Therefore, a new ion detector, 'MIGHTION,' was developed and evaluated using the time-of-flight (TOF) mass spectrometer, as described in Chapter 7. In MIGHTION, an avalanche diode was used instead of the rear MCP of the chevron MCP detector. No gain drop in MIGHTION was verified after a large signal comparable to the digitizer input limit, which was 3.25 V at 50 Ω termination, corresponding to 0.73 nC. Using MIGHTION can be beneficial in improving the quantitative performance of TOF mass spectrometers.

References

[8-1] G.W. Fraser, M.T. Pain, J.E. Lees, J.F. Pearson, Nuclear Instruments and Methods in Physics Research Section A: Accelerators, Spectrometers, Detectors and Associated Equipment 306 (1991) 247–260.

[8-2] G.W. Fraser, M.T. Pain, J.E. Lees, Nuclear Instruments and Methods in Physics Research Section A: Accelerators, Spectrometers, Detectors and Associated Equipment 327 (1993) 328–336.

[8-3] L. Giudicotti, M. Bassan, R. Pasqualotto, A. Sardella, Review of Scientific Instruments 65 (1994) 247–258.

[8-4] S. Coeck, M. Beck, B. Delauré, V.V. Golovko, M. Herbane, A. Lindroth, S. Kopecky, V.Yu. Kozlov, I.S. Kraev, T. Phalet, N. Severijns, Nuclear Instruments and Methods in Physics Research Section A: Accelerators, Spectrometers, Detectors and Associated Equipment 557 (2006) 516–522.

Acknowledgments